

Abstract

Measurement of (π^- -Ar) and (K^+ -Ar) total hadronic cross sections in the LArIAT experiment

Elena Gramellini

2018

6 Abstract goes here. Limit 750 words.

7 **Measurement of (π^- -Ar) and (K^+ -Ar)**

8 **total hadronic cross sections in the**

9 **LArIAT experiment**

10 A Dissertation
11 Presented to the Faculty of the Graduate School
12 of
13 Yale University
14 in Candidacy for the Degree of
15 Doctor of Philosophy

16 by
17 Elena Gramellini

18 Dissertation Director: Bonnie T. Fleming

19 Date you'll receive your degree

²⁰

Copyright © 2018 by Elena Gramellini

²¹

All rights reserved.

22

A mia mamma e mio babbo,

23

grazie per le radici e grazie per le ali.

24

To my mom and dad,

25

thank you for the roots and thank you for the wings.

²⁶ Contents

²⁷	Acknowledgements	viii
²⁸	0 Introduction	1
²⁹	1 The theoretical framework	2
³⁰	1.1 The Standard Model	2
³¹	1.2 Neutrinos: tiny cracks in the Standard Model	5
³²	1.2.1 Neutrinos in the Standard Model	5
³³	1.2.2 Neutrino Oscillations	7
³⁴	1.2.3 Make up of Neutrino Interactions	8
³⁵	1.3 Beyond the Standard Model	10
³⁶	1.3.1 Open Questions in Neutrino Physics	12
³⁷	1.3.2 Towards a more fundamental theory: GUTs	16
³⁸	1.4 Motivations for Hadronic Cross Sections in Argon	19
³⁹	1.4.1 Pion-Argon Total Hadronic Cross Section	19
⁴⁰	1.4.2 Kaon-Argon Total Hadronic Cross Section	30
⁴¹	2 Liquid Argon Detectors at the Intensity Frontier	35
⁴²	2.1 The Liquid Argon Time Projection Chamber Technology	35
⁴³	2.1.1 TPCs, Neutrinos & Argon	36
⁴⁴	2.1.2 LArTPC: Principles of Operation	38

45	2.1.3	Liquid Argon: Ionization Charge	41
46	2.1.4	Liquid Argon: Scintillation Light	46
47	2.1.5	Signal Processing and Event Reconstruction	50
48	2.2	The Intensity Frontier Program	54
49	2.2.1	Prospects for LArTPCs in Neutrino Physics: SBN and DUNE	55
50	2.2.2	Prospects for LArTPCs in GUT Physics: DUNE	56
51	2.2.3	Enabling the next generation of discoveries: LArIAT	58
52	3	LArIAT: Liquid Argon In A Testbeam	61
53	3.1	The Particles' Path to LArIAT	61
54	3.2	LArIAT Tertiary Beam Instrumentation	63
55	3.2.1	Bending Magnets	64
56	3.2.2	Multi-Wire Proportional Chambers	66
57	3.2.3	Time-of-Flight System	68
58	3.2.4	Punch-Through and Muon Range Stack Instruments	69
59	3.2.5	LArIAT Cosmic Ray Paddle Detectors	71
60	3.3	In the Cryostat	72
61	3.3.1	Cryogenics and Argon Purity	72
62	3.3.2	LArTPC: Charge Collection	75
63	3.3.3	LArTPC: Light Collection System	78
64	3.4	Trigger and DAQ	80
65	3.5	Control Systems	82
66	4	Total Hadronic Cross Section Measurement Methodology	88
67	4.1	Event Selection	89
68	4.1.1	Selection of Beamline Events	89
69	4.1.2	Particle Identification in the Beamline	90
70	4.1.3	TPC Selection: Halo Mitigation	90

71	4.1.4	TPC Selection: Shower Removal	91
72	4.2	Beamline and TPC Handshake: the Wire Chamber to TPC Match . .	92
73	4.3	The Thin Slice Method	94
74	4.3.1	Cross Sections on Thin Target	94
75	4.3.2	Not-so-Thin Target: Slicing the Argon	95
76	4.3.3	Corrections to the Raw Cross Section	97
77	4.4	Procedure testing with truth quantities	98
78	5	Data and MC preparation for the Cross Section Measurements	101
79	5.1	Cross Section Analyses Data Sets	101
80	5.2	Construction of a Monte Carlo Simulation for LArIAT	103
81	5.2.1	G4Beamline	103
82	5.2.2	Data Driven MC	108
83	5.3	Estimate of Backgrounds in the Pion Cross Section	111
84	5.3.1	Background from Pion Capture and Decay	111
85	5.3.2	Contributions from the Beamline Background	114
86	5.4	Estimate of Energy Loss before the TPC	117
87	5.5	Tracking Studies	121
88	5.5.1	Angular Resolution	121
89	5.6	Calorimetry Studies	127
90	5.6.1	Kinetic Energy Measurement	127
91	6	Negative Pion Cross Section Measurement	130
92	6.1	Raw Cross Section	130
93	6.1.1	Statistical Uncertainty	132
94	6.1.2	Treatment of Systematics	134
95	6.2	Corrections to the Raw Cross Section	135
96	6.2.1	Background subtraction	135

97	6.2.2 Efficiency Correction	138
98	6.3 Results	142
99	7 Positive Kaon Cross Section Measurement	144
100	7.1 Raw Cross Section	144
101	7.2 Corrections to the Raw Cross Section	146
102	7.3 Results	148
103	A Additional Tracking Studies for LArIAT Cross Section Analyses	151
104	A.0.1 Study of WC to TPC Match	152
105	A.0.2 Tracking Optimization	154
106	B Energy Calibration	155

¹⁰⁷ Acknowledgements

¹⁰⁸ “*Dunque io ringrazio tutti quanti.*

¹⁰⁹ *Specie la mia mamma che mi ha fatto così funky.”*

¹¹⁰ – Articolo 31, Tanqi Funky, 1996 –

¹¹¹ “*At last, I thank everyone.*

¹¹² *Especiallly my mom who made me so funky.”*

¹¹³ – Articolo 31, Tanqi Funky, 1996 –

¹¹⁴ A lot of people are awesome, especially you, since you probably agreed to read

¹¹⁵ this when it was a draft.

¹¹⁶ Chapter 0

¹¹⁷ Introduction

¹¹⁸ **Chapter 1**

¹¹⁹ **The theoretical framework**



¹²⁰ – J. S. Bach, Suite No. 1 in G major, BWV 1007, 1720 ca. –

¹²¹ In this chapter, we set the (π^- - Ar) and (K^+ - Ar) total hadronic cross section
¹²² measurements into the greater theoretical and phenomenological framework. We start
¹²³ by briefly describing the Standard Model (Section 1.1), with particular attention to
¹²⁴ neutrinos and neutrino interactions (Section 1.2). We then describe some of the
¹²⁵ open questions in neutrino physics today and Beyond Standard Model theories (1.3)
¹²⁶ setting the stage for the measurements reported in this work (Section 1.4).

¹²⁷ **1.1 The Standard Model**

¹²⁸ The Standard Model (SM) of particle physics is the most accurate theoretical descrip-
¹²⁹ tion of the subatomic world and, in general, one of the most precisely tested theories
¹³⁰ in the history of physics. The SM describes the strong, electromagnetic and weak
¹³¹ interactions among elementary particles in the framework of quantum field theory,

132 accounting for the unification of electromagnetic and weak interactions for energies
133 above the vacuum expectation value (VEV) of the Higgs field. The SM does not
134 describe gravity or general relativity.

135 The Standard Model is a gauge theory based on the local symmetry group

$$G_{SM} = SU(3)_C \otimes SU(2)_L \otimes U(1)_Y \quad (1.1)$$

136 where the subscripts C indicates the conserved strong charge (color), and the
137 subscripts Y indicates the conserved hypercharge. If we indicated with T the weak
138 isospin T and with T3 its third component, hypercharge can be related to the electric
139 charge Q through the Gell-Mann-Nishijima relation:

$$Q = \frac{Y}{2} + T_3. \quad (1.2)$$

140 In the quantum field framework, the SM fields correspond to the irreducible rep-
141 resentations of the G_{SM} symmetry group. In particular, the particles are divided in
142 two categories, fermions and bosons, according to their spin-statistics. Described by
143 the Fermi-Dirac statistics, fermions have half-integer spin and are sometimes called
144 “matter-particles”. Bosons or “force carriers” have integer spin, follow the Bose-
145 Einstein statistics and mediate the interaction between fermions. The fundamental
146 fermions and their quantum numbers are listed in Tab 1.1.

147 Quarks can interact via all three the fundamental forces; they are triplets of
148 $SU(3)_C$, that is they can exist in three different colors. If one chooses a base where
149 u , c and t quarks are simultaneously eigenstates of both the strong and the weak
150 interactions, the remaining eigenstates are usually written as d , s and b for the strong
151 interaction and d' , s' and b' for the weak interaction, because the latter ones are
152 the result of a CKM rotation on the first ones. Charged leptons interact via the
153 weak and the electromagnetic forces, while neutrinos only interact via the weak force.

Generation	I	II	III	T	Y	Q
Leptons	$\begin{pmatrix} \nu_e \\ e \end{pmatrix}_L$	$\begin{pmatrix} \nu_\mu \\ \mu \end{pmatrix}_L$	$\begin{pmatrix} \nu_\tau \\ \tau \end{pmatrix}_L$	$1/2$	-1	0
	e_R	μ_R	τ_R	0	-2	-1
Quarks	$\begin{pmatrix} u \\ d' \end{pmatrix}_L$	$\begin{pmatrix} c \\ s' \end{pmatrix}_L$	$\begin{pmatrix} t \\ b' \end{pmatrix}_L$	$1/2$	$1/3$	$2/3$
	u_R	c_R	t_R	0	$4/3$	$2/3$
	d'_R	s'_R	b'_R	0	$-2/3$	$-1/3$

Table 1.1: SM elementary fermionic fields. The subscripts L and R indicate respectively the negative chirality (left-handed) and the positive chirality (right-handed).

- 154 The gauge group univocally determines the number of gauge bosons that carry the
 155 interaction; the gauge bosons correspond to the generators of the group: eight gluons
 156 (g) for the strong interaction, one photon (γ) and three bosons (W^\pm , Z^0) for the
 157 electroweak interaction. A gauge theory by itself cannot provide a description of
 158 massive particles, but it is experimentally well known that most of the elementary
 159 particles have non-zero masses. The introduction of massive fields in the Standard
 160 Model lagrangian would make the theory not gauge invariant, resulting ill-defined.
 161 This problem is solved in the SM by the introduction of a scalar iso-doublet $\Phi(x)$, the
 162 Higgs field, which gives mass to W^\pm and Z^0 gauge bosons through the electroweak
 163 symmetry breaking mechanism and to the fermions through Yukawa coupling [74, 75].
 164 The discovery of the Higgs boson in 2012 by the LHC experiments [40, 41] marked
 165 the ultimate confirmation of a long history of successful predictions by the SM.

¹⁶⁶ 1.2 Neutrinos: tiny cracks in the Standard Model

¹⁶⁷ To our current knowledge, neutrinos are the most abundant fermion in the Universe.
¹⁶⁸ And yet, they are maybe the most mysterious particle in the SM: they generate
¹⁶⁹ theoretical puzzles and experimental challenges. In this section, we treat neutrinos
¹⁷⁰ within and beyond the SM and describe the make up of their interaction with matter.

¹⁷¹ 1.2.1 Neutrinos in the Standard Model

¹⁷² Neutrino can be introduced in the SM as left-handed massless Weyl spinors. The
¹⁷³ Dirac equation of motion for a free field

$$(i\gamma^\mu \partial_\mu - m)\psi = 0 \quad (1.3)$$

¹⁷⁴ for a fermionic field

$$\psi = \psi_L + \psi_R \quad (1.4)$$

¹⁷⁵ is equivalent to the equations

$$i\gamma^\mu \partial_\mu \psi_L = m\psi_R \quad (1.5)$$

¹⁷⁶

$$i\gamma^\mu \partial_\mu \psi_R = m\psi_L \quad (1.6)$$

¹⁷⁷ for the chiral fields ψ_R and ψ_L , whose evolution in space and time is coupled
¹⁷⁸ through the mass m . If the fermion is massless, the chiral fields decouple and the
¹⁷⁹ fermion can be described by a single Weyl spinor with two independent compo-
¹⁸⁰ nents [114]. Pauli initially rejected the description of a physical particle through
¹⁸¹ a single Weyl spinor because of its implication of parity violation. In fact, since
¹⁸² the spatial inversion operator throws $\psi_R \leftrightarrow \psi_L$, parity is conserved only if both chi-
¹⁸³ ral components exist at the same time. For the neutrino introduction in the SM,
¹⁸⁴ experiments came in help of the theoretical description. The constraint of parity

¹⁸⁵ conservation weakened after Wu's experiment in 1957 [117]. Additionally, there was
¹⁸⁶ no experimental indication for massive neutrinos, nor evidence of interaction via the
¹⁸⁷ neutrino right-handed component.

¹⁸⁸ The symmetry group $SU(2)_L \otimes U(1)_Y$ is the only group relevant for neutrino
¹⁸⁹ interactions. The SM electroweak lagrangian is the most general renormalizable la-
¹⁹⁰ grangian invariant under the local symmetry group $SU(2)_L \otimes U(1)_Y$. The lagrangian
¹⁹¹ couples the weak isotopic spin doublets and singlets described in Table 1.1 with the
¹⁹² gauge bosons A_a^μ ($a = 1,2,3$) and B^μ , and Higgs doublet $\Phi(x)$:

$$\begin{aligned} \mathcal{L} = & i \sum_{\alpha=e,\mu,\tau} \bar{L}'_{\alpha L} \not{D} L'_{\alpha L} + i \sum_{\alpha=1,2,3} \bar{Q}'_{\alpha L} \not{D} Q'_{\alpha L} \\ & + i \sum_{\alpha=e,\mu,\tau} \bar{l}'_{\alpha R} \not{D} l'_{\alpha R} + i \sum_{\alpha=d,s,b} \bar{q}'^D_{\alpha R} \not{D} q'^D_{\alpha R} + i \sum_{\alpha=u,c,t} \bar{q}'^U_{\alpha R} \not{D} q'^U_{\alpha R} \\ & - \frac{1}{4} A_{\mu\nu} A^{\mu\nu} - \frac{1}{4} B_{\mu\nu} B^{\mu\nu} \\ & + (D_\rho \Phi)^\dagger (D^\rho \Phi) - \mu^2 \Phi^\dagger \Phi - \lambda (\Phi^\dagger \Phi)^2 \\ & - \sum_{\alpha,\beta=e,\mu,\tau} \left(Y_{\alpha\beta}^l \bar{L}'_{\alpha L} \Phi l'_{\beta R} + Y_{\alpha\beta}^{l*} \bar{l}'_{\beta R} \Phi^\dagger L'_{\alpha L} \right) \\ & - \sum_{\alpha=1,2,3} \sum_{\beta=d,s,b} \left(Y_{\alpha\beta}^D \bar{Q}'_{\alpha L} \Phi q'^D_{\beta R} + Y_{\alpha\beta}^{D*} \bar{q}'^D_{\beta R} \Phi^\dagger Q'_{\alpha L} \right) \\ & - \sum_{\alpha=1,2,3} \sum_{\beta=u,c,t} \left(Y_{\alpha\beta}^U \bar{Q}'_{\alpha L} \tilde{\Phi} q'^U_{\beta R} + Y_{\alpha\beta}^{U*} \bar{q}'^U_{\beta R} \tilde{\Phi}^\dagger Q'_{\alpha L} \right). \end{aligned} \quad (1.7)$$

¹⁹³ The first two lines of the lagrangian summarize the kinetic terms for the fermionic
¹⁹⁴ fields and their coupling to the gauge bosons $A_a^{\mu\nu}$, $B^{\mu\nu}$ ¹. The third line describes
¹⁹⁵ the kinetic terms and the self-coupling terms of the gauge bosons. The forth line is
¹⁹⁶ the Higgs lagrangian, which results in the spontaneous symmetry breaking. The last
¹⁹⁷ three lines describe the Yukawa coupling between fermions and the Higgs field, origin
¹⁹⁸ of the fermions' mass.

1. In gauge theories the ordinary derivative ∂_μ is substituted with the covariant derivative D_μ . Here $D_\mu = \partial_\mu + igA_\mu \cdot I + ig'B_\mu \frac{Y}{2}$, where I and Y are the $SU(2)_L$ and $U(1)_Y$ generators, respectively.

199 The coupling between left-handed and right-handed field generates the mass term
200 for fermions. The SM assumes only left-handed components for neutrinos, thus im-
201 plying zero neutrino mass. Since any linear combination of massless fields results in a
202 massless field, the flavor eigenstates are identical to the mass eigenstates in the SM.

203 1.2.2 Neutrino Oscillations

204 The determination of the flavor of a neutrino dynamically arises from the correspond-
205 ing charged lepton associated in a change current interaction; for example, a ν_e is a
206 neutrino which produces an e^- , a $\bar{\nu}_\mu$ is a neutrino which produces a μ^+ , *etc.* The
207 neutrino flavor eigenstates $|\nu_\alpha\rangle$, with $\alpha = e, \mu, \tau$, are orthogonal to each other and
208 form a base for the weak interaction matrix.

209 Overwhelming experimental data show that neutrinos change flavor during their
210 propagation [100]. This phenomenon, called “neutrino oscillations”, was predicted
211 first by Bruno Pontecorvo in 1957 [101]. Neutrino oscillations are possible only if
212 the neutrino flavor eigenstate are not identical to the mass eigenstates. Thus, the
213 observation of neutrino oscillation results in the first evidence of physics beyond the
214 Standard Model. A minimal extension of the SM introduces three mass eigenstates,
215 $|\nu_i\rangle$ ($i = 1, 2, 3$), whose mass m_i is well defined. The unitary Pontecorvo-Maki-
216 Nakagawa-Sakata matrix transforms the mass base into the flavor base as follows

$$|\nu_\alpha\rangle = U_{PMNS} |\nu_i\rangle, \quad (1.8)$$

217 with

$$U_{PMNS} = \begin{bmatrix} c_{12} & s_{12} & 0 \\ -s_{12} & c_{12} & 0 \\ 0 & 0 & 1 \end{bmatrix} \begin{bmatrix} c_{13} & 0 & s_{13}e^{-i\delta} \\ 0 & 1 & 0 \\ -s_{13}e^{-i\delta} & 0 & c_{13} \end{bmatrix} \begin{bmatrix} 1 & 0 & 0 \\ 0 & c_{23} & s_{23} \\ 0 & -s_{23} & c_{23} \end{bmatrix} \begin{bmatrix} e^{i\alpha_1} & 0 & 0 \\ 0 & e^{i\alpha_2} & 0 \\ 0 & 0 & 1 \end{bmatrix} \quad (1.9)$$

where c , e and s stand respectively for cosine and sine of the corresponding mixing angles (θ_{12} , θ_{23} and θ_{13}), δ is the Dirac CP violation phase, α_1 and α_2 are the eventual Majorana CP violation phases. Experimental results on neutrino oscillations are generally reported in terms of the mixing angles and of the squared mass splitting $\Delta m_{ab}^2 = m_a^2 - m_b^2$, where a and b represent the mass eigenstates. A summary of the current status of experimental results, albeit partial, is given in table 1.2.

Table 1.2: Summary of experimental results on neutrino oscillation parameters. **ADD CITATIONS**

	Value	Precision	Experiment
θ_{23}	45°	9.0%	Super Kamiokande, MINOS, Nova, MACRO
$-\Delta m_{32}^2$	$2.5 \cdot 10^{-3} \text{ eV}^2$	1.8%	
θ_{12}	34°	5.8%	SNO, Gallex, SAGE, KamLAND
$-\Delta m_{12}^2$	$7.4 \cdot 10^{-5} \text{ eV}^2$	2.8%	
θ_{13}	9°	4.7%	DAYA Bay, RENO
$-\Delta m_{32}^2$	$2.5 \cdot 10^{-3} \text{ eV}^2$	1.8%	

1.2.3 Make up of Neutrino Interactions

All neutrino experiments involving the detection of single neutrinos are concerned with neutrino interactions (and neutrino cross sections) on nuclei. Given the invisible nature of the neutrino, characterizing the products of its interaction is the only method to a) assess the neutrino presence, b) detect its flavor in case of a charge current interaction and c) eventually reconstruct its energy.

Historically, neutrino interactions with the nucleus in the GeV region are divided into three categories into three categories whose contributions change as a function

of increasing neutrino energy:: quasi elastic (QE), resonant (RES), and deep inelastic (DIS) scattering. All current and forthcoming oscillation experiments on neutrino beams live in the 0.1-10 GeV transition region, which encompasses the energy where the QE neutrino-nucleus interaction transitions into RES and then into DIS. For scattering off free nucleons, neutrino and antineutrino QE charge current scattering refers to the process $\nu_l n \rightarrow l^- p$ and $\bar{\nu}_l p \rightarrow l^+ n$ where a charged lepton and single nucleon are ejected in the elastic interaction. Resonant scattering refers to an inelastic collision producing a nucleon excited state (Δ, N^*) – the resonance – which then quickly decays, most often to a nucleon and single-pion final state. DIS refers to the head-on collision between the neutrino and a parton inside the nucleon, producing hadronization and subsequent abundant production of mesons and nucleons. In addition to such interactions between the neutrino and a single component of the nucleus, neutrinos can also interact with the nucleus as a whole, albeit more rarely, a well documented process called coherent meson production scattering [57]; the signature of such process is the production of a distinctly forward-scattered single meson final state, most often a pion. This simple picture of neutrino interactions works rather well for scattering off of light nuclear targets, such as the H₂ and D₂ of bubble chamber experiments [63], but the complexity of the nuclear structure for heavier nuclei such as argon complicates this model.

As we will discuss in Chapter 2, the properties of argon make it a good candidate for an interacting medium in neutrino experiments; in particular the density of its interaction centers increases the yield of neutrino interactions and allows for relatively compact detectors. Though, the choice of a relatively heavy nuclear target comes at the cost of enhancing nuclear effects which modify the kinematic and final state of the neutrino interaction products.

Nuclear effects can potentially affect neutrino event rates, final state particle emission, neutrino energy reconstruction, and the neutrino/antineutrino ratios, carrying

259 deep implications for oscillation experiments. Even in the case of “simple” QE scat-
260 tering, intra-nuclear hadron rescattering and correlation effects between the target
261 nucleons can cause the ejection of additional nucleons in the final state, modifying
262 the final state kinematics and topology. In the case of resonant and DIS scattering,
263 the hadronic interactions of meson and nucleons produced in the decay of the res-
264 onance or during hadronization complicate this picture even more. A large source
265 of uncertainty in modeling nuclear effects in neutrino interactions come from mesons
266 interactions (and re-interactions) in the nucleus, e.g., pion re-scattering, charge ex-
267 change, and absorption.

268 A renewed interest for neutrino cross section measurements surged in recent years,
269 along with a lively discussion on the data reporting; the historical method of reporting
270 the neutrino cross section as a function of the neutrino energy or momentum trans-
271 fered shakes under the weight of its dependency on the chosen nuclear model. On one
272 hand, correcting for nuclear effects in neutrino interaction can introduce unwanted
273 sources of uncertainty and model dependency especially due to the mis-modeling of
274 the meson interactions. On the other, avoiding this correction makes a comparison
275 between neutrino interactions on different target nuclei extremely difficult.

276 Data on neutrino scattering off many different nuclei are available for both charged
277 current (CC) and neutral current (NC) channels, as summarized in [63]. A summary
278 of the results on QE, resonant and DIS scattering for neutrinos and antineutrinos from
279 accelerators on different target is reported in Figure 1.1, where the (NUANCE) [37]
280 event generator is used as comparison with the theory.

281 1.3 Beyond the Standard Model

282 The discovery of neutrino oscillation and its implication of non-zero neutrino mass
283 mark the beginning of a new, exciting era in neutrino physics: the era of physics Be-

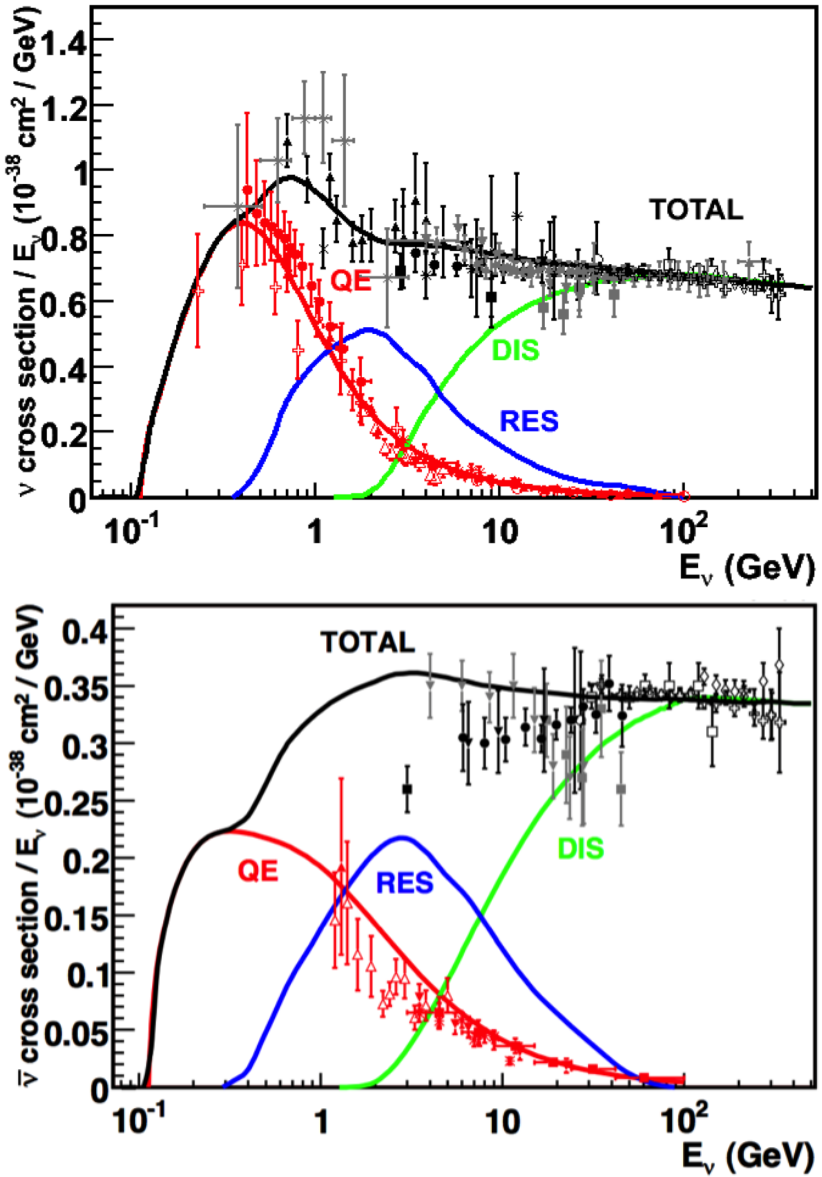


Figure 1.1: Total neutrino (top) and antineutrino (bottom) CC cross sections per nucleon divided by neutrino energy as a function of energy as reported in [63]. Predictions for the total (black), the QE (red), resonant (blue) and DIS (green) are provided by the NUANCE generator. The quasi-elastic scattering data and predictions have been averaged over neutron and proton targets (isoscalar target).

284 yond the Standard Model (BSM) at the intensity frontier. We are currently searching
285 for new, deeper theories that can accommodate neutrinos with tiny but non-zero
286 masses, while remaining consistent with the rest of the Standard Model.

287 **1.3.1 Open Questions in Neutrino Physics**

288 On one hand, the last three decades of experiments in neutrino oscillations brought
289 spectacular advancements in the understanding of the oscillations pattern, measuring
290 the neutrino mixing angles and mass splitting with a precision of less than 10%. On
291 the other, they opened the field for a series of questions needing experimental answers.

292 **Sterile neutrinos.** Hints to the existence of at least one additional neutrino,
293 in the form of various anomalies, have been puzzling physicists almost from the be-
294 ginning of neutrino oscillation searches. Originally designed to look for evidence of
295 neutrino oscillation, the Liquid Scintillator Neutrino Detector (LSND) [53] provided
296 a first conflicting result with the Standard Model expectation of only three neutrinos.

297 A second conflicting result has also been provided by the MiniBooNE experiment [49].

298 The LSND and MiniBooNE ν_e and $\bar{\nu}_e$ appearance results, known as the “LSND and
299 MiniBooNE anomalies” [14, 15, 23], may be interpreted under the assumption of a new
300 right-handed neutrino. The additional neutrino needs to be “sterile”, i.e needs not
301 to couple with the electroweak force carriers, in order to meet the constraint imposed
302 by the measurement of the width of the Z boson [2]. The new sterile neutrino would
303 mainly be composed of a heavy neutrino ν_4 with mass m_4 such that $m_1, m_2, m_3 \ll m_4$
304 and $\Delta m^2 = \Delta m_{14}^2 \sim [0.1 - 10] \text{ eV}^2$. The introduction of sterile neutrinos is an ap-
305 pealing line of thinking, since this renormalizable generalization of the SM has the
306 potential to impact long standing questions in high energy physics and cosmology:
307 light sterile neutrinos are candidates for dark matter particles and there are ideas
308 that the theory could be adjusted to explain the baryon asymmetry of the Universe
309 via leptogenesis [70].

310 **CP Violation In Lepton Sector.** The measurement of non-zero value for the
 311 oscillation parameter θ_{13} allows the exploration of low-energy CP violation in the lep-
 312 ton sector at neutrino long baseline oscillation experiments, enabling the possibility
 313 to measure the Dirac CP-violating phase δ . Exciting theoretical results tie δ directly
 314 to the generation of the baryon asymmetry of the Universe at the Grand Unified
 315 Theory scale **a couple of cit would be nice**. According to the theoretical model de-
 316 scribed in [99], for example, leptogenesis can be achieved if $|\sin \theta_{13} \sin \delta| > 0.11$, i.e.
 317 $\sin \delta > 0.7$.
 318 The asymmetry in the oscillation probability of neutrinos and antineutrinos is the ob-
 319 servable sensitive to the Dirac CP-violating phase δ leveraged in neutrino oscillation
 320 experiments. Using the parameterization of the PMNS matrix shown in Equation
 321 1.9, the difference between the probability of $\nu_e \rightarrow \nu_\mu$ oscillation and the probability
 322 of $\bar{\nu}_e \rightarrow \bar{\nu}_\mu$ oscillation can be parametrized as follows [38],

$$P_{\nu_e \rightarrow \nu_\mu} - P_{\bar{\nu}_e \rightarrow \bar{\nu}_\mu} = J \cos \left(\pm \delta - \frac{\Delta_{31} L}{2} \right) \sin \left(\frac{\Delta_{21} L}{2} \right) \sin \left(\frac{\Delta_{31} L}{2} \right) \quad (1.10)$$

323 where

$$J = \cos \theta_{13} \sin 2\theta_{13} \sin 2\theta_{12} \sin 2\theta_{23} \quad (1.11)$$

324 is the Jarlskog invariant [80], L the neutrino baseline, i.e. the distance between
 325 the neutrino production and detection points, and Δ_{ab} a factor proportional to the
 326 sign and magnitude of the mass splitting. From these equations, it is clear how the
 327 relative large value of θ_{13} is a happy accident necessary not to completely suppress
 328 the sensitivity to CP violation. The equations also show how the sensitivity to δ is
 329 tied to the measurement of the least precisely measured mixing angle, θ_{23} (via the
 330 $\sin 2\theta_{23}$ term) and to an other unknown quantity, the neutrino “mass hierarchy” (via
 331 the Δ_{ab} terms). The precise determination of θ_{23} is often referred as to “the octant
 332 problem”. Current experimental results [3, 12] are consistent with $\theta_{23} = 45^\circ$, which

333 would imply maximal mixing between ν_μ - ν_τ , hinting to an intriguing new symmetry.
334 Therefore, a precise measurement of θ_{23} is of great interest for theoretical models of
335 quark-lepton universality [73, 91, 104], whose quark and lepton mixing matrices are
336 proportional to the deviation of θ_{23} from 45°.

337 **Neutrino mass hierarchy.** The “mass hierarchy” problem refers to the unknown
338 ordering of the value of absolute mass of the neutrino mass eigenstates. Current
339 oscillation experiments are sensitive only to the magnitude of the mass splitting, and
340 not directly to its sign. In a framework where the lightest neutrino mass (arbitrarily)
341 corresponds to the first eigenstate m_1 , it is unknown whether $m_2 - m_1 < m_3 - m_1$
342 (Normal Hierarchy) or $m_2 - m_1 > m_3 - m_1$ (Inverted Hierarchy). The mass hierarchy
343 affects not only the sensitivity to CP violation searches in long baseline oscillation
344 experiments, but also the sensitivity to determine whether neutrinos are Majorana
345 particles in neutrinoless double beta decay experiments.

346 **Majorana or Dirac?** Evidence of neutrino oscillations demands the introduction
347 of a mechanism which can give mass to the neutrinos. This mechanism should possibly
348 also explain why neutrino masses are at least six orders of magnitude lower than the
349 electron mass (the second lightest SM fermion). In a description of neutrinos as Dirac
350 4-component spinors, the neutrino field acquires mass via the Higgs mechanism as
351 any other fermion of the SM. In this case, the neutrino mass is given by $m_a = \frac{y_a^\nu v}{\sqrt{2}}$,
352 where v is the Higgs VEV and y_a^ν is the Yukawa coupling between the Higgs and the
353 neutrino. The smallness of neutrino masses can only be pinned on a tiny Yukawa
354 coupling which is not justified by the theory.

355 In 1937, Majorana demonstrated that the introduction of a two components spinor is
356 sufficient to describe a massive fermion [90]. The Dirac equations of motion for the
357 chiral fields (equations 1.5 and 1.6) hold true in the case of two components spinor
358 under the assumption that the chiral components ψ_R and ψ_L are correlated through
359 the charge conjugation matrix \mathcal{C} , $\psi_R = \mathcal{C}\bar{\psi}_L$. Therefore the theory is applicable only

360 to neutral fermions. Neutrinos are the only neutral elementary particles in the SM
361 – the only possible Majorana particle candidate. This theory constructs a neutrino
362 Majorana mass term \mathcal{L}_5 of the following form in the Higgs unitary gauge

$$\mathcal{L}_5 = \frac{1}{2} \frac{gv^2}{\mathcal{M}} \nu_L^T \mathcal{C}^\dagger \nu_L, \quad (1.12)$$

363 where g is the coupling coefficient, v the Higgs VEV and \mathcal{M} a constant with the
364 dimension of the mass proportional to the scale of new physics. The \mathcal{L}_5 term would
365 introduce a non-renormalizable term in the lagrangian, since it has dimensions of
366 energy to the fifth power. This is not allowed in the SM lagrangian; however, the
367 existence of such terms is plausible if we consider the SM as an effective theory
368 at low energy, manifestation of the symmetry breaking of a more general theory at
369 higher energy, e.g. a Grand Unified Theory (GUT), and not the definitive theory.
370 The mass term in eq 1.12 implies the neutrino mass to be $m = \frac{gv^2}{\mathcal{M}}$. The coupling
371 coefficient can be of the order of any other fermion's coupling coefficient, since the
372 smallness of neutrino masses is achieved by the big value of the new physics mass
373 scale alone. This vanilla formulation is the conceptual basis for many flavors of *see-*
374 *saw mechanism* [119], which we will not discuss here in any detail. However, it is
375 fascinating how the puzzle of the neutrino mass hints to the existence of a deeper and
376 more complete theory.

377 From a kinematic point of view, Dirac and Majorana neutrinos satisfy the same
378 energy-momentum dispersion relationship. Thus, it is impossible to discern the neu-
379 trino nature through kinematic effects such as neutrino oscillations. Neutrinoless
380 double beta decay searches are the most promising way to understand the nature of
381 the neutrino and are therefore subject of great theoretical and experimental interest.
382 Observation of the lepton number violating process $0\nu\beta\beta$ would imply neutrinos have
383 a Majorana component. Depending on the mass hierarchy, the theory also predicts

384 $0\nu\beta\beta$ exclusion regions and confirmation of the sole Dirac component for neutrinos [43].

386

387 1.3.2 Towards a more fundamental theory: GUTs

388 Despite its highly predictive power, a number of conceptual issues arise in the SM
389 which disfavor it to be a good candidate for a fundamental theory.

390 The SM does not include a suitable dark matter candidate and a mechanisms
391 that accounts for the baryon asymmetry of the universe. Additionally, up to a total
392 of 25 parameters remain seemingly arbitrary and need to be fitted to data: 3 gauge
393 couplings, 9 charged fermion masses, 3 mixing angles and one CP phase in the CKM
394 matrix, the Higgs mass and quartic coupling, θ_{QCD} , 3 neutrino mixing angles, 1 Dirac
395 phase and, eventually, 2 Majorana phases.

396 From a group theory perspective, the SM has a rather complex group structure,
397 where a gauge group is formed with the direct product of other three groups as shown
398 in eq. 1.1. Drawing a parallel with the electroweak symmetry breaking mechanism,
399 where the $SU(2)_L \otimes U(1)_Y$ is recovered from $U(1)_{EM}$, an interesting line of simplification
400 for the SM group structure would be to devise a similar mechanism where
401 $SU(3)_C \otimes SU(2)_L \otimes U(1)_Y$ is recovered from an hypothetical larger group. IS THIS
402 CORRECT? Just as the electroweak unification becomes evident at energies higher
403 than the Higgs VEV, a direct manifestation of Grand Unification Theories (GUTs)
404 would occur at even higher energies.

405 As the smallness of neutrino masses suggests the existence of a higher mass scale,
406 an other, even stronger, hint to Grand Unification comes from the slope of running
407 of the coupling constants. The coupling constants for the electromagnetic, weak and
408 strong interactions in the SM vary as a function of the interaction energy as shown
409 in figure 1.2; they do not exactly meet under the current experimental constraints,

⁴¹⁰ but their trend is interesting enough to push for the construction of theories where
⁴¹¹ perfect unification is achieved through the addition of new particles.

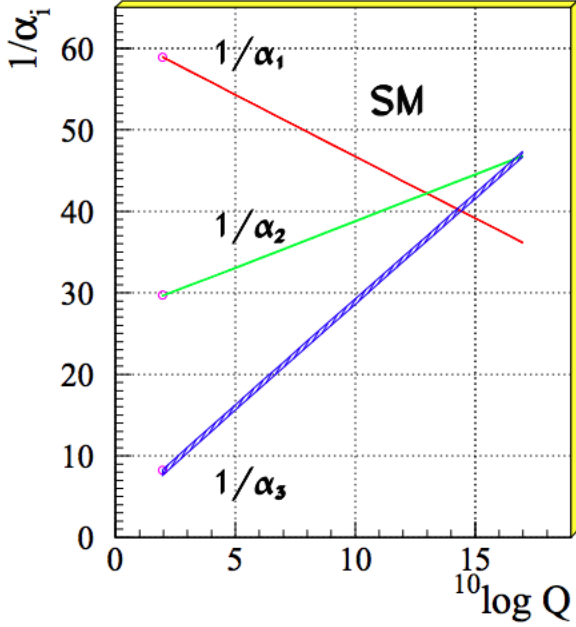


Figure 1.2: Evolution of the inverse of the three coupling constants in the Standard Model as a function of the momentum transferred, [84].

SU(5). The smallest simple group containing $SU(3)_C \otimes SU(2)_L \otimes U(1)_Y$ is $SU(5)$, as shown first by Georgi and Glashow in [67]. Quarks and leptons in this group fit the $\bar{5}$ and 10 representations. The representation for left-handed fermions are the following

$$\bar{5} = (\nu_e, e^-)_L + \bar{d}_L \quad (1.13)$$

$$10 = e_L^+ + \bar{u}_L + (u, d)_L, \quad (1.14)$$

⁴¹² while the boson structure gains a new couple of super heavy bosons (X,Y)

$$24 = \underbrace{(8, 1)}_{\text{gluons}} + \underbrace{(1, 3) + (1, 1)}_{W^\pm, Z, \gamma} + \underbrace{(3, 2) + (\bar{3}, 2)}_{X, Y \text{ bosons}}. \quad (1.15)$$

⁴¹³ Nice features such as charge quantization and the identity between the positron

414 and proton charge value come directly from the group structure. The new super
415 heavy bosons are colored and form a weak doublet. Their are the mediator of the
416 interaction that turns quarks into leptons, leading to predict the existence of processes
417 that violate baryon number, such as $p \rightarrow \pi^0 + e^+$ (see fig 1.8, right). The prediction
418 for proton decay lifetime, $\tau_p \sim \frac{M_X^4}{m_p^5} \sim 10^{30 \pm 1.5}$ years, is unfortunately experimentally
419 disproved by IMB and Super-Kamiokande [4, 28].

420 **SO(10).** More complicated group structures, such as SO(10) are still viable
421 candidates for GUT. SO(10) includes the same type of X and Y bosons as SU(5).
422 Right-handed massive neutrinos are embedded in the construction of the irreducible
423 representation of SO(10). Different patterns of SO(10) symmetry breaking to recover
424 the SM are possible and lead to different predictions for the proton decay lifetime;
425 some of these predictions are not excluded by the experiments [85].

426 **SUSY GUTs.** Supersymmetry theories allow for another family of GUTs. In
427 SUSY, every fundamental particle in the SM has a “superpartner”, identical in each
428 quantum number except for the spin-statistics: the fermion supersymmetric partners
429 are bosons and vice versa. Collider experiments (mainly LHC) constrain the mass of
430 the supersymmetric partners to be very heavy [?]. The SU(5), SU(10) groups with
431 a SUSY twist are the basic groups for SUSY GUTs. From the phenomenology point
432 of view, SUSY models tend to push the proton decay life time higher by a factor of
433 four, they solve the “hierarchy problem”, and they also predict new channels for the
434 proton decay. In particular they predict the presence of kaons in the final product,
435 with a dominant mode of $p \rightarrow K^+ \bar{\nu}$. Predictions on the proton decay lifetime depend
436 on the chosen SUSY model; again, some of the predictions are not excluded by the
437 experiments [88, 89, 108].

438 **1.4 Motivations for Hadronic Cross Sections in Ar-**
439 **gon**

440 Critical challenges await the next decade of high energy physics at the intensity
441 frontier. Following the recommendation of the latest Particle Physics Project Priori-
442 tization Panel [105], the US is dedicating substantial resources to the development of
443 a short- and long- baseline neutrino program to address many of open questions in
444 neutrino physics today. This program pivots on the Liquid Argon Time Projection
445 Chamber (LArTPC) detector technology which will be described in Chapter 2.

446 The main goals of these research programs include:

- 447 - the assessment of the existence of right-handed sterile neutrinos via the study
448 of accelerator neutrinos on a short baseline (SBN),
- 449 - the determination of the sign of Δm_{13}^2 (or Δm_{23}^2), i.e., the neutrino mass hier-
450 archy via the study of accelerator neutrinos on a long baseline (DUNE),
- 451 - the determination of the octant, i.e. whether θ_{23} is maximal, via the study of
452 accelerator neutrinos on a long baseline (DUNE),
- 453 - the determination the status of CP symmetry in the lepton sector, via the study
454 of accelerator neutrinos on a long baseline (DUNE),
- 455 - the search for observables predicted by GUTs, such as proton decay via the
456 study of non accelerator physics in massive underground detectors (DUNE).

457 **1.4.1 Pion-Argon Total Hadronic Cross Section**

458 This section outlines the importance of the pion-argon total hadronic cross section in
459 the context of the current and upcoming liquid argon neutrino experiments, SBN and
460 DUNE. We describe the signal signature and historic measurements of pion-nucleus

461 cross section, as well as the implementation of these cross sections in the current
462 version of the simulation package used by LArIAT.

463 π^- Ar Cross Section in the Context of Neutrino Searches

464 As outlined in 1.2.3, neutrino experiments use the products of neutrino interactions
465 to identify the energy and flavor of the incoming neutrino. Pions are a common
466 product of neutrino interaction, especially in resonant scattering, DIS and coherent
467 pion production. For neutrino experiments in argon, there are two main reasons
468 why understanding pion hadronic interactions with argon is important: to model the
469 behavior of the pion inside the target nucleus and to model the behavior of the pion
470 during its propagation inside the detector medium.

471 Assumptions on the nuclear modeling and on the interaction of hadrons inside the
472 nucleus performed at the level of the neutrino event generator bridge the measure-
473 ment of the products of a neutrino interaction to the reconstruction of the neutrino
474 energy and flavor. Thus, understanding pion hadronic interactions with the nucleus is
475 particularly important to model correctly resonant, DIS and coherent pion production
476 in neutrino interactions. For example, in case of resonant scattering,

$$\nu_l + N \rightarrow l + \Delta/N^* \rightarrow l + \pi + N', \quad (1.16)$$

477 the Δ and N^* and excited states will decay hadronically in matters of $\sim 10^{-24}$ s
478 inside the nucleus producing pions which will have many chances to re-interact
479 as they exit the target medium. The decay modes for the lower mass Δ (1232) and
480 $N^*(1440)$ are listed in table 1.3.

481 The key elements of a neutrino event generators for resonance and DIS events
482 are the nuclear model and the hadron treatment (both production and transporta-
483 tion). We illustrate here the conceptual basis of the GENIE Neutrino Generator [18]

484 as an example, since GENIE is one the most popular event generators for liquid ar-
485 gon experiments. For example, the nuclear model used by GENIE for all processes
486 is a Relativistic Fermi Gas (RFG) model modified to incorporate nucleon-nucleon
487 correlations [30]. This means that the initial momentum and binding energy of the
488 struck nucleon is determined by assuming nucleons inside the nucleus are quasi-free,
489 acting independently in the mean field of the nucleus. For $A > 20$ such as argon, the
490 2-parameter Woods-Saxon shell model for density function is used. The GENIE mod-
491 ule INTRANUKE [83] is used to simulate final-state interactions (FSI) which model
492 hadron re-interactions inside the nucleus. This module places the outgoing parti-
493 cles in the nucleus and propagates them using the “hA model”. In the INTRANUKE
494 hA model, hadrons can undergo at most one FSI per event. When possible, external
495 hadron-nucleus scattering data are used to tune INTRANUKE. Since no data is avail-
496 able for Argon, GENIE uses an interpolation of data from heavier and lighter nuclei
497 for the pion-argon cross section leading to large (10?s of %) resultant uncertainties in
498 the INTRANUKE module.

499 Once the pion has left the target nucleus, the pion-argon hadronic cross section also
500 plays an important role in the pion transportation inside the argon medium: processes
501 such as pion absorption or pion charge exchange can greatly modify the topology of
502 a neutrino interactions in the detector and lead to significant modifications in the
503 event classification. Being able to reconstruct the details of pions inside the detector
504 is an imperative for modern liquid argon neutrino experiment to achieve the design
505 resolution for their key physics measurements.

506 π^- -Ar Hadronic Interaction: Signal Signatures

507 Strong hadronic interaction models [48, 68] predict the pion interaction processes with
508 argon in the [100 - 1200] MeV energy range. The total hadronic π^- -Ar interaction
509 cross section is defined as the one related to the single process driven only by the

510 strong interaction which is dominant in the considered energy range. In measuring
511 the “total” cross section, we include both the elastic and reaction channels, regardless
512 of the final state,

$$\sigma_{Tot} = \sigma_{Elastic} + \sigma_{Reaction}; \quad (1.17)$$

513 the reaction channel is further characterized by several exclusive channels with defined
514 topologies,

$$\sigma_{Reaction} = \sigma_{Inelastic} + \sigma_{abs} + \sigma_{chex} + \sigma_{\pi prod}. \quad (1.18)$$

515 A summary of the pion final states in order of pion multiplicity for the reaction
516 channel is given in table 1.4. Pion capture and pion decay at rest dominate the
517 cross section under 100 MeV. We define pion capture as the process determining the
518 formation of a pionic atom and the subsequent pion’s end of life. Stopping negative
519 pions can form pionic argon, where the negative pion plays the role of an orbital
520 electron. Since the pion mass is two orders of magnitude greater than the electron
521 mass, the spatial wave form of the pion will overlap more with the nucleus compared
522 to the electron case. After the electromagnetic formation of the pionic atom, the
523 pion will get quickly absorbed by the nucleus, which is put in an excited state. The
524 nucleus then de-excites with the emission of low energy nucleons and photons. Pion
525 capture is dominant compared to pion decay, the other important process for very
526 low energy pions. The decay of a pion is governed by the weak force; the pion decay
527 life time is $\tau_\pi = 2.6 \times 10^{-8}$ s and the main decay mode is $\pi^- \rightarrow \mu^- + \bar{\nu}_\mu$ (BR 99.98%).
528 Since pion capture can be considered an electromagnetic process and pion decay is a
529 weak process, this energy region is purposely excluded from the hadronic cross section
530 measurement.

531 **Previous measurements: Lighter and Heavier Nuclei**

532 Many experiments with pion beams have studied the hadronic interaction of pions on
533 light and heavy materials, such as He, Li, C, Fe, Pb [36]. However, data on argon are
534 rare: the total differential hadronic cross section has never been measured before on
535 argon. Simulation packages such as Geant4 base their pion transportation for argon
536 on data from lighter and heavier nuclei: the goal of LArIAT’s dedicated measurement
537 on argon is to bridge this gap in data, thus reducing the uncertainties related to pion
538 interactions in argon in both neutrino event generators and in simulation packages of
539 pion transportation.

540 The shape of the pion-nucleus interaction cross section in the energy range con-
541 sidered shows the distinct features indicating the presence of a resonance. In fact, the
542 mean free path of a pion of kinetic energy between 100 and 400 MeV is much shorter
543 than the average distance between nucleons (which is of the order of 1 fm). There-
544 fore, the pion interacts with surface nucleons. A Δ resonance is often produced in
545 the interaction, which subsequently decays inside the nucleus. Experimental results
546 on several nuclei as reported in [36] are shown in Figure 1.3; it is interesting to notice
547 here how the shape of the Δ resonance becomes less pronounced as a function of the
548 mass number of the target nucleus. Pion interactions with heavier nuclei also shift the
549 peak of the resonance at lower energy; this effect is due to kinematic considerations
550 and to the difference in propagation of the Δ inside the nucleus. Multiple scattering
551 effect modify the resonance width, which is larger than the natural-decay width. As
552 an example of a fairly well studied target, Figure 1.4 reports the negative pion cross
553 section on Carbon for the elastic and reaction² channels, and their sum [54].

2. This paper calls “inelastic interaction” what we refer as to “reaction channel”.

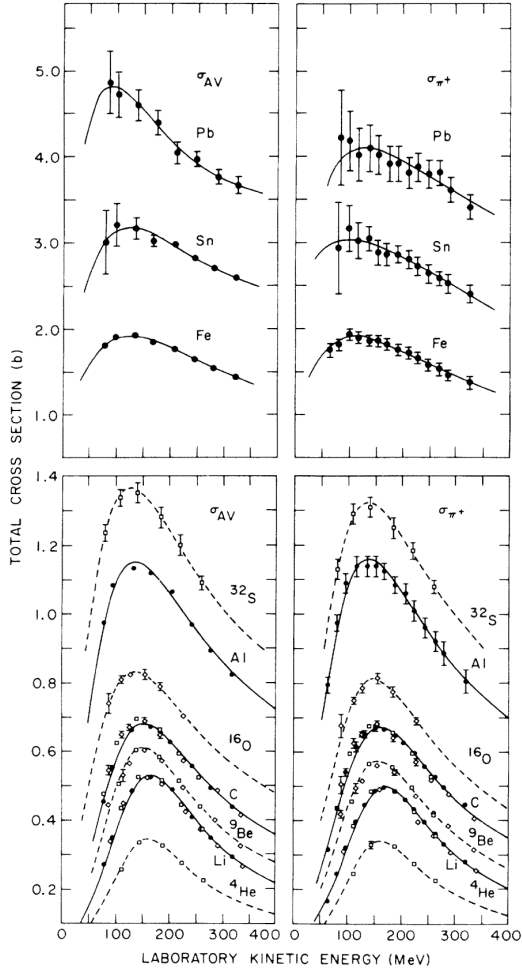


Figure 1.3: Pion-nucleus total cross sections: σ_{π^+} for positive pions (right) and σ_{AV} (left) for the average between positive and negative pions $\sigma_{AV} = \frac{\sigma_{\pi^+} + \sigma_{\pi^-}}{2}$ in the Δ resonance region. The error bars include estimates of systematic uncertainties. The curves are the results of fits to the data assuming a Breit-Wigner shape. This summary plot is reported in [36] and uses data from [51, 115].

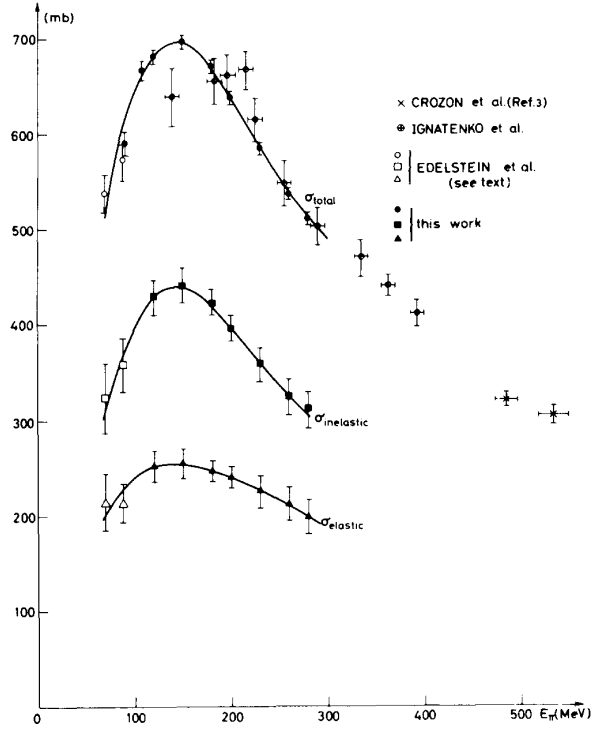


Figure 1.4: Negative pion nucleus total, elastic and reaction cross sections on ^{12}C as from [54].

554 Negative Pion Interaction Cross Section in Simulation Packages

555 LArIAT uses Geant4 as the default simulation package. In particular, pions (and
 556 kaons) transportation is achieved through the Geant4 FTFP_BERT physics list. In
 557 this physics list, Geant4 uses the Bertini cascade model [116] to simulate the products
 558 of the pion-nucleus interaction as well as secondary hadronic re-interactions inside
 559 the target nucleus (intra-nuclear cascade). The target nucleus is represented as a
 560 continuous gas where the nuclear potential follows concentrical shells whose depths
 561 approximate the Woods-Saxon shape. The CERN-HERA compilations [112, 113] of
 562 hadron-nucleon interaction data is the data base used for the decision making process
 563 after the cascade is invoked. The cross section model determines if the pion inter-
 564 acts, the eventual type of interaction and the interaction multiplicity. For hadron
 565 projectiles with energy less than 20 GeV, Geant4 reports the uncertainty on the cross

566 section model to be about the size of the error bars on the data used, or about 10%,
567 increasing to 20-30% in energy regions where data is sparse.

568 The relevance of the GENIE generator for neutrino physics and its basic working
569 principles have been outlined earlier in this section. Given GENIE’s modularity,
570 information on hadron-nucleus interactions can be extracted from the INTRANUKE
571 module and directly compared against the Geant4 predictions. The work in [96]
572 reviews the current status of negative and positive pion simulation in Geant4 and
573 GENIE for ^{12}C , ^{56}Fe , and ^{40}Ca . From that work, we report the results for ^{12}C in
574 Figure 1.5 as it allows a direct comparison between Geant4, GENIE and and pion
575 re-scattering data. Geant4 predictions for π^- on Carbon are in good agreement with
576 data over the entire spectrum spectrum, while GENIE predictions seem to show some
577 features at around 500 MeV and 900 MeV, maybe due to higher resonances in the hA
578 model. From the same work, we also report the negative pion cross section on ^{40}Ca
579 in Figure 1.6, since this is the nuclear medium closest to argon. The predictions from
580 both Geant4 and GENIE agree with data in the high energy region; the Geant4 and
581 GENIE predictions diverge in the resonance region, where data is not available. These
582 few examples highlight how cross section data for the specific nucleus considered in
583 the neutrino experiments is fundamental to inform the Monte Carlo simulation.

584 For the LArIAT simulation of the MC sample used in the π^- argon total hadronic
585 cross section measurement we use the Geant4 Bertini Cascade model, whose predic-
586 tions for the total, elastic and reaction hadronic cross sections are show in Figure
587 1.7.

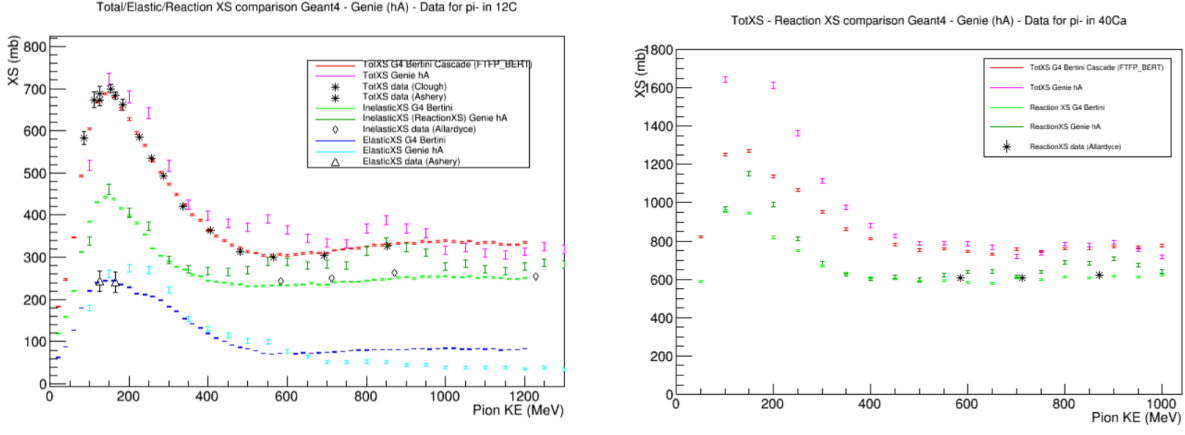


Figure 1.5: Total, elastic and reaction cross section for π^- on ^{12}C . Comparison between results from Geant4 simulation (Bertini cascade model), Genie simulation (hA model), and experimental data [22, 51, 52, 107].

Figure 1.6: Total, elastic and reaction cross section for π^- on ^{40}Ca . Comparison between results from Geant4 simulation (Bertini cascade model), Genie simulation (hA model), and experimental data [52].

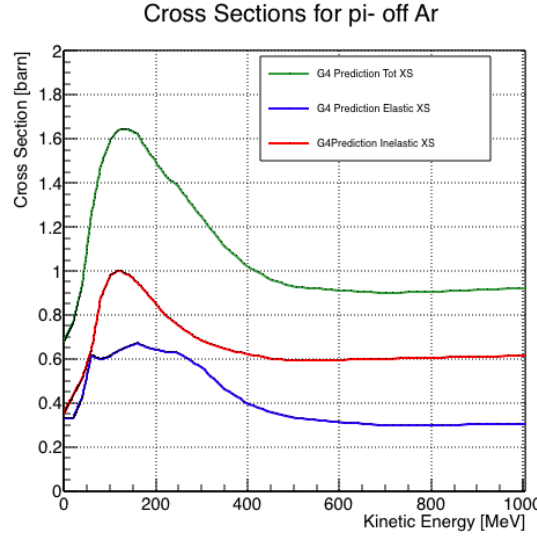


Figure 1.7: Total, elastic and reaction hadronic cross section for π^- -argon implemented in Geant4 10.01.p3.

Resonance	Decay Mode	Lifetime (s)
Δ (1232) $3/2^+$	$\Delta^{++}(\text{uuu}) \rightarrow p\pi^+$ $\Delta^+(\text{uud}) \rightarrow n\pi^+$ $\Delta^+(\text{uud}) \rightarrow p\pi^0$ $\Delta^0(\text{udd}) \rightarrow n\pi^0$ $\Delta^0(\text{udd}) \rightarrow p\pi^-$ $\Delta^-(\text{ddd}) \rightarrow n\pi^-$	$\sim 5.6 \times 10^{-24}$
N^* (1440) $1/2^+$	$N^* \rightarrow N\pi$ $N^* \rightarrow N\pi\pi$	$\sim 2.2 \times 10^{-24}$

Table 1.3: Main decay modes of the lightest Delta resonance and Nucleon excited state.

N π in FS	Channel Name	Reaction	Notes
0	Pion Absorption, σ_{abs}	$\pi^-(np) \rightarrow nn$ (2-body abs) $\pi^-(nnp) \rightarrow nnn$ (3-body abs) $\pi^-(npp) \rightarrow pnn$ (3-body abs) $\pi^-(nnpp) \rightarrow pmn$ (Multi-body abs)	Suppressed on single nucleon by energy conservation: the process occurs on at least two nucleons system.
1	Elastic Scattering, σ_{el}	$\pi^- + N \rightarrow \pi^- + N$	Scattering on nucleon or nucleus, the target is left in ground state
1	Charge Exchange, σ_{chea}	$\pi^- + p \rightarrow \Delta^0 \rightarrow \pi^0 + n$ $\pi^- + N \rightarrow \pi^+ +$ nucleons	Single charge exchange: charged pion converts into neutral pion Double charge exchange: charged pion converts into opposite charge pion
1	Inelastic Scattering, σ_{inel}	$\pi^- + p \rightarrow \Delta^0 \rightarrow \pi^- + p$ (knock-out) $\pi^- + n \rightarrow \Delta^- \rightarrow \pi^- + n$ (knock-out)	Other possible reactions: Pure Inelastic scattering: population of low energy bound excited states Nuclear break-up with nucleons or fragments knock-out
2+	Pion Production, $\sigma_{\pi prod}$	$\pi^- + N \rightarrow \geq 2\pi +$ nucleons	Possible if pion K.E ≥ 500 MeV/c

Table 1.4: Summary of negative pion hadronic interactions of the reaction channel as a function of the pion multiplicity in the final state in the energy range [100-1200] MeV.

588 **1.4.2 Kaon-Argon Total Hadronic Cross Section**

589 This section outlines the importance of the kaon-argon total hadronic cross section.
590 We start by discussing the measurement in the context of nucleon decay searches. We
591 then describe the signal signature and historical measurements of kaon-nucleus cross
592 section, as well as the implementation of this cross sections in the current version of
593 the simulation package used by LArIAT.

594 **K⁺Ar Cross section in the Context of Nucleon Decay Searches**

595 Baryon number is accidentally conserved in the Standard Model. Even though no
596 baryon number violation has been experimentally observed thus far, no underlying
597 symmetry in line with the Noether paradigm [95] explains its conservation. As shown
598 in section 1.3.2, almost all Grand Unified Theories predict at some level baryon num-
599 ber violation in the form of nucleon decay on long time-scales. Given the impossibil-
600 ity to reach grand unification energy scales with collider experiments (Energy Scale
601 $> 10^{15}$ GeV), an indirect proof of GUTs is needed. The experimental observation of
602 nucleon decay may be the only viable way to explore these theories.

603 In case of nucleon decay discovery, the dominant decay mode may uncover addi-
604 tional information about the GUT type. Supersymmetric GUTs [24, 45] prefer the
605 presence of kaons in the products of the decay, e.g. $p \rightarrow K^+ \bar{\nu}$ (see fig 1.8, left).
606 Gauge mediated GUTs, in which new gauge bosons are introduced that allow for the
607 transformation of quarks into leptons, and vice versa, prefer the mode $p \rightarrow e^+ \pi^0$ (see
608 fig 1.8, right).

609 LArIAT tiny active volume makes it impossible for the experiment to place com-
610 petitive limits on nucleon decay searches. However, LArIAT provides excellent data
611 to characterize kaons in liquid argon for the ‘‘LAr golden mode’’, $p \rightarrow K^+ \bar{\nu}$. The
612 result of these studies will affect future proton decay searches in LArTPCs. Previous
613 work has been done to assess the potential identification efficiency for different decay

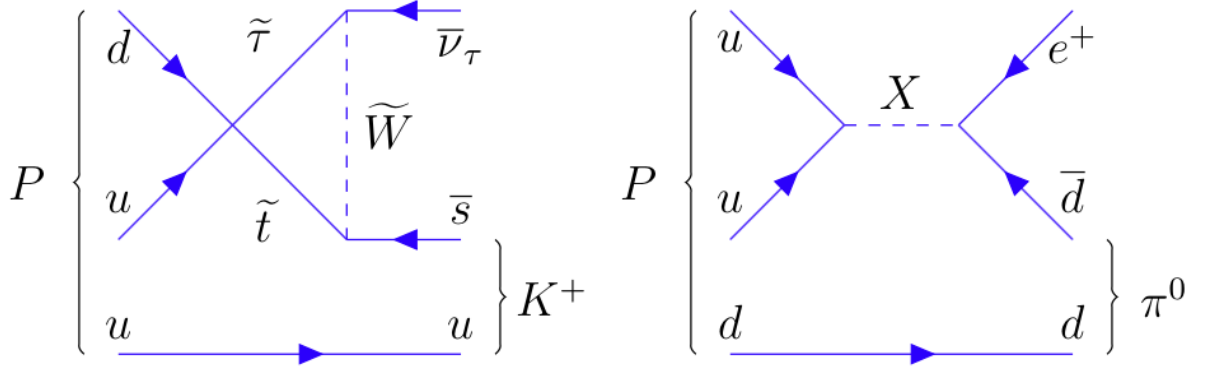


Figure 1.8: Feynman diagrams for proton decay “golden modes”: $p \rightarrow K^+\bar{\nu}$ for supersymmetric GUTs on the left and $p \rightarrow e^+\pi^0$ for gauge-mediated GUTs on the right.

614 modes in a LArTPC [50], but, as the time of this writing, no study of kaon selection
 615 efficiency in LArTPCs has been performed on data. The K^+ -Ar interaction cross
 616 section has never been measured before and can affect the possibility of detecting
 617 and measuring kaons when produced in a proton decay event. Kaon interactions with
 618 argon can distort the kaon energy spectrum as well as change the topology of single
 619 kaon events. In a LArTPC, non-interacting kaons appear as straight tracks with a
 620 high ionization depositions at the end (Bragg peak). The topology of interacting
 621 kaons can be quite different. In case of elastic scattering, a distinct kink will be
 622 present in the track. In case of inelastic scattering the Bragg peak will not be present
 623 and additional tracks will populate the event. Performing the total hadronic K^+ -Ar
 624 cross section measurement on data serves the double purpose of identifying the rate
 625 of “unusual” topologies (kinks and additional tracks) and of developing tools for kaon
 626 tracking in LAr.

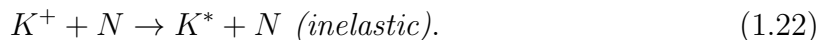
627 **K^+ Ar Hadronic Interaction: Signal Signatures**

The interaction of a mildly relativistic charged kaon with an argon nucleus is determined largely by the strong force. The total hadronic K^+ -Ar interaction cross section

is defined as the one related to the single (hadronic) process driven only by the strong interaction. In this case, “total” indicates all strong interactions regardless of the final state. This condition purposefully includes both elastic and inelastic (reaction) channels. Indeed, the total cross section section can be then decomposed into

$$\sigma_{Tot} = \sigma_{Elastic} + \sigma_{Reaction}.$$

628 For the LArIAT cross section analysis, the kaons considered span a momentum
 629 inside the TPC from 100 MeV/c to 800 MeV/c. In this energy range, the relevant
 630 K-Nucleon interactions are according to [62]:



631 **Previous Measurements: Lighter and Heavier Nuclei**

632 In general, measurements on kaon cross sections are extremely scarce. The mea-
 633 surement of the kaon interaction cross section would bring the additional benefit
 634 of reducing the uncertainties associated with hadron interaction models adopted in
 635 MC simulations for argon targets, beneficial for both proton decay studies and kaon
 636 production from neutrino interaction studies, where the uncertainties for final state
 637 interaction models are big [46].

638 Figure 1.9 shows a 1997 measurement on several elements as performed by Fried-
 639 mann et al. [64]. As a reference, this paper measures a σ_{Tot} for Si of 366.5 ± 4.8
 640 mb and a σ_{Tot} for Ca of 494.6 ± 7.7 mb at 488 MeV/c. The cross section for argon

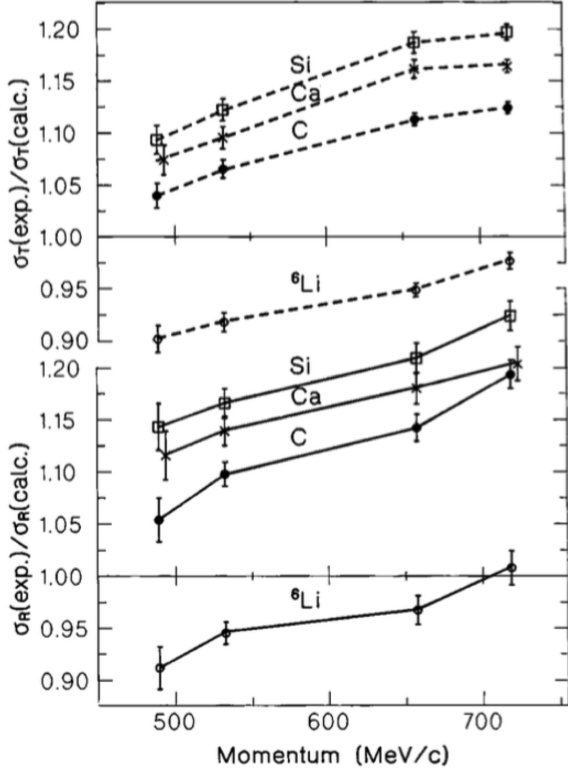


Figure 1.9: Ratios between experimental and calculated cross sections as from [64].
Top: Total cross sections.
Bottom: reaction cross sections.

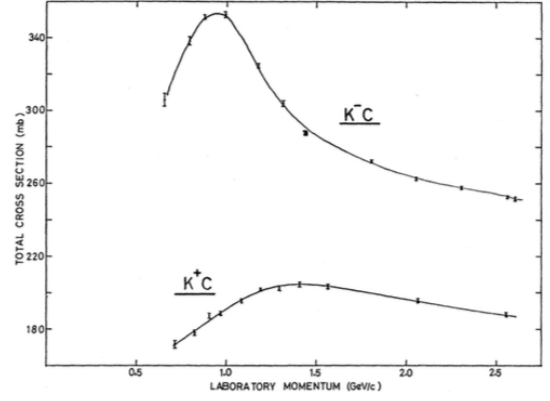


Figure 1.10: Total K^+ and K^- cross sections on carbon as from [32].

is expected to lie in between these two measurements. Additional data on the kaon cross section are provided by Bugg et al. [32]. Bugg performs a measurement of the total K^+ and K^- cross sections on protons and deuterons over the range of 0.6-2.65 GeV/c, as well as a measurement of the total K^+ and K^- cross sections on carbon for a number of momenta; the results of this paper on carbon are reported in Figure 1.10.

647 Kaon Interaction Cross Section for thin target in Geant4

Since the kaon cross section in argon has never been measured before, simulation packages tune kaon transportation in argon by extrapolation from lighter and heavier nuclei. LArIAT uses the Geant4 suite for particle transportation. Since kaon data on

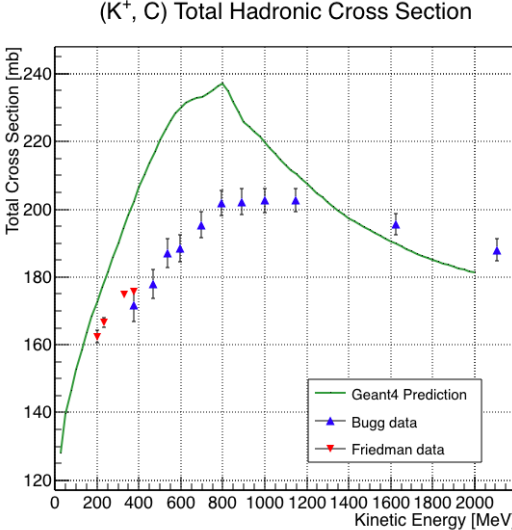


Figure 1.11: Total hadronic cross section for carbon implemented in Geant4 10.01.p3 with overlaid with the Bugg and Friedman data.

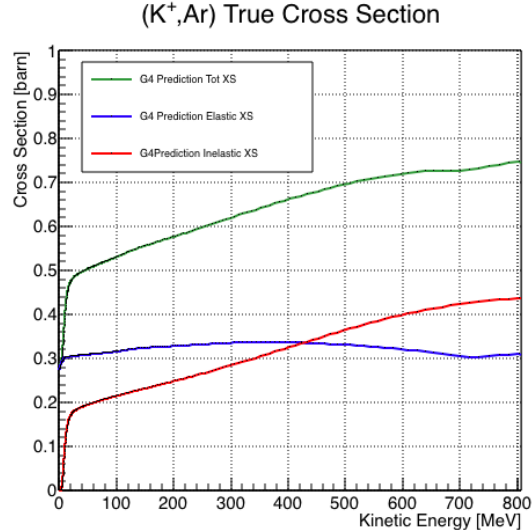


Figure 1.12: Total, elastic and reaction hadronic cross section for K^+ -argon implemented in Geant4 10.01.p3.

carbon are available, we used it as a metric to evaluate the Geant4 prediction performances. Figure 1.11 shows the total hadronic cross section for carbon implemented in Geant4 10.01.p3 overlaid with the Bugg and Friedman data. Unfortunately, version 10.01.p3³ of Geant4, which is the version used for the simulation in this work, does not reproduce the data for carbon closely. On one hand, this evidence makes us even more wary when using the Monte Carlo in simulating the kaon-argon interactions. On the other, it further highlights the importance of the kaon measurement. For the LArIAT simulation of the MC sample used in the K^+ argon total hadronic cross section measurement we use the Geant4 Bertini Cascade model, whose predictions for the total, elastic and reaction hadronic cross sections are show in Figure 1.12.

3. It should be noted that the latest Geant4 version, 10.03.p3, uses a different parametrization for the kaon cross section and retrieves a better agreement with data.

661 Chapter 2

662 Liquid Argon Detectors at the

663 Intensity Frontier

664 “*Don’t you know, honey,*
665 *Ain’t nobody ever gonna love you, the way I try to do?*”
666 – Janis Joplin, Cry Baby, 1971 –

667 In the next few years, LArTPCs will be the tools to answer some of the burning
668 questions in neutrino physics today. This chapter illustrates the operational principles
669 of this detector technology, as well as the scope of the key detectors in the US liquid
670 argon program – SBN, DUNE and LArIAT.

671 2.1 The Liquid Argon Time Projection Chamber

672 Technology

673 In this section, we outline an extremely brief history of Time Projection Chambers
674 as particle detectors, focusing on their incarnation as Argon detectors for neutrino
675 physics. We further describe the working principles of Liquid Argon Time Projection

676 Chambers, leading to the description of the event reconstruction in LArTPC.

677 2.1.1 TPCs, Neutrinos & Argon

678 David Nygren designed the first Time Projection Chamber (TPC) in the late 1970s [97]
679 for the PEP-4 experiment, a detector apt to study electron-positron collisions at the
680 PEP storage ring at the SLAC National Accelerator Laboratory. From the original
681 design in the seventies – a cylindrical chamber filled with methane gas – the TPC
682 detector concept has seen many incarnations, the employment of several different
683 active media and a variety of different particle physics applications, including, but
684 not limited to the study of electron/positron storage rings (e.g. PEP4, TOPAZ,
685 ALEPH and DELPHI), heavy ions collisions in fixed target and collider experiments
686 (e.g. EOS/HISS and ALICE), dark matter (ArDM), rare decays and capture (e.g.
687 TRIUMF, MuCap), neutrino detectors and nucleon decay (ICARUS, SBN, DUNE),
688 and neutrino less double beta decay (Next). A nice review of the history of TPCs
689 and working principles is provided in [76].

690 Several features of the TPC technology make these detectors a more versatile tool
691 compared to other ionization detectors and explain such a wide popularity. TPCs are
692 the only electronically read detector which deliver simultaneous three-dimensional
693 track information and a measurement of the particle energy loss. Leveraging on both
694 tracking and calorimetry, particle identification (PID) capabilities are enhanced over
695 a wide momentum range.

696 Historically, the active medium in ionization detectors has been in the gaseous
697 form. Carlo Rubbia first proposed the use of a Liquid Argon TPC for a neutrino
698 experiment, ICARUS [106], in 1977. Using nobles elements in the liquid form for
699 neutrino detectors is advantageous for several reasons. The density of liquids is \sim 1000
700 times greater than gases, augmenting the number of targets for neutrino's interaction
701 in the same volume, in a effort to balance the smallness of neutrino cross section. Since

Element	LAr	LXe
Atomic Number	18	54
Atomic weight A	40	131
Boiling Point Tb at 1 atm	87.3 K	165.0 K
Density	1.4 g/cm ³	3.0 g/cm ³
Radiation length	14.0 cm	2.8 cm
Moliere Radius	10.0 cm	5.7 cm
Work function	23.6 eV	15.6 eV
Electron Mobility at $E_{field} = 10^4$ V/m	0.047 m ² /Vs	0.22 m ² /Vs
Average dE/dx MIP	2.1 MeV/cm	3.8 MeV/cm
Average Scintillation Light Yield	40000 γ /MeV	42000 γ /MeV
Scintillation λ	128 nm	175 nm

Table 2.1: LAr, LXe summary of properties relevant for neutrino detectors.

the energy loss of charged particle is proportional to the target material density, as shown in the Bethe-Block equation (eq. 2.1), the increased density reflects into a proportionally higher energy loss, enhancing the calorimetry capability of detectors with a liquid active medium. Additionally, the ionization energy of liquids is smaller than gasses by the order of tens of eV. Thus, at the passage of charged particles, liquids generally produce more ionization electrons than gases for the same deposited energy, forcing the particles to deposit more energy in a shorter range. The downside of using noble liquid elements in experiments is that they require expensive cryogenic systems to cool the gas until it transitions to its the liquid form. The properties of liquid argon in comparison liquid xenon – a popular choice for dark matter and neutrinoless double beta decay detectors – are summarized in table 2.1. Albeit xenon would be more desirable than argon given some superior properties such as lower ionization energy and higher density and light yield, argon relative abundance abates the cost of argon compared to xenon, making argon a more viable choice for the construction of ton (and kilo-ton) scale neutrino detectors.

LArTPCs are some times referred as to “electronic” bubble-chambers, for the similarity in the tracking and energy resolution which is coupled with an electronic readout of the imaging information in LArTPCs. Compared to these historic detectors

720 however, LArTPC bestow tridimensional tracking and a self triggering mechanism
721 provided by the scintillation light in the liquid argon. An event display of a ν_μ CC
722 interaction candidate in the MicroBooNE detector is shown in picture 2.1 to display
723 the level of spatial details these detectors are capable of; the color scale of the image
724 is proportional to the energy deposited, hinting to these calorimetry capabilities of
the detectors.

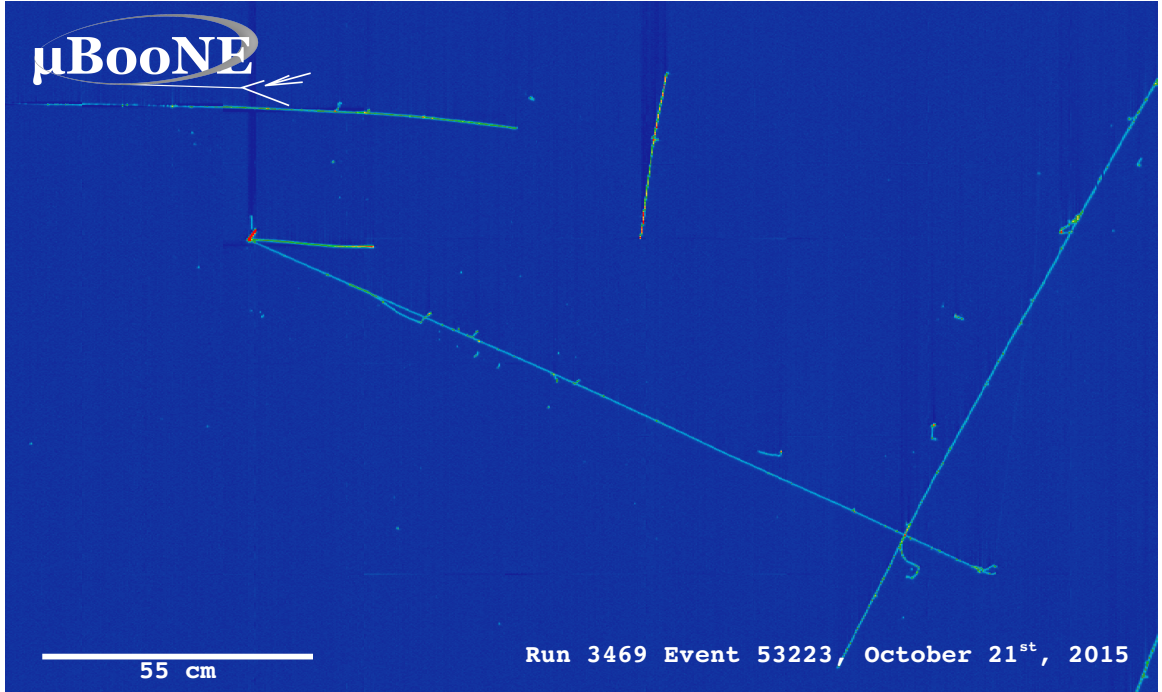


Figure 2.1: Event display of a ν_μ CC interaction candidate in the MicroBooNE detector.

725

726 2.1.2 LArTPC: Principles of Operation

727 To the bare bones, a LArTPC is a bulk of liquid argon sandwiched in a flat capacitor,
728 equipped with a light collection system, as the cartoon in 2.2 shows. A uniform
729 electric field of the order of 500 V/cm is maintained constant between the faces of the
730 capacitor. The anode is sensitive to ionization charge and it is usually made of two
731 or more planes segmented into several hundreds parallel sense wires a few millimeters
732 apart; different geometries for the anode segmentation are under study [47].

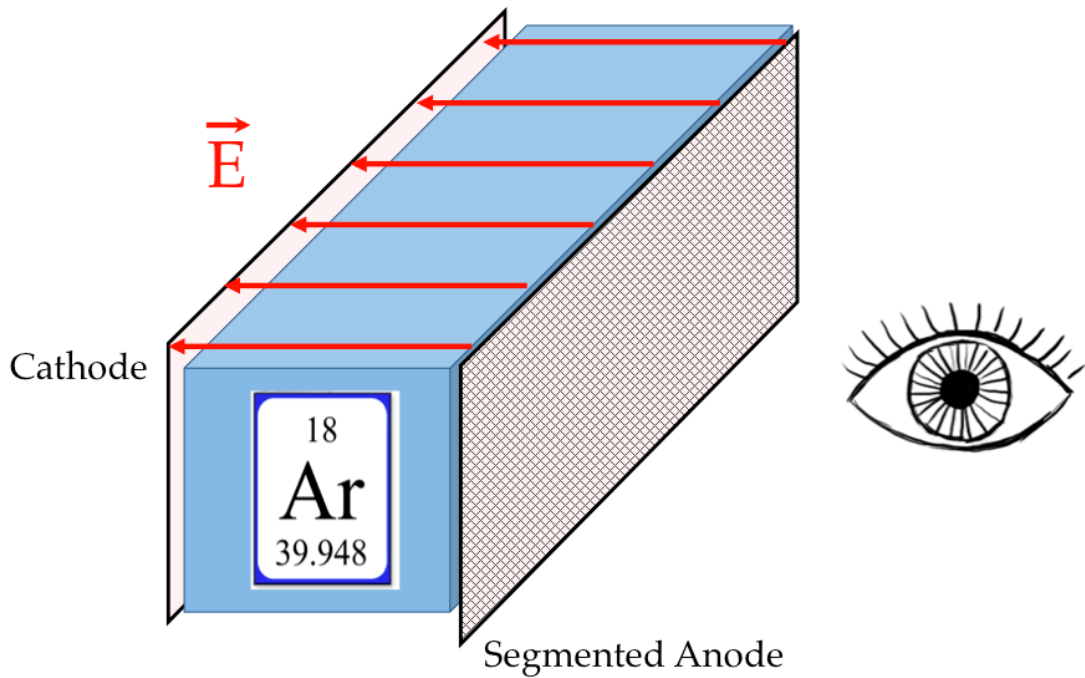


Figure 2.2: A cartoonish sketch of a LArTPC.

733 Argon ionization and scintillation are the processes leveraged to detect particles
 734 in the LArTPC active volume. When a ionizing radiation traverses the argon active
 735 volume it leaves a trail of ionization electrons along its trajectory and it excites
 736 the argon producing scintillation light – details on the production and detection of
 737 ionization charge and scintillation light are provided in 2.1.4 and 2.1.4 respectively.
 738 The optical detector sees the argon scintillation light in matters of nanoseconds.
 739 This flash of light determines the start time of an event in the chamber, t_0 . The
 740 uniform electric field drifts the ionization electrons from the production point towards
 741 the anode in order of hundreds of microseconds or more depending on the chamber
 742 dimensions¹. The anode sense wires see either an induced current by the drifting
 743 ionization charge (on induction planes) or an injection of such charge (collection

1. The ionized argon also drifts, but in the opposite directions compared to the electrons. Since the drift time is proportional to the particle mass, the ions' drift time is much longer than the electrons'. Ionized argon is collected on the cathode which is not instrumented, so it is not used to infer information about the interactions in the chamber.

744 plane). An appropriate choice of the voltage bias on each wire plane assures ideal
745 charge transparency, so that all the ionization charge is collected on the collection
746 plane and none on the induction planes.

747 The arrival time of the charge on the anode sense wires is used to measure the
748 position of the original ionizing radiation in the drift direction. In fact, since the
749 constant electric field implies that the drift velocity is also constant, the position of
750 the original ionization is simply given by the multiplication of the drift velocity by the
751 drift time, where the “drift time” is the difference between t_0 and the charge arrival
752 time on the wire planes. The spacial resolution on this dimension is limited by the
753 time resolution of the electronics or by longitudinal diffusion of the electrons. The
754 spatial information on the different wire planes maps a bi-dimensional projection of
755 the interaction pattern in the plane perpendicular to the drift direction. The spacial
756 resolution on this dimension is limited by the transverse electron diffusion in argon
757 and by the grain of the anode segmentation, i.e. the spacing between the wires in
758 the sense planes [44]. The off-line combination of the 2-D information on the wire
759 planes with the timing information allows for the 3D reconstruction of the event in
760 the chamber.

761 Since the charge deposited by the ionizing radiation is proportional to the de-
762 posited energy and the charge collected on the sense plane is a function of the de-
763 posited charge, LArTPCs allow the measurement of the energy deposit in the active
764 volume. Effects due to the presence of free charge and impurities in the active vol-
765 ume, such as a finite electron lifetime, recombination and space charge, complicate
766 the relationship between deposited and collected charge affecting the measurement of
767 the particle’s energy, as described in the next section.

768 2.1.3 Liquid Argon: Ionization Charge

769 The mean rate of energy loss by moderately relativistic elementary charge particles
 770 heavier than electrons is well described by the modified Bethe-Bloch [100] equation

$$-\frac{dE}{dx} = K z^2 \frac{Z}{A} \varrho \frac{1}{\beta^2} \left[\frac{1}{2} \ln \frac{2m_e c^2 \beta^2 \gamma^2 T_{max}}{I^2} - \beta^2 - \frac{\delta}{2} \right], \quad (2.1)$$

771 where z is the number of unit charge of the ionizing radiation, Z , A and ϱ are the
 772 atomic number, mass number and density of the medium, m_e is the electron mass,
 773 $\gamma = \frac{\beta}{\sqrt{1-\beta^2}}$ is the Lorentz factor of the ionizing radiation, T_{max} is the maximum kinetic
 774 energy which can be imparted to a free electron in a single collision, I is the mean
 775 excitation energy on eV, δ is the density correction and $K = 0.307075 \text{ MeV g}^{-1} \text{ cm}^2$ is
 776 a numerical conversion factor. The Bethe-Bloch treats the energy loss by an ionizing
 777 radiation via quantum-mechanical collisions producing ionization or an excitation in
 778 the medium as an uniform and continuous process. The density correction terms
 779 becomes relevant for incident particle with high energy, where screening effects due
 780 to the polarization of the medium by high energy particles occur.

781 Excitation and ionization of the detector medium occur in similar amounts. Since
 782 the ionizing collisions occur randomly, we can parametrize their number k in a segment
 783 of length s along the track with a Poissonian function

$$P(k) = \frac{s^k}{k! \lambda^k} e^{-s/\lambda}, \quad (2.2)$$

784 where $\lambda = 1/N_e \sigma_i$, with N_e being the electron density of σ_i the ionization cross-
 785 section per electron. About 66% of the ionizing collisions in Argon produce only
 786 a single electron/ion pair [76]; in the other cases, the transferred kinetic energy is
 787 enough for the primary electron to liberate one or more secondary electrons, which
 788 usually stay close to the original pair. Occasionally, electrons can receive enough

789 energy to be ejected with high energy, forming a so-called “ δ -ray”: a detectable short
790 track off the particle trajectory, as shown in figure 2.3. The average number of δ -ray
791 with energy $E > E_0$ per cm follows the empirical form

$$P(E > E_0) \sim \frac{y}{\beta^2 E_0}, \quad (2.3)$$

792 where y is an empirical factor depending on the medium (0.114 for gaseous Ar), and
793 β is v/c .

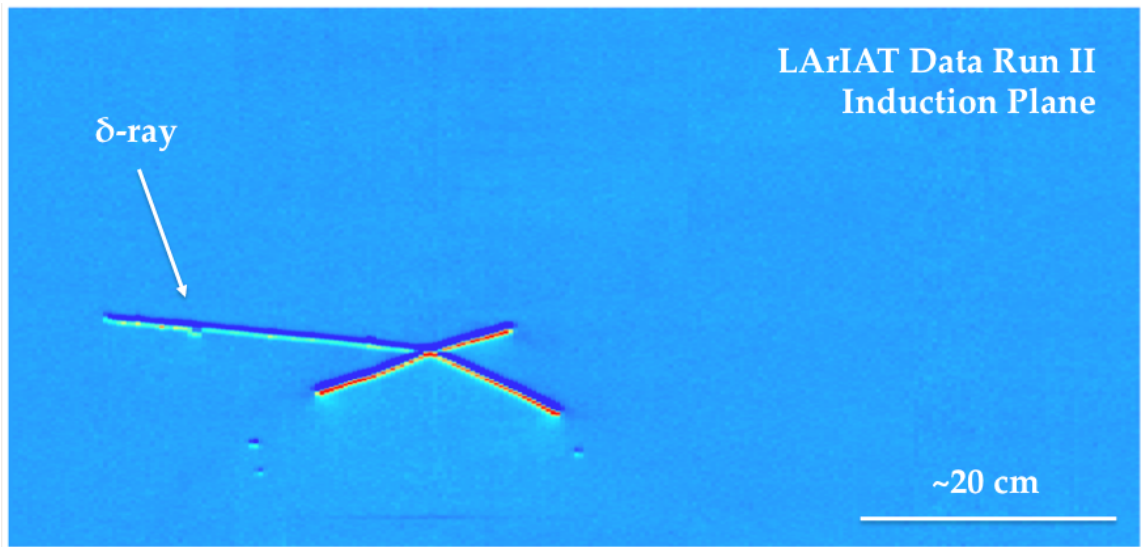


Figure 2.3: Events display for a LArIAT pion absorption candidate on the induction plane, with highlighted delta ray.

794 Purity & Electron Life Time

795 The presence of electronegative contaminants in liquid argon, such as oxygen O_2
796 and water H_2O , is particularly pernicious, since these molecules quench the charge
797 produced by the ionizing radiation. Thus, amount of charge per unit of length dQ/dx
798 collected on the collection plane depends on the charge's production point in the
799 detector: ionization produced close to the cathode will see more impurities along its
800 journey to the collection plane than ionization produced close to the anode, resulting

801 in greater attenuation of its charge. As a result, the amount of charge collected on
 802 the sense wires as a function of the traveled distance follows an exponential decay
 803 trend. The traveled distance is generally measured in terms of drift time and the
 804 characteristic time constant of the exponential decay is called electron lifetime τ_e .
 805 Figure 2.4 shows the typical life time for LArIAT data. The procedure to measure
 806 the electron lifetime in LArIAT is outlined in [103]. LArIAT small drift distance (47
 807 cm) allows for a relatively short electron life time. The life time for bigger detectors
 808 such as MicroBooNE, whose drift distance is 2.6 m, needs to be of the order of
 809 tens of milliseconds to allow a charge collection usable for physics analyses. Energy
 810 reconstruction in LArTPC applies a correction for the finite lifetime to calibrate the
 811 detector calorimetric response; details for LArIAT are provided in Section B.

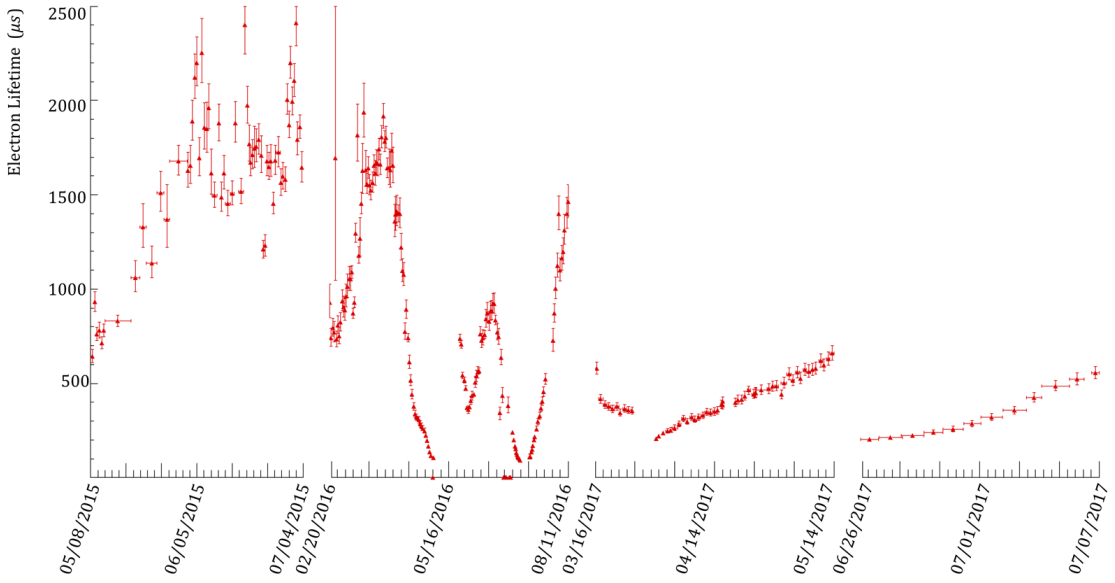


Figure 2.4: Electron lifetime during the LArIAT run period [42].

812 LArTPCs use hermetically sealed and leak-checked vessels to abate the leakage
813 and diffusion of contaminants into the system. The liquid argon filling of the volume
814 occurs after the vessel is evacuated or purged with gaseous argon [10] to reduce re-
815 maining gases in the volume. Even so, the construction of a pure tank of argon is
816 unviable, as several sources of impurity remain. In particular, impurities can come
817 from the raw argon supply, the argon filtration system and from the outgassing from
818 internal surfaces. Outgassing is a continuous diffusive process producing contami-
819 nants, especially water, even after the vessel is sealed, particularly from materials in
820 the ullage region². Since research-grade argon comes from the industrial distillation
821 of air, the impurities with the highest concentration are nitrogen, oxygen and water,
822 generally maintained under the 1 part per million level by the vendor. Even so, a
823 higher level of purity is necessary to achieve a free electron life time usable in meter
824 scale detectors. Thus, argon is constantly filtered in the cryogenic system, which
825 reduce the oxygen and water contamination to less than 100 parts per trillion. The
826 filtration system depends on the size and drift distance of the experiment and, for
827 experiments on several meters scale, it includes an argon recirculation system.

828 Recombination Effect

829 After production, ionization electrons thermalize with the surrounding medium and
830 may recombine with nearby ions. Recombination might occur either between the
831 electron and the parent ion through Coulomb attraction, as described in the geminate
832 theory [98], or thanks to the collective charge density of electrons and ions from
833 multiple ionizations in a cylindrical volume surrounding the particle trajectory, as
834 described in the columnar model [79]. Consideration on the average electron-ion
835 distance and the average ion-ion distance for argon show that the probability of

2. While the liquid argon low temperature reduces outgassing in the liquid, this process remains significant for absorptive material (such as plastic) above the surface of the liquid phase.

836 geminate recombination is low; thus recombination in argon is mainly due to collective
837 effects [5]. Since protons, kaons and stopping particles present a higher ionization
838 compared to MIPs, recombination effects are more prominent when considering the
839 reconstruction of energy deposited by these particles.

840 Theoretical descriptions of recombination based on the Birks model and the Box
841 model are provided in [29] and [111], respectively. The Birks model assumes a gaus-
842 sian spatial distribution around the particle trajectory during the entire recombina-
843 tion phase and identical charge mobility for ions and electrons. The Box model also
844 assumes that electron diffusion and ion mobility are negligible in liquid argon during
845 recombination. In these models, the fraction of ionization electrons surviving recom-
846 bination is a function of the number of ion-electron pairs per unit length, the electric
847 field, the average ion-electron separation distance after thermalization and the angle
848 of the particle with respect to the direction of the electric field – plus the diffusion
849 coefficient in the Birks model. Given the stringent assumptions, it is perhaps not sur-
850 prising that these models are in accordance to data only in specific regimes: the Birks
851 model is generally used to describe recombination for low dE/dx , the Box model for
852 high dE/dX . In LArTPC, the ICARUS and ArgoNeut experiments have measured
853 recombination in [16] and [5] respectively. Since LArIAT uses the refurbished Ar-
854 goNeut TPC and cryostat at the same electric field, LArIAT currently corrects for
855 recombination using the ArgoNeut measured recombination parameters in [5].

856 Space Charge Effect

857 Slow-moving positive argon ions created during ionization can build-up in LArTPC,
858 causing the distortion of the electric field within the detector. This effect, called
859 “space charge effect” leads to a displacement in the reconstructed position of the
860 signal ionization electrons. In surface LArTPCs the space charge effect is primarily
861 due to the rate of ionization produced by cosmic rays which is slowly drifting in the

862 chamber at all times. Surface LArTPC of the size of several meters are expected
863 to be modestly impacted from the space charge effect, where charge build-up create
864 anisotropy of the electric field magnitude of the order of 5% at a drift field of 500
865 V/cm [92]. The smallness of the LArIAT drift volume and its relatively high electric
866 field are such that the effect of space charge is expected to be negligible.

867 **2.1.4 Liquid Argon: Scintillation Light**

868 Liquid argon emits scintillation light at the passage of charged particles. LArTPCs
869 leverage this property to determine when the ionization charge begins to drift towards
870 the anode plane.

871 **Scintillation Process**

872 Scintillation light in argon peaks in the ultraviolet at a 128 nm, shown in comparison
873 to Xenon and Kypton in Figure 2.5, from [93]. The light yield collected by the optical
874 detector depends on the argon purity, the electric field, the dE/dx and particle type,
875 averaging at the tens of thousands of photons per MeV.

876 The de-excitation of Rydberg dimers in the argon is responsible for the scintillation
877 light. Rydberg dimers exist in two states: singlets and a triplets. The time constant
878 for the singlet radiative decay is 6 ns, resulting in a prompt component for the scin-
879 tillation light. The decay of the triplet is delayed by intersystem crossing, producing
880 a slow component with a time constant of ~ 1500 ns. “Self-trapped exciton lumines-
881 cence” and “recombination luminescence” are the two processes responsible for the
882 creation of the Rydberg dimers [82]. In the first process, a charged particle excites an
883 argon atom which becomes self-trapped in the surrounding bulk of argon, forming a
884 dimer; the dimer is in the singlet state 65% of the times and in the triplet state 35%
885 of the times. In case of recombination luminescence, the charged particle transfers
886 enough energy to ionize the argon. The argon ion forms a charged argon dimer state,

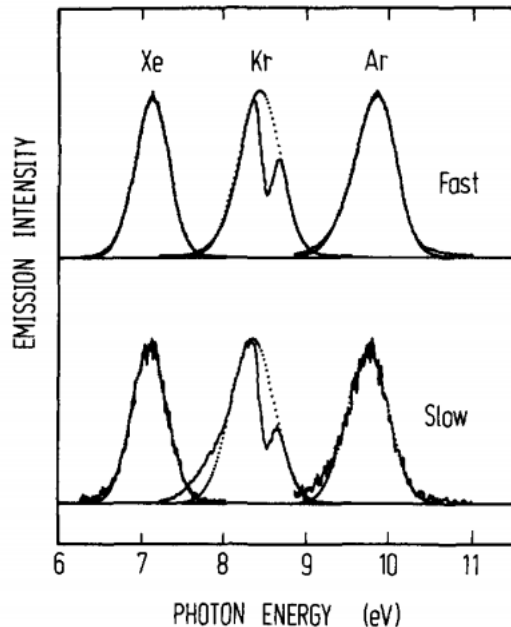


Figure 2.5: Emission spectra of the fast and slow emission components in Xenon, Krypton and Argon according to [93]. The dotted lines correspond to the Gaussian fits.

which quickly recombines with the thermalized free electron cloud. Excimer states
 are produced in the recombination, roughly half in the singlet and half in the triplet
 state. The light yield dependency on the electric field, on the dE/dx and particle
 type derives from the role of free charge in the recombination luminescence process.
 The spacial separation between the argon ions and the free electron cloud depends on
 the electric field. On one hand, a strong electric field diminishes the recombination
 probability, leading to a smaller light yield; on the other, it increases the free charge
 drifting towards the anode plane. Hence, the amount of measurable charge and light
 anti-correlates as a function of the electric field. Ionizing particles in the argon mod-
 ify the local density of both free electrons and ions depending on their dE/dx . Since
 the recombination rate is proportional to the square of the local ionization density,
 highly ionizing particles boost recombination and the subsequent light yield compared
 to MIPs. The possibility to leverage this dependency for pulseshape-based particle
 identification has been shown in [31, 87].

901 **Effects Modifying the Light Yield**

902 The production mechanism through emission from bound excimer states implies that
903 argon is transparent to its own scintillation light. In fact, the photons emitted from
904 these metastable states are not energetic enough to re-excite the argon bulk, greatly
905 suppressing absorption mechanisms. In a LArTPC however, several processes modify
906 the light yield in between the location where light is produced and the optical detector.
907 In a hypothetical pure tank of argon, Rayleigh scattering would be the most important
908 processes modifying the light yield. Rayleigh scattering changes the path of light
909 propagation in argon, prolonging the time between light production and detection.
910 The scattering length has been measured to be 66 cm [77] , shorter than the theoretical
911 prediction of ~ 90 cm [110]; this value is short enough to be relevant for the current
912 size of LArTPCs detectors. In fact, Rayleigh scattering worsen the resolution on t_0 ,
913 the start time for charge drifting, and alters the light directionality, complicating the
914 matching between light and charge coming from the same object in case of multiple
915 charged particles in the detector.

916 Traces of impurities in argon such as oxygen, water and nitrogen also affect the
917 light yield, mainly via absorption and quenching mechanisms. Absorption occurs as
918 the interaction of a 128 nm photon directly with the impurity dissolved in the liquid
919 argon. Differently, quenching occurs as the interaction of an argon excimer and an
920 impurity, where the excimer transfers its excitation to the impurity and dissociates
921 non-radiatively. Given this mechanism, it is evident how quenching is both a function
922 of the impurity concentrations and the excimer lifetime. Since the triplet states
923 live much longer than the singlet states, quenching occurs mainly on triplet states,
924 affecting primarily the slow component of the light, reducing the scintillation yield
925 and a shortening of the scintillation time constants.

926 The stringent constraints for the electron life time limit the presence of oxygen and
927 water to such a low level that both absorption and quenching on these impurity is not

expected to be significant. Contrarily, the nitrogen level is not bound by the electron life time constraints – nitrogen being an inert gas, expensive to filter. Thus, nitrogen is often present at the level provided by the vendor. The effects of nitrogen on argon scintillation light have been studied in the WArP R&D program and at several test stands. The quenching process induced by nitrogen in liquid Ar has been measured to be proportional to the nitrogen concentration, with a rate constant of $\sim 0.11 \mu\text{s}^{-1} \text{ ppm}^{-1}$; appreciable decreasing in lifetime and relative amplitude of the slow component have been shown for contamination as high as a few ppm of nitrogen [6]. For a nitrogen concentration of 2 parts per million, typical of the current generation of LArTPC, the attenuation length due to nitrogen has been measured to be ~ 30 meters [81].

Wavelength Shifting of LAr Scintillation Light

Liquid argon scintillation light is invisible for most optical detectors deployed in a LArTPC, such as cryogenic PMTs and SiPMs, since a wavelength of 128 nm is generally too short to be absorbed from most in glasses, polymers and semiconductor materials. Research on prototype SiPMs absorbing directly VUV light and their deployment in noble gasses experiment is ongoing but not mature [118]. Thus, experiments need to shift the wavelength of scintillation light to be able to detect it. Albeit deployed in different ways, neutrinos and dark matter experiments commonly use 1,1,4,4-tetraphenyl-butadiene (TPB) to shift the scintillation light. TPB absorbs the vacuum ultraviolet (VUV) light and emits in the visible at ~ 425 nm [33], with a ratio of visible photon emitted per VUV photon absorbed of $\sim 1.2:1$ [65].

Neutrino experiments typically coat their optical detector system evaporating a layer of TPB either directly on the PMTs glass surface or on acrylic plates mounted in front of the PMTs [59]; this technique allows the fast detection light coming directly from the neutrino interaction. Dark matter experiments typically evaporate TPB on

954 reflective foils mounted on the inside walls of the sensitive volume and detect the
955 light after it has been reflected; this technique leads to a higher and more uniform
956 light yield, though scattering effects for both the visible and VUV light augment
957 the propagation time and hinder directionality information [60]. In order to take
958 advantage of both these techniques, hybrid systems with PMT coating and foils are
959 being considered for the next generation of large neutrino detectors.

960 2.1.5 Signal Processing and Event Reconstruction

961 In this section we illustrate the processing and reconstruction chain of the TPC sig-
962 nals, from the pulses on the sense wire to the construction of three dimensional objects
963 with associated calorimetry. Different experiments can chose different software pack-
964 ages for their off line signal processing and event reconstruction, but a popular choice
965 for US based LArTPCs is LArSoft [39]. Based on the Art framework [71], LArSoft is
966 an event-based toolkit to perform simulation, analysis and reconstruction of LArT-
967 PCs events.

968

969 LArTPC signal processing develops in several consecutive stages that we summa-
970 rize here in the following categories: *Deconvolution, Hit Reconstruction, 2D Cluster-*
971 *ing, 3D Tracking, Calorimetry Reconstruction*. A visualization of the signal processing
972 workflow is shown in figure 2.6.

973

974 **Deconvolution.** Induction and collection planes have different field responses,
975 given the different nature of the signals on these planes: the wires on the induction
976 planes see the inductive signal of the drifting charge, while the wires on the collection
977 planes see the current derived from the charge entering the conductor. Thus, signals
978 on the induction plane are bi-polar pulse and signal on the collection plane are unipo-
979 lar pulses, see Figure 2.6 panel a). The first step in signal processing is deconvolution,

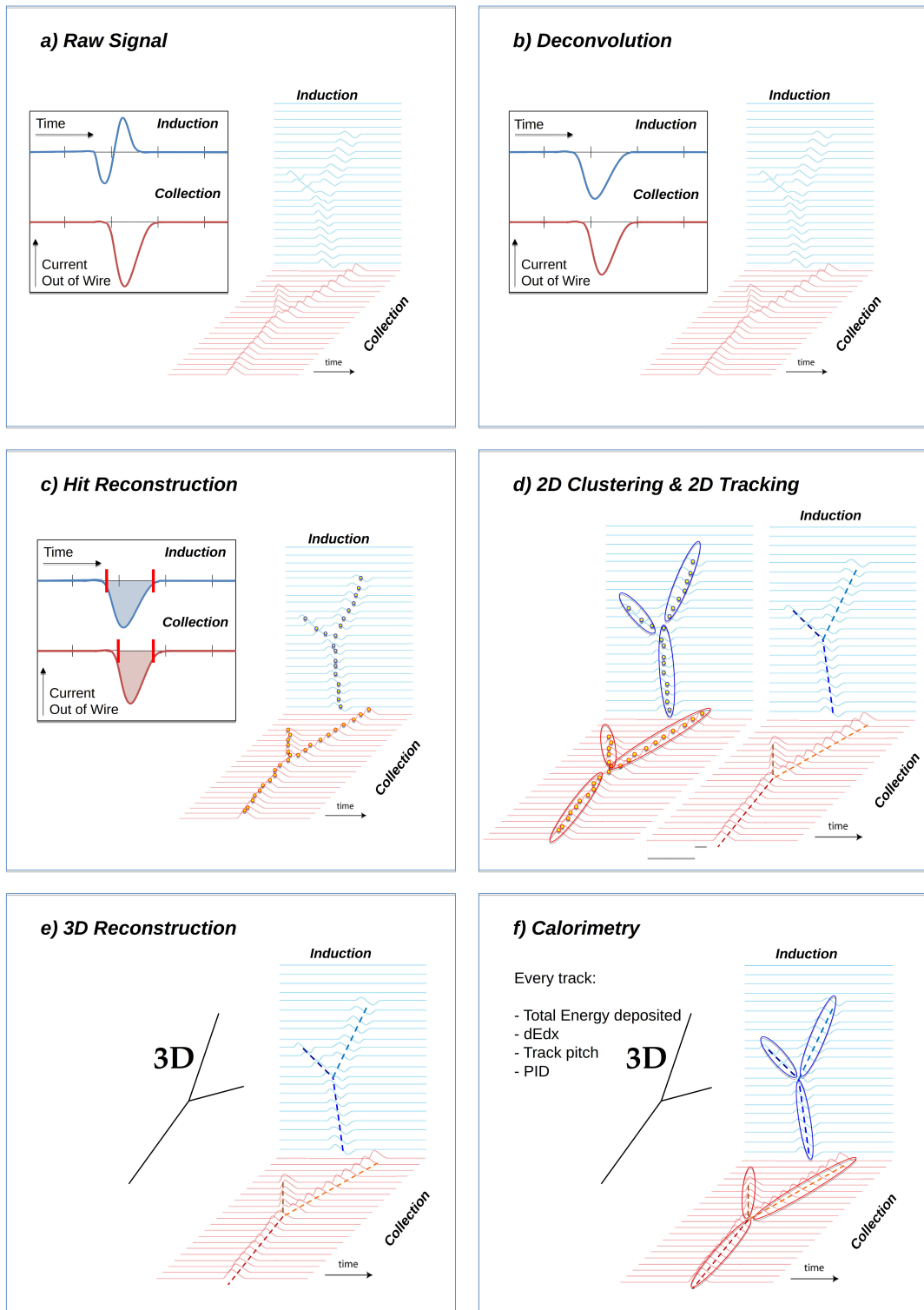


Figure 2.6: A scheme of a typical signal processing workflow in LArSoft.

980 that is a series of off-line algorithms geared towards undoing the detector effects. The
981 result of the deconvolution step is the production of a comparable set waveforms on
982 all planes presenting unipolar, approximately gaussian-like pulses (Figure 2.6 panel
983 b). Signal from all planes are treated on equal footage beyond this point. Some
984 LArTPC apply noise filtering in the frequency domain just after the deconvolution
985 to clean up wire cross talk. Since signals from the LArIAT TPC are extremely clean,
986 noise filtering is not necessary.

987

988 **Hit Reconstruction.** The second stage of the signal processing is the recon-
989 struction of hits, indicating an energy deposition in the detector. A peak finder scans
990 the deconvolved TPC waveforms for each wire on the whole readout time looking for
991 spikes above the waveform’s baseline. It then fits these peaks with gaussian shapes
992 and stores the fit parameters such as the quality of the fit, the peak time, height and
993 area under the gaussian fit. The information resulting from this process on a single
994 spike form a single reconstructed “hit”, see Figure 2.6 panel c). The next steps in
995 the event reconstruction chain will then decide if rejecting hits with poor fits. It is
996 important to notice how the height and width of the hit depend on the topology of
997 the event: for example, a particle running parallel to the wire planes will leave a series
998 of sharp hits on many consecutive wires, while a particle traveling towards the planes
999 will leave a long, wide hit on very few wires. The height of the hits and their integral
1000 is proportional to the charge collected on the wire, so it depends on the particle type.

1001

1002 The event reconstruction chain uses collection of hits to form more complex objects
1003 associated with the particles in the detector. The development of different approaches
1004 to accomplish this task is an extremely hot topic in LArTPC event reconstruction
1005 which spans from more traditional approaches such as line-clustering [26] to the use of
1006 machine learning tools [58]. Generally speaking, the scope of hit clustering and event

1007 reconstruction to provide shower-like or track like-objects with an associated energy
1008 reconstruction. This is because different particles have different topology in the de-
1009 tector – electrons and photon create electromagnetic showers, resulting in shower-like
1010 topologies, while muons and hadrons leave track-like signals. For the scope of these
1011 thesis, we will describe only LArIAT’s approach to track reconstruction even if we
1012 recognize the breath of LArTPC event reconstruction is much wider. We are inter-
1013 ested in the reconstruction of pions and kaons in the active volume, whose topology
1014 is track-like.

1015

1016 **2D Clustering Reconstruction.** The LArIAT reconstruction of track-like ob-
1017 jects starts by clustering hits on the collection and induction planes separately with
1018 the use of the TrajCluster clustering package [25]. TrajCluster looks for a collection
1019 of hits in the wire-time 2D space which can be described with a line-like 2D trajec-
1020 tory. TrajCluster reconstructs trajectories by adding trajectory points to the leading
1021 edge of the trajectory while stepping through the 2D space of hits. Several factors
1022 determine whether a hit is added to the trajectory, including but not limited to

- 1023 1. the goodness of the fit of the single hit,
- 1024 2. the charge of the hit compared to the average charge and RMS of the hits
1025 already forming the trajectory,
- 1026 3. the goodness of trajectory fit with and without the hit addition,
- 1027 4. the angle between the two lines formed by the collection of hits before and after
1028 the considered hit in the trajectory.

1029 The final product of this reconstruction stage is the collection of bidimensional clusters
1030 on each wire plane, see Figure 2.6 panel d).

1031 **3D Tracking.** The 3D tracking set of algorithms uses clusters close in time on
1032 the induction and collection planes as starting point to form a 3D track. Firstly, it

1033 construct a tentative 3D trajectory using the edges of the clusters. Then, it projected
1034 back the tentative trajectory on to the planes and adjusts the parameters of the 3D
1035 track fit such that they minimize the distance between the fit projections and the
1036 track hits in all wire planes simultaneously. Tridimensional tracking can use multiple
1037 clusters in one plane, but it can never break them in smaller groups of hits. This
1038 algorithm was first developed for the ICARUS collaboration [20]. The final product
1039 of this reconstruction stage is the formation of tridimensional objects in the TPC
1040 active volume, see Figure 2.6 panel e).

1041

1042 **Calorimetry.** The last step in the event reconstruction chain is to assign calorimetric
1043 information to the track (or shower) objects. Calorimetry is performed separately on the different planes. A multi-step procedure is needed to retrieve the energy
1044 deposited in the TPC from the charge seen by the wires. For each hit associated with
1045 the track object, the calorimetry algorithms calculate the charge seen on every wire
1046 using the area underneath the gaussian fit; then, they correct this raw charge by the
1047 electron life time, the electronic noise on the considered wire and the recombination
1048 effect. Lastly an overall calibration of the energy, explained in detail in section B,
1049 is applied and the calorimetric information for the given track is assigned. Even if
1050 calorimetry is done in 2D, it benefits from the 3D tracking information; typical information available after the calorimetric reconstruction are the total energy deposited
1051 by the particle and its stopping power dE/dx at each “track pitch”, i.e. at each 2D
1052 projection on the wire plane of the 3D trajectory.

1055 2.2 The Intensity Frontier Program

1056 This section highlights the role of Liquid Argon Time Projection Chambers at the
1057 Intensity frontier. In particular, we show the prospects for the exploration of neutrino

1058 physics (Section 2.2.1) and GUT models (Section 2.2.2) in current and forthcoming
1059 LAr experiments. In Section , we introduce LArIAT and its role in the Intensity
1060 Frontier panorama.

1061 **2.2.1 Prospects for LArTPCs in Neutrino Physics: SBN and**
1062 **DUNE**

1063 The ArgoNeut experiment [17] together the LAr R&D experiments TallBo and the
1064 Yale TPC initiated the US LArTPC neutrino program. Following the success of the
1065 ArgoNeut small TPC on the NuMI beam, a wide program of LArTPCs on neutrino
1066 beams has flourished. The construction of LArTPCs as near and far detectors at
1067 different baseline allows for the exploration of some of the fundamental questions in
1068 neutrino physics today illustrated in section 1.3.1.

1069 The Short-Baseline Neutrino (SBN) [21] program at Fermilab is tasked with con-
1070 clusively assess the nature of the “LSND and MiniBooNE anomalies” [14, 15, 23],
1071 resolving the mystery of sterile neutrinos at the eV² scale. The SBN program entails
1072 three surface LArTPCs positioned on the Booster Neutrino Beam at different dis-
1073 tances from the neutrino production in oder to fully exploit the L/E dependence of
1074 the oscillation pattern: SBND (100 m from the decay pipe), MicroBooNE (450 m),
1075 and ICARUS (600 m). Within the oscillation context, the choice of the LArTPC tech-
1076 nology for the SBN detectors changes the set of systematics with respect to LSND
1077 and MiniBooNE, whose detection techniques were both based on Cherenkov light.
1078 In particular, LArTPCs provide excellent electron/photon separation [9] lacking in
1079 Cherenkov detectors which can be leveraged to abate the photon background from
1080 neutral current interactions in ν_e searches. MicroBooNE [8], the first detector of the
1081 SBN program to be fully operational, started its first neutrino run in October 2015.
1082 MicroBooNE is a 89 ton active volume LArTPC, single drift chamber with TPC di-
1083 mensions of 2.6 m (drift) x 2.3 m (heigh) x 10.4 m (depth). MicroBooNE is positioned

at a very similar L/E on the Booster neutrino beam as MiniBooNE has the scope to directly cross check the MiniBooNE oscillation measurement. In case MicroBooNE confirms the presence of the “low energy excess” anomaly, SBND and ICARUS will provide the full measurement of the oscillation parameters. SBND and ICARUS are both dual drift chambers, whose active volume is respectively 112 ton and 600 ton. ICARUS is scheduled to become operational by the end of 2018 and SBND shortly after. Besides the oscillation analysis, the second main goals of SBN is to perform an extensive campaign of neutrino cross section measurements in argon. Given the importance of nuclear effects in (relatively) heavy materials, as discussed in section 1.2.3, both the oscillation analysis of the SBN program and the measurements of neutrino properties in DUNE will benefit from such a campaign.

On a different neutrino beam and baseline, the DUNE experiment, née LBNE [11], is the flagship experiment on the medium-long term of US-based neutrino physics, scheduled to start data taking in 2026. Shooting neutrinos from Fermilab for 800 miles to the SURF laboratory in South Dakota, DUNE is tasked with performing conclusive measurements of CP violation in the lepton sector, the neutrino mass ordering and the θ_{23} octant. The DUNE far detector will count four 10 kton LArTPCs, roughly of dimensions of 19 m (horizontally) x 18 m (vertically) x 66 m (depth).

2.2.2 Prospects for LArTPCs in GUT Physics: DUNE

The experimental exploration of a manifestation of Grand Unified Theory is possible in DUNE thanks to its sheer mass. In particular, proton decay searches are a capital topic of DUNE’s wide non-accelerator physics program. The key elements for a rare decay experiment are: massive active volume, long exposure, high identification efficiency and low background. Figure 2.7 shows the current best experimental limits on nucleon decay lifetime over branching ratio (dots). Historically, the dominant technology used in these searches has been water Cherenkov detectors: all the best

1110 experimental limits on every decay mode are indeed set by Super-Kamiokande [?, ?].
 1111 As shown in section 1.3.2, different family of GUTs predict the proton to decay in
 1112 different modes. In particular, SUSY flavored GUTs prefer the presence of kaons
 1113 in the decay products, e.g. $p \rightarrow K^+ \bar{\nu}$. It is particularly important to notice that
 1114 the kaon energy for the proton decay mode $p \rightarrow K^+ \bar{\nu}$ is under Cherenkov threshold
 1115 in water. Thus, Super-Kamiokande set the limit on the lifetime for the $p \rightarrow K^+ \bar{\nu}$
 1116 mode by relying on photons from nuclear de-excitation and on the muon tagging in
 1117 the kaon decay leptonic mode. For this reason, an attractive alternative approach to
 1118 identifying nucleon decay is the use of a LArTPCs, where the kaon is directly visible
 1119 in the detector. According to [11], DUNE will have an active volume large enough,
 1120 have sufficient shielding from the surface, and will run for lengths of time sufficient
 1121 to compete with Hyper-K, opening up the opportunity for the discovery of nucleon
 1122 decay.

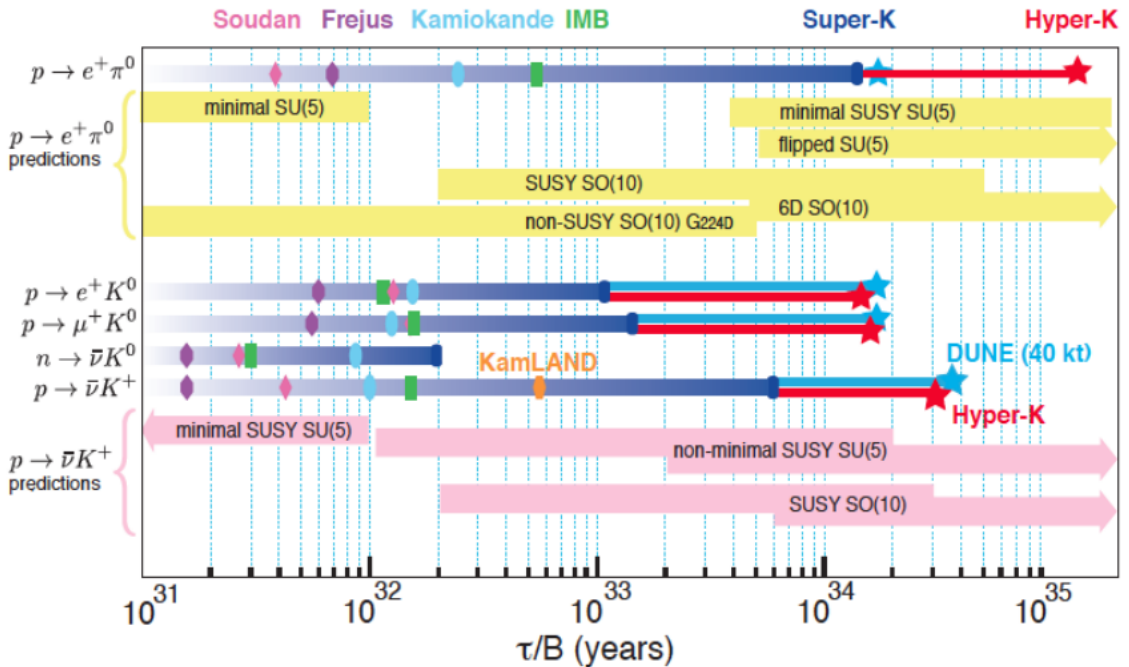


Figure 2.7: Proton decay lifetime limits from passed and future experiments.

1123 2.2.3 Enabling the next generation of discoveries: LArIAT

1124 LArIAT, a small LArTPC in a test beam, is designed to perform an extensive physics
1125 campaign centered on charged particle cross section measurements while characteriz-
1126 ing the detector performance for future LArTPCs. Since LArTPCs represent the most
1127 advanced experiments for physics at the Intensity Frontier, their complex technology
1128 needs a thorough calibration and dedicated measurements of some key quantities to
1129 achieve the precision required for the next generation of discoveries. LArIAT’s goal
1130 is to provide such calibration and dedicated measurements. The LArIAT LArTPC is
1131 deployed in a dedicated calibration test beamline at Fermilab. We use the LArIAT
1132 beamline to characterize the charge particles before they enter the TPC: the particle
1133 type and initial momentum is known from beamline information. The precise calori-
1134 metric energy reconstruction of the LArTPC technology enables the measurement of
1135 the total differential cross section for tagged hadrons. The Pion-Nucleus and Kaon-
1136 Nucleus total hadronic interaction cross section have never been measured before in
1137 argon and they are a fundamental step to shed light on light meson interaction in nu-
1138 clei per se, while providing a key input to neutrino physics and proton decay studies
1139 in future LArTPC experiments like SBN and DUNE.

1140 In order to showcase LArIAT’s utility to SBN and DUNE, we illustrate briefly
1141 two comparisons as examples: one regarding neutrino interactions and the second
1142 regarding proton decay studies.

1143 The left side of figure 2.8 shows the distribution of products in momentum spectrum
1144 and particle type as simulated in a ν_e CC interaction in DUNE (according to [86]);
1145 the range of these distribution is to compare with the momentum distribution of
1146 light particles in the LArIAT beamline – shown on the right side of figure 2.8. The
1147 momentum spectrum in the LArIAT beamline for electrons, muons and pions – the
1148 most abundant particles produced in a ν_e CC interaction – covers a wide range of the
1149 expected momentum distribution in a neutrino event.

1150 The signature of a proton decay event in the “LAr golden mode” is the presence of
 1151 a single kaon of about 400 MeV in the detector; the momentum spectrum of the kaon
 1152 pre and post FSI in such an event as simulated by GENIE is shown on the left side
 1153 of figure 2.9. The right side of figure 2.9 shows the momentum spectrum of kaons in
 1154 the LArIAT beamline. Kaons arriving to the LArIAT TPC are ideal for proton decay
 1155 studies, since their momentum in the beamline is just above the typical momentum
 1156 for kaons in a proton decay event: the majority of LArIAT kaons slow down in the
 1157 TPC enough to enter the desired momentum window.

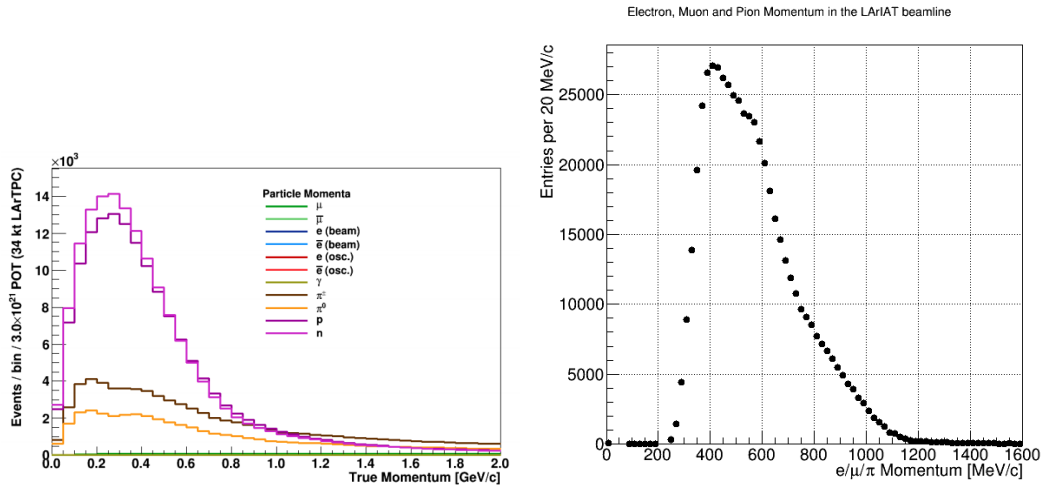


Figure 2.8: *Left.* Simulation of the products of a ν_e CC interaction in DUNE, both in particles type and momentum.

Right. Momentum spectrum for low mass particles (e, μ, π) in the LArIAT beamline, negative tune, Run II, Picky Tracks see section 3.2.2.

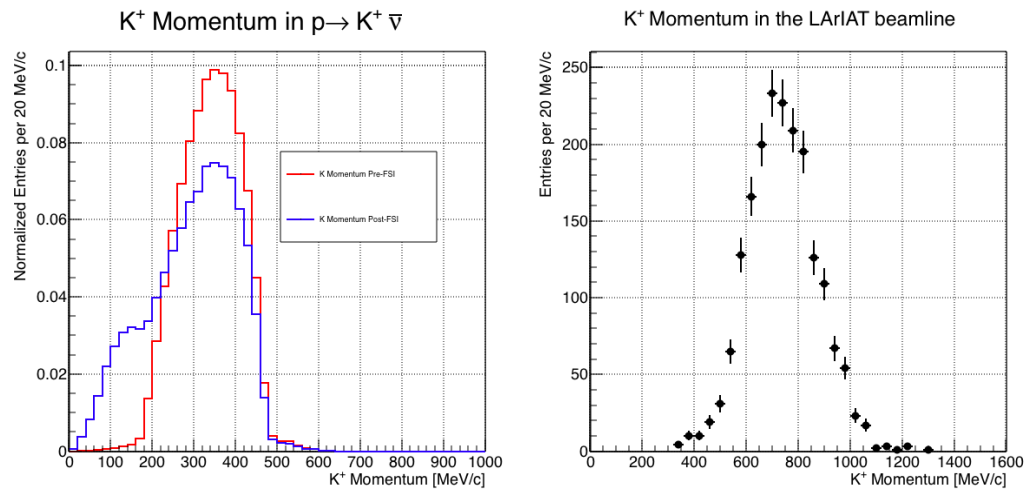


Figure 2.9: *Left.* Momentum of the kaon outgoing a proton decay $p \rightarrow K^+ \bar{\nu}$ event as simulated by the Genie 2.8.10 event generator in argon. The red line represents the kaon momentum distribution before undergoing the simulated final state interaction inside the argon nucleus, while the blue line represents the momentum distribution after FSI.

Right. Positive Kaon momentum spectrum in the LArIAT beamline, positive tune, Run II, Picky Tracks see section 3.2.2.

1158 **Chapter 3**

1159 **LArIAT: Liquid Argon In A**

1160 **Testbeam**

1161 “*But, hey we need to be somewhat foolish...*”

1162 – Agnes Obel, Avenue, 2010 –

1163 In this chapter, we describe the LArIAT experimental setup. We start by illus-
1164 trating the journey of the charged particles in the Fermilab accelerator complex, from
1165 the gaseous thermal hydrogen at the Fermilab ion source to the delivery of the LAr-
1166 IAT tertiary beam at MC7. We then describe the LArIAT beamline detectors, the
1167 LArTPC, the DAQ and the monitoring system.

1168 **3.1 The Particles’ Path to LArIAT**

1169 LArIAT’s particle history begins in the Fermilab accelerator complex with a beam of
1170 protons. The process of proton acceleration develops in gradual stages (see picture
1171 3.1): gaseous hydrogen is ionized in order to form H^- ions; these ions are boosted
1172 to 750 keV by a Cockcroft-Walton accelerator and injected into the linear accelerator
1173 (Linac) that increases their energy up to 400 MeV; then, H^- ions pass through a

1174 carbon foil and lose the two electrons; the resulting protons are then injected into a
1175 rapid cycling synchrotron, called the Booster; at this stage, protons reach 8 GeV of
1176 energy and are compacted into bunches; the next stage of acceleration is the Main
1177 Injector, a synchrotron which accelerates the bunches up to 120 GeV; in the Main
1178 Injector, several bunches are merged into one and are ready for delivery.

1179 The Fermilab accelerator complex works in supercycles of 60 seconds in duration.
1180 A 120 GeV primary proton beam with variable intensity is extracted in four-second
1181 “spills” and sent to the Meson Center beam line.

1182 LArIAT’s home at Fermilab is the Fermilab Test Beam Facility (FTBF), where
1183 the experiment characterizes a beam of charged particles in the Meson Center beam
1184 line. At FTBF, the primary beam is focused onto a tungsten target to create LAr-
1185 IAT’s secondary beam. The secondary beamline is set such that the composition of
1186 the secondary particle beam is mainly positive pions. The momentum peak of the
1187 secondary beam was fixed at 64 GeV/c for the LArIAT data considered in this work,
1188 although the beam is tunable in momentum between 8-80 GeV/c; this configuration
1189 of the secondary beamline assured a stable beam delivery at the LArIAT experimental
1190 hall.

1191 The secondary beam impinges then on a copper target within a steel collimator
1192 inside the LArIAT experimental hall (MC7) to create the LArIAT tertiary beam,
1193 (shown in Fig. 3.2). The steel collimator selects particles produced with a 13° pro-
1194 duction angle. The particles are then bent by roughly 10° through a pair of dipole
1195 magnets. By configuring the field intensity of the magnets we allow the particles of
1196 LArIAT’s tertiary beam to span a momentum range from 0.2 to 1.4 GeV/c. The
1197 polarity of the magnet is also configurable and determines the sign of the beamline
1198 particles which are focused on the LArTPC. If the magnet polarity is positive the
1199 tertiary beam composition is mostly pions and protons with a small fraction of elec-
1200 trons, muons, and kaons. It is the job of the LArIAT beamline equipment to select the

Fermilab Accelerator Complex

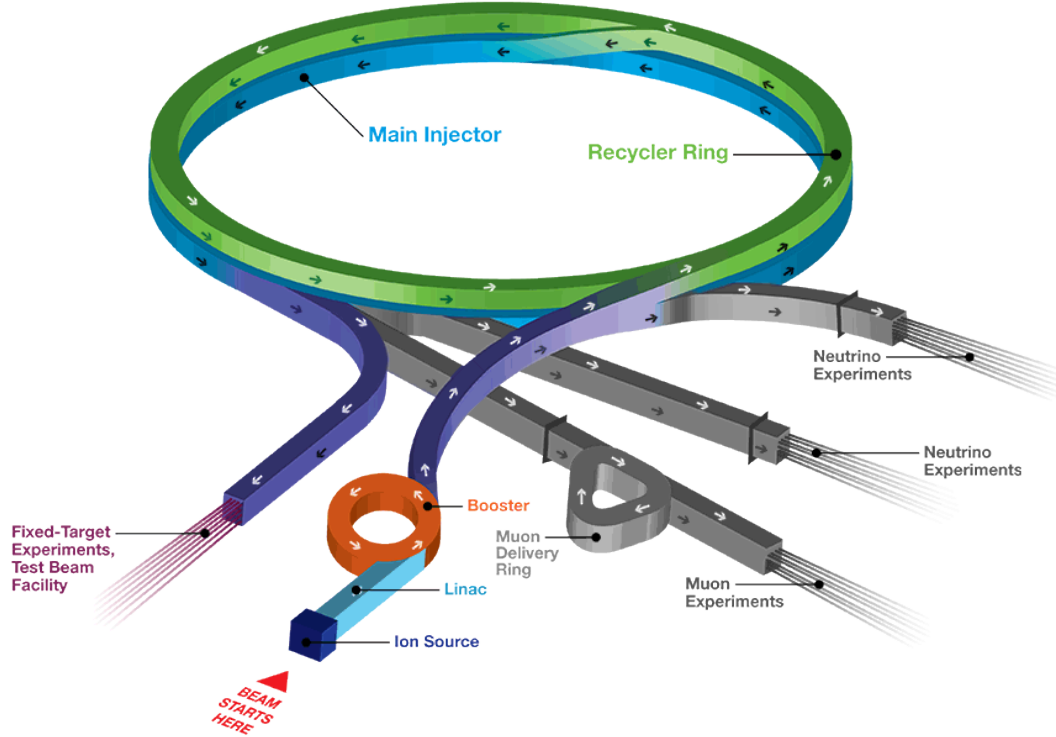


Figure 3.1: Layout of Fermilab Accelerator complex.

1201 particles polarity, to perform particle identification in the beamline and to measure
1202 the momentum of the tertiary beam particles before they get to the LArTPC. The
1203 LArIAT detectors are described in the following paragraphs.

1204 3.2 LArIAT Tertiary Beam Instrumentation

1205 The instrumentation of LArIAT tertiary beam and the TPC components have changed
1206 several times during the three years of LArIAT data taking. The following paragraphs
1207 describe the components operational during “Run II”, the data taking period relevant
1208 to the hadron cross section measurements considered in this thesis.

1209 The key components of the tertiary beamline instrumentation for the hadron cross
1210 section analyses are the two bending magnets, a set of four wire chambers (WCs)

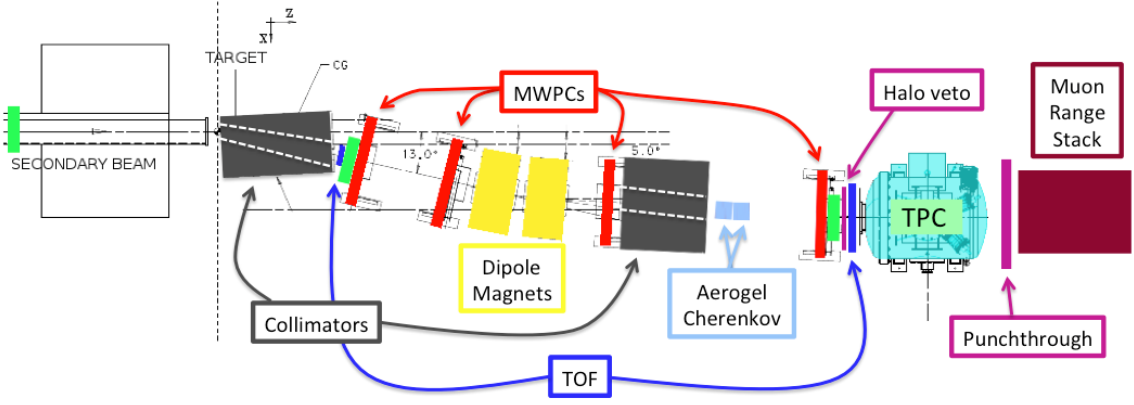


Figure 3.2: Bird’s eye view of the LArIAT tertiary beamline. In grey: upstream and downstream collimators; in yellow: bending magnets; in red: multi wire proportional chambers; in blue: time of flight; in green: liquid argon TPC volume; in maroon: muon range stack.

and two time-of-flight scintillating paddles (TOF) and, of course, the LArTPC. The magnets determine the polarity of the particles in the tertiary beam; the combination of magnets and wire chambers determines the particles’ momenta, which is used to determine the particle species in conjunction with the TOF. A muon range stack downstream from the TPC and two sets of cosmic paddles configured as a telescope surrounding the TPC are also used for calibration purposes. A couple of Aerogel Cherenkov counters, which we will not describe here as they are not used in the hadron cross section measurements, completes the beamline instrumentation.

3.2.1 Bending Magnets

LArIAT uses a pair of identical Fermilab type “NDB” electromagnets, recycled from the Tevatron’s anti-proton ring, in a similar configuration used for the MINERvA T-977 test beam calibration [55]. The magnets are a fundamental piece of the LArIAT beamline equipment, as they are used for the selection of the particle polarity and for the momentum measurement before the LArTPC. The sign of the current in the magnets allows us to select either positively or negatively charged particles; the value

1226 of the magnetic field is used in the momentum determination and in the subsequent
1227 particle identification.

1228 We describe here the characteristics and response of one magnet, as the second one
1229 has a similar response, given its identical shape and history. Each magnet is a box with
1230 a rectangular aperture gap in the center to allow for the particle passage. The magnet
1231 aperture measures 14.22 cm in height, 31.75 cm in width, and 46.67 cm in length.
1232 Since the wire chambers aperture ($\sim 12.8 \text{ cm}^2$) is smaller than the magnet aperture,
1233 only the central part of the magnet gap is utilized. The field is extremely uniform
1234 over this limited aperture and was measured with two hall probes, both calibrated
1235 with nuclear magnetic resonance probes. The probes measured the excitation curve
1236 shown in Figure 3.3.

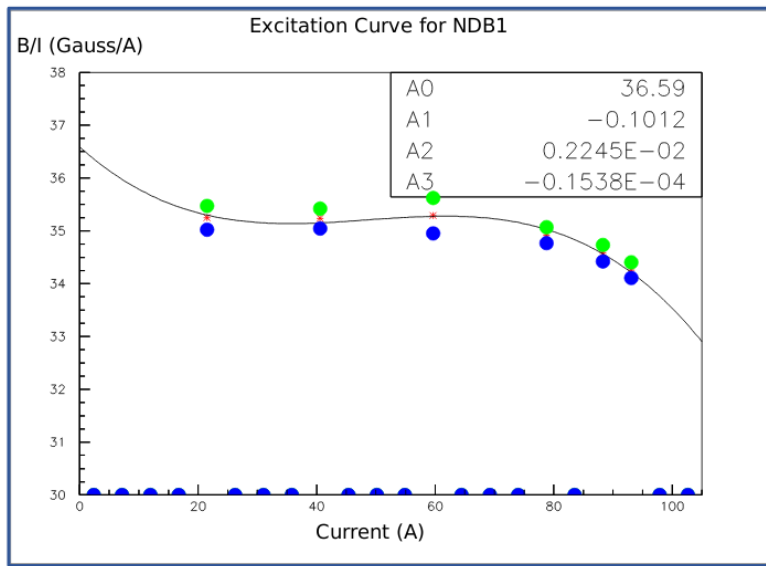


Figure 3.3: Magnetic field over current as a function of the current, for one NDB magnet (excitation curve). The data was collected using two hall probes (blue and green). We fit the readings with a cubic function (black) to average of measurements (red) given in the legend [42].

1237 The current through the magnets at a given time is identical in both magnets.
1238 For the Run II data taking period, the current settings explored were 60A ($B \sim 0.21$
1239 T) and 100A ($B \sim 0.35$ T) in both polarities. Albeit advantageous to enrich the
1240 tertiary beam composition with high mass particles such as kaons, we never pushed

1241 the magnets current over 100 A, not to incur in overheating. During operation, we
1242 operated an air and water cooling system on the magnets and we remotely monitored
1243 the magnet temperatures.

1244 **3.2.2 Multi-Wire Proportional Chambers**

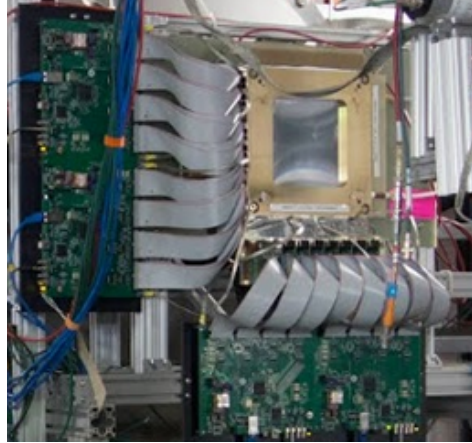


Figure 3.4: One of the four Multi Wire Proportional Chambers (WC) used in the LArIAT tertiary beamline and related read-out electronics.

1245 LArIAT uses four multi-wire proportional chambers, or wire chambers (WC) for
1246 short, two upstream and two downstream from the bending magnets. The geometry of
1247 one chamber is shown in Figure 3.4: the WC effective aperture is a square of 12.8 cm
1248 perpendicular to the beam direction. Inside the chamber, the 128 horizontal and 128
1249 vertical wires strung at a distance of 1 mm from each other in a mixture of 85% Argon
1250 and 15% isobutane gas. The WC operating voltage is between 2400 V and 2500 V.
1251 The LArIAT wire chambers are an upgraded version of the Fenker Chambers [61],
1252 where an extra grounding improves the signal to noise ratio of the electronic readout.

1253 Two ASDQ chips [94] mounted on a mother board plugged into the chamber serve
1254 as front end amplifier/discriminator. The chips are connected to a multi-hit TDC [72]
1255 which provides a fast OR output used as first level trigger. The TDC time resolution
1256 is 1.18 ns/bin and can accept 2 edges per 9 ns. The maximum event rate acceptable
1257 by the chamber system is 1 MHz: this rate is not a limiting factor considering that

1258 the rate of the tertiary particle beam at the first wire chamber is estimated to be less
1259 than 15 kHz. A full spill of data occurring once per supercycle is stored on the TDC
1260 board memory at once and read out by a specially designed controller. We use LVDS
1261 cables to carry both power and data between the controller and the TDCs and from
1262 the controller to the rest of the DAQ.

1263 Multi-Wire Proportional Chambers functionality

1264 We use the wire chamber system together with the bending magnets to measure the
1265 particle's momentum.

1266 In the simplest scenario, only one hit on each and every of the four wire chambers
1267 is recorded during a single readout of the detector systems. Thus, we use the hit
1268 positions in the two wire chambers upstream of the magnets to form a trajectory
1269 before the bend, and the hit positions in the two wire chambers downstream of the
1270 magnets to form a trajectory after the bend. We use the angles in the XZ plane
1271 between the upstream and downstream trajectories to calculate the Z component of
1272 the momentum as follows:

$$P_z = \frac{B_{eff}L_{eff}}{3.3(\sin(\theta_{DS}) - \sin(\theta_{US}))}, \quad (3.1)$$

1273 where B_{eff} is the effective maximum field in a square field approximation, L_{eff}
1274 is the effective length of both magnets (twice the effective length of one magnet),
1275 θ_{US} is the angle off the z axis of the upstream trajectory, θ_{DS} is the angle off the
1276 z axis of the downstream trajectory and $3.3 c^{-1}$ is the conversion factor from [T·m]
1277 to [MeV/c]. By using the hit positions on the third and fourth wire chamber, we
1278 estimate the azimuthal and polar angles of the particle trajectory, and we are able to
1279 calculate the other components of the momentum.

1280 The presence of multiple hits in a single wire chamber or the absence of hits in one
1281 (or more) wire chambers can complicate this simple scenario. The first complication

is due to beam pile up, while the latter is due to wire chamber inefficiency. In the case of multiple hits on a single WC, at most one wire chamber track is reconstructed per event. Since the magnets bend particles only in the X direction, we assume the particle trajectory to be roughly constant in the YZ plane, thus we keep the combination of hits which fit best with a straight line. It is still possible to reconstruct the particle’s momentum even if the information is missing in either of the two middle wire chambers (WC2 or WC3), by constraining the particle trajectory to cross the plane in between the magnets.

Events satisfying the simplest scenario of one single hit in each of the four wire chambers form the “Picky Track” sample. We construct another, higher statistics sample, where we loosen the requirements on single hit and wire chamber efficiency: the “High Yield” sample. For LArIAT Run II, the High Yield sample is about three times the Picky Tracks statistics. We assume an uncertainty of 2% for four-point WC track, momentum uncertainty as reported for the same beamline in [55].

3.2.3 Time-of-Flight System

Two scintillator paddles, one upstream of the first set of WCs and one downstream of the second set of WCs form LArIAT time-of-flight (TOF) detector system.

The upstream paddle is made of a 10 x 6 x 1 cm scintillator piece, read out by two PMTs mounted on the beam left side which collect the light from light guides mounted on all four edges of the scintillator. The downstream paddle is a 14 x 14 x 1 cm scintillator piece read out by two PMTs on the opposite ends of the scintillator, as shown in figure 3.5. The relatively thin width in the beamline direction minimizes energy loss of beam particles traveling through the scintillator material.

The CAEN 1751 digitizer is used to digitize the TOF PMTs signals at a sampling rate of 1 GHz. The 12 bit samples are stored in a circular memory buffer. At trigger time, data from the TOF PMTs are recorded to output in a 28.7 μ s windows starting

1308 approximately 8.4 μ s before the trigger time.

1309 **TOF functionality**

1310 The TOF signals rise time (10-90%) is 4 ns and a full width, half-maximum of 9 ns
1311 consistent in time. The signal amplitudes from the upstream TOF and downstream
1312 TOF are slightly different: 200 mV for the upstream PMTs but only 50 mV for
1313 downstream PMTs. The time of the pulses was calculated utilizing an oversampled
1314 template derived from the data itself. We take the pulse pedestal from samples
1315 far from the pulse and subtract it from the pulse amplitude. We then vertically
1316 stretch a template to match the pedestal-subtracted pulse amplitude and we move
1317 it horizontally to find the time. With this technique, we find a pulse time-pickoff
1318 resolution better than 100 ps. The pulse pile up is not a significant problem given
1319 the TOF timing resolution and the rate of the particle beam. Leveraging on the
1320 pulses width uniformity of any given PMT, we flag events where two pulses overlap
1321 as closely in time as 4 ns with a 90% efficiency according to simulation.

1322 We combine the pulses from the two PMTs on each paddle to determine the
1323 particles' arrival time by averaging the time measured from the single PMT, so to
1324 minimize errors due to optical path differences in the scintillator. However, a time
1325 spread of approximately 300 ps is present in both the upstream and downstream
1326 detectors, likely due to transit time jitter in the PMTs themselves.

1327 **3.2.4 Punch-Through and Muon Range Stack Instruments**

1328 The punch-through and the muon range stack (MuRS) detectors are located down-
1329 stream of the TPC. These detectors provide a sample of TPC crossing tracks without
1330 relying on TPC information and can be used to improve particle ID for muons and
1331 pions with momentum higher than 450 MeV/c.

1332 The punch-through is simple sheet of scintillator material, read out by two PMTs.



Figure 3.5: Image of the down stream time of flight paddle, PMTs and relative support structure before mounting.

1333 The MuRS is a segmented block of steel with four slots instrumented with scintillation
1334 bars. The four steel layers in front of each instrumented slot are 2 cm, 2 cm, 14 cm
1335 and 16 cm deep in the beam direction. Each instrumented slot is equipped with
1336 four scintillation bars each, positioned horizontally in the direction orthogonal to the
1337 beam. Each scintillator bar measures $\textcolor{red}{? \times ? \times 2}$ cm and it is read out by one PMT.

1338 The signals from both the punch-thorough and the MuRS PMTs are sent to a
1339 NIM discriminator. If the signal crosses the discriminator threshold, it is digitized in
1340 the CAEN V1740, same as the TPC. The sampling time of the CAEN V1740 is slow
1341 (of the order of 128 ns) and that the pulse shape information from the PMT is lost.
1342 A Punch-thorough and MuRS signal will then be simply a “hit” at a given time in
1343 the beamline event.

1344 It is worth mentioning here the presence of an additional scintillation paddle
1345 between WC4 and the downstream paddle of the TOF system, called halo. The
1346 halo is a $39 \times 38 \times 1$ cm 3 paddle with a 6.5 cm radius hole in the center, whose original
1347 function was to reject beam particles slightly offset from the beamline center. Data

1348 from this paddle turned out to be unusable, so our data events include both particle
1349 going through the halo scintillation material or through the halo hole.

1350 **3.2.5 LArIAT Cosmic Ray Paddle Detectors**

1351 LArIAT triggers both on beam events and on cosmic rays events. We perform this
1352 latter trigger by using two sets of cosmic ray paddle detectors (a.k.a. “cosmic towers”.)
1353 The cosmic towers frame the LArIAT cryostat, as one sits in the downstream left
1354 corner and the other sits in the upstream right corner of the cryostat. Two paddle
1355 sets of four scintillators pieces each make up each cosmic tower, an upper set and a
1356 lower set per tower. Of the four paddles, a couple of two matched paddles stands
1357 upright while the a second matched pair lies across the top of the assembly in the top
1358 sets (or across the bottom of the assembly in the bottom sets). The horizontal couple
1359 is used as a veto for particles traveling from inside the TPC out. The four signals
1360 from the vertical paddles along one of the body diagonals of the TPC are combined
1361 in a logical “AND”. This allows to select track due to cosmic muons at the ground
1362 level crossing the TPC along one of its diagonals. Cosmic ray muons whose average
1363 energy is in the few GeV range crossing both anode and cathode populate the events
1364 triggered this way. This particularly useful sample of tracks is associated can be used
1365 for many tasks; for example, we use anode-cathode piercing tracks to cross check the
1366 TPC electric field on data (see Appendix ??), to calibrate the charge response of
1367 the TPC wires for the full TPC volume and to measure the electron lifetime in the
1368 chamber [103].

1369 We retrieved the scintillation paddles from the decommissioning of the CDF de-
1370 tector at Fermilab and we used only the paddles with a counting efficiency greater
1371 than 95% and low noise at working voltage. The measured trigger rate of the whole
1372 system is 0.032 Hz, corresponding to ~ 2 muons per minute.



Figure 3.6: Photograph of one of the scintillation counters used in the cosmic towers.

¹³⁷³ 3.3 In the Cryostat

¹³⁷⁴ The heart of the LArIAT experiment lives in the LArIAT Cryostat. In this section,
¹³⁷⁵ we describe the cryogenic system and the argon purity (Section 3.3.1), the LArIAT
¹³⁷⁶ TPC (Section 3.3.2) and light collection system (3.3.3).

¹³⁷⁷ 3.3.1 Cryogenics and Argon Purity

¹³⁷⁸ LArIAT repurposed the ArgoNeuT cryostat [17] in order to use it in a beam of charged
¹³⁷⁹ particles, and added a new process piping and a new liquid argon filtration system in
¹³⁸⁰ FTBF. Inside the LArIAT experimental hall, the cryostat sits in the beam of charged
¹³⁸¹ particles with its horizontal main axis oriented parallel to the secondary beam, 3°
¹³⁸² off axis from the tertiary beam

¹³⁸³ Two volumes make up LArIAT cryostat, shown in Figure 3.7: the inner vessel and
¹³⁸⁴ the outer vessel. Purified liquid argon fills the inner vessel, while the outer volume
¹³⁸⁵ provides insulation through a vacuum jacket equipped with layers of aluminized mylar
¹³⁸⁶ superinsulation. The inner vessel is a cylinder of 130 cm length and 76.2 cm diameter,
¹³⁸⁷ containing about 550 L of LAr, corresponding to a mass of 0.77 ton. We run the signal
¹³⁸⁸ cables for the LArTPC and the high voltage feedthrough through a “chimney” at the
¹³⁸⁹ top and mid-length of the cryostat.

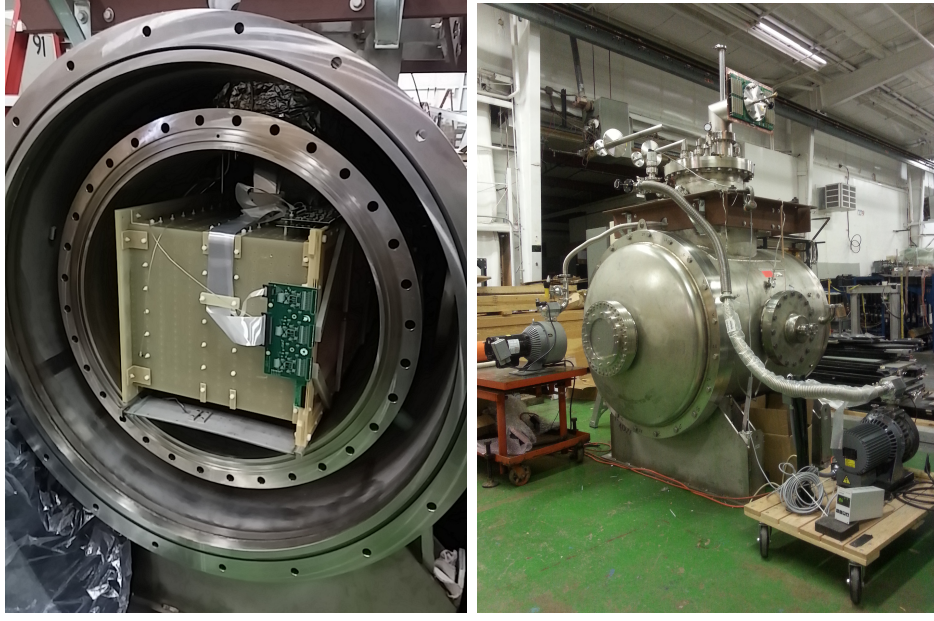


Figure 3.7: Left: the LArIAT TPC in the inner volume of the open cryostat. Right: cryostat fully sealed ready to be transported to FTBF.

Given the different scopes of the ArgoNeuT and LArIAT detectors, we made several modifications to the ArgoNeuT cryostat in order to use it in LArIAT. In particular, the modifications shown in Figure 3.8 were necessary to account for the beam of charged particles entering the TPC and to employ the new FTBF liquid argon purification system. We added a “beam window” on the front outer end cap and an “excluder” on the inner endcap, with the purpose of minimizing the amount of non-instrumented material upstream of the TPC’s active volume. The amount of non-instrumented material in front of the TPC for LArIAT corresponds to ~ 0.3 electron radiation lengths (X_0), to compare against the $\sim 1.6X_0$ of ArgoNeuT. To allow studies of the scintillation light, we added a side port feedthrough which enables the mounting of the light collection system, as well as the connections for the corresponding signal and high-voltage cables (see Section 3.3.3). We modified the bottom of the cryostat adding Conflat and ISO flange sealing to connect the liquid argon transfer line to the new argon cooling and purification system.

As in any other LArTPC, argon purity is a crucial parameter for LArIAT. Indeed,



Figure 3.8: Main modifications to the ArgoNeuT cryostat: 1) outlet for connection to the purification system at the bottom of the cryostat; 2) the “beam-window” on the outer endcap and “excluder” which reduces the amount of non-instrumented material before the TPC; 3) the side port to host the light collection system.

1405 the presence of contaminants affects both the basic working principles of a LArTPC,
 1406 as shown in section 2.1.2: electronegative contaminants such as oxygen and water de-
 1407 crease the number of ionization electrons collected on the wires after drifting through
 1408 the volume. In addition, contaminants such as Nitrogen decrease the light yield
 1409 from scintillation light, especially in its slow component. In LArIAT, contaminations
 1410 should not exceed the level of 0.2 parts per billion (ppb). We achieve this level of
 1411 purity in several stages. The specifics required for the commercial argon bought for
 1412 LArIAT are 2 parts per million (ppm) oxygen, 3.5 ppm water, and 10 ppm nitrogen.
 1413 This argon is monitored with the use of commercial gas analyzer. Argon is stored in
 1414 a dewar external to LArIAT hall and filtered before filling the TPC. LArIAT uses a
 1415 filtration system designed for the Liquid Argon Purity Demonstrator (LAPD) [56]:
 1416 half of a 77 liter filter contains a 4A molecular sieve (Sigma-Aldrich [109]) able to re-
 1417 move mainly water, while the other half contains BASF CU-0226 S, a highly dispersed
 1418 copper oxide impregnated on a high surface area alumina, apt to remove mainly oxy-

1419 gen [27]. A single pass of argon in the filter is sufficient to achieve the necessary
1420 purity, unless the filter is saturated. In case the filter saturates, the media needs to
1421 be regenerated by using heated gas; this happened twice during the Run II period¹.
1422 The electron lifetime during the full LArIAT data taking are shown in Figure 2.4.
1423 The filtered argon reaches the inner vessel via a liquid feedthrough which is routed to
1424 the bottom of the cryostat. Argon is not recirculated in the system; rather, it boils
1425 off and vents to the atmosphere. During data taking, we replenish the argon in the
1426 cryostat every 6 hours to keep the TPC high voltage feedthrough and cold electronics
1427 always submerged. In fact, we constantly monitor the level, temperature, and pres-
1428 sure of the argon both in the commercial dewar and inside the cryostat during data
1429 taking.

1430 **3.3.2 LArTPC: Charge Collection**

1431 The LArIAT Liquid Argon Time Projection Chamber is a rectangular box of dimen-
1432 sions 47 cm (drift) x 40 cm (height) x 90 cm (length), containing 170 liters of Liquid
1433 Argon. The LArTPC three major subcomponents are

- 1434 1) the cathode and field cage,
- 1435 2) the wire planes,
- 1436 3) the read-out electronics.

1437 **Cathode and field cage**

1438 A G10 plain sheet with copper metallization on one of the 40 x 90 cm inner surfaces
1439 forms the cathode. A high-voltage feedthrough on the top of the LArIAT cryostat
1440 delivers the high voltage to the cathode; the purpose of the high voltage system

1. We deemed the filter regeneration necessary every time the electron lifetime dropped under 100 μs .

1441 (Figure 3.9) is to drift ionization electrons from the interaction of charged particles
 1442 in the liquid argon to the wire planes. The power supply used in this system is a
 1443 Glassman LX125N16 [69] capable of generating up to -125 kV and 16 mA of current,
 1444 but operated at -23.5kV during LArIAT Run-II. The power supply is connected via
 1445 high voltage cables to a series of filter pots before finally reaching the cathode.

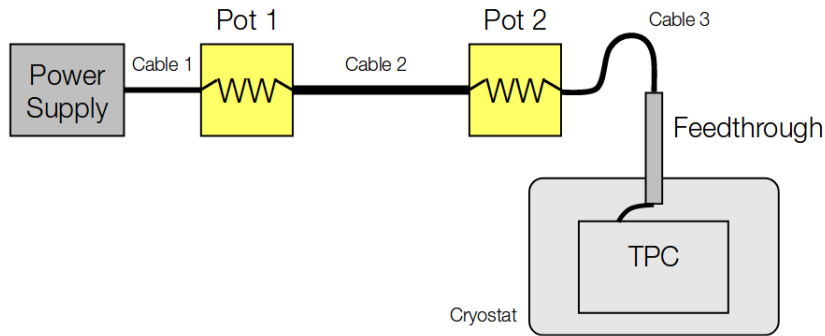


Figure 3.9: Schematic of the LArIAT high voltage system.

1446 The field cage is made of twenty-three parallel copper rings framing the inner
 1447 walls of the G10 TPC structure. A network of voltage-dividing resistors connected to
 1448 the field cage rings steps down the high voltage from the cathode to form a uniform
 1449 electric field. The electric field over the entire TPC drift volume is 486 V/cm, as
 1450 measured in appendix ???. The maximum drift length, i.e. the distance between
 1451 cathode and anode planes, is 47 cm.

1452 Wire planes

1453 LArIAT Run-II has three wire planes separated by 4 mm spaces: in order of increasing
 1454 distance from the cathode, they are the shield, the induction and the collection plane.
 1455 The “wire pitch”, i.e., the distance between two adjacent wires in a given plane, is
 1456 4 mm. The shield plane counts 225 parallel wires of equal length oriented vertically.
 1457 This plane is not connected with the read-out electronics; rather it shields the outer
 1458 planes from extremely long induction signals due to the ionization in the whole drift

volume. As the shield plane acts almost like a Faraday cage, the resulting shape of signals in the first instrumented plane (induction) is easier to reconstruct. Both the induction and collection planes count 240 parallel wires of different length oriented at 60° from the vertical with opposite signs. Electrons moving past the induction plane will induce a bipolar pulse on its wires; the drifting electrons will be then collected on the collection plane's wires, forming a unipolar pulse.

The three wire planes and the cathode form three drift volumes, as shown in Figure 3.10. The main drift volume is defined as the region between the cathode plane and the shield plane (C-S). The other two drift regions are those between the shield plane and the induction plane (S-I), and between the induction plane and the collection plane (I-C). The electric field in these regions is chosen to satisfy the charge transparency condition and allow for 100% transmission of the drifting electrons through the shield and the induction planes.

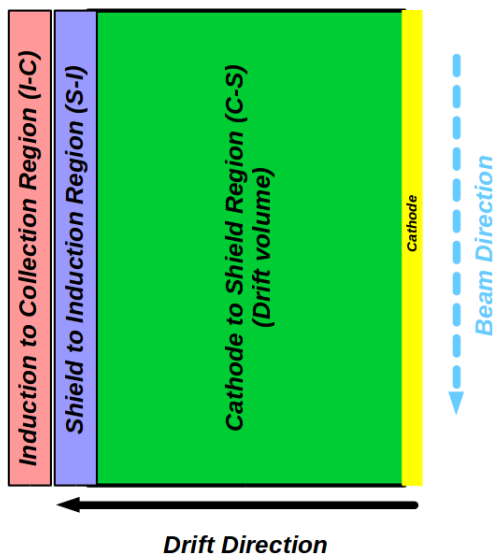


Figure 3.10: Schematic of the three drift regions inside the LArIAT TPC: the main drift volume between the cathode and the shield plane (C-S) in green, the region between the shield plane and the induction plane (S-I) in purple, and the region between the induction plane and the collection plane (I-C) in pink.

Table 3.1 provides the default voltages applied to the cathode and the shield,

1473 induction, and collection plane.

Table 3.1: Cathode and anode planes default voltages

Cathode	Shield	Induction	Collection
-23.17 kV	-298.8 V	-18.5 V	338.5 V

1474 Electronics

1475 Dedicated electronics read the induction and collection plane wires, for a total of
1476 480-channel analog signal path from the TPC wires to the signal digitizers. A digital
1477 control system for the TPC-mounted electronics, a power supply, and a distribution
1478 system complete the front-end system. Figure 3.11 shows a block diagram of the
1479 overall system. The direct readout of the ionization electrons in liquid argon forms
1480 typically small signals on the wires, which need amplification in oder to be processed.
1481 LArIAT performs the amplification stage directly in cold with amplifiers mounted
1482 on the TPC frame inside the liquid argon. The BNL ASICs adopted in LArIAT are
1483 designated as LArASIC, version 4-star and are the same used by the MicroBooNE
1484 experiment [59]. The signal from the ASICs are driven to the other end of the readout
1485 chain, to the CAEN V1740 digitizers [35]. The CAEN V1740 has a 12 bit resolution
1486 and a maximum input range of 2 VDC, resulting in about 180 ADC count for a
1487 crossing MIP.

1488 3.3.3 LArTPC: Light Collection System

1489 The collection of scintillation photons is the second mechanism of particle detection
1490 in argon other than the ionization electrons. Over the course of LArIAT's three years
1491 of data taking, the light collection system changed several times. We describe here
1492 the light collection system for Run II. Two PMTs, a 3-inch diameter Hamamatsu
1493 R-11065 and 2-inch diameter ETL D757KFL [7], as well as three SiPMs arrays (two
1494 Hamamatsu S11828-3344M 4x4 arrays and one single-channel SensL MicroFB-60035)

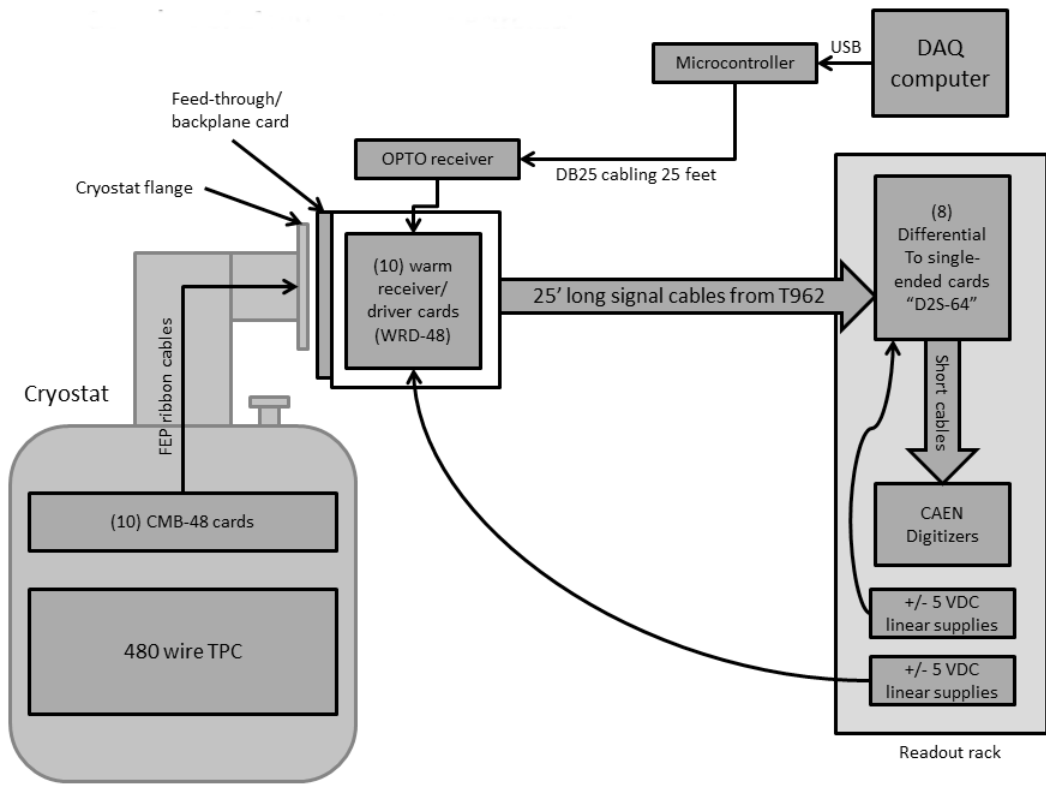


Figure 3.11: Overview of LArIAT Front End electronics.

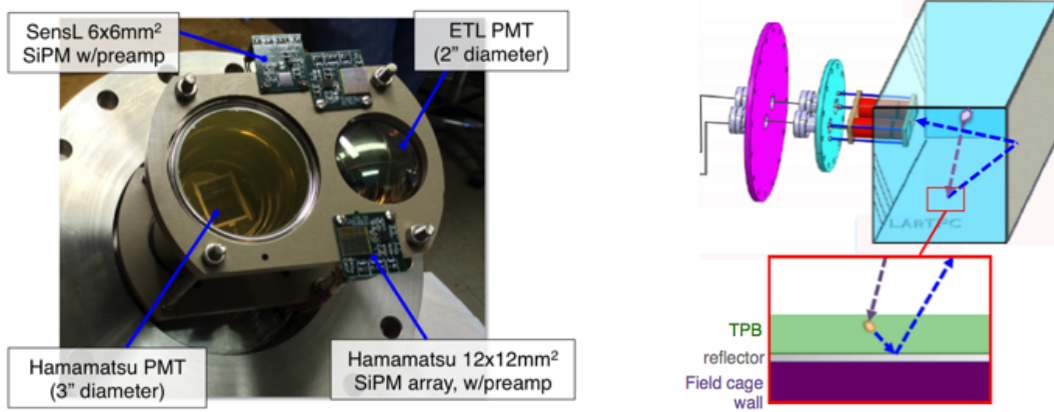


Figure 3.12: LArIAT’s photodetector system for observing LAr scintillation light inside the TPC (left), and a simplified schematic of VUV light being wavelength-shifting along the TPB-coated reflecting foils (right).

1495 are mounted on the PEEK support structure. PEEK screws into an access flange
 1496 as shown in Figure 3.12, on the anode side, leaving approximately 5 cm of clearance
 1497 from the collection plane.

1498 Liquid argon scintillates in vacuum-ultraviolet (VUV) range at 128 nm; since
 1499 cryogenic PMTs are not sensitive to VUV wavelengths, we need to shift the light to a
 1500 range that is visible to the PMTs. In LArIAT, the wavelength shifting is achieved by
 1501 installing highly-reflective 3M VIKUITI dielectric substrate foils coated with a thin
 1502 layer of tetraphenyl-butadiene (TPB) on the four unbiased walls of the TPC. The
 1503 scintillation light interaction with the TPB emits one or more visible photons, which
 1504 are then reflected into the chamber. Thus, the light yield increases and results in
 1505 higher uniformity of light across the TPC active volume, allowing the possibility of
 1506 light-based calorimetry, currently under study.

1507 For Run II, we coated the windows of the ETL PMT and the SensL SiPM with
 1508 a thin layer of TPB. In doing so, some of the VUV scintillation light converts into
 1509 visible right at the sensor faces, keeping information on the direction of the light
 1510 source. Information about the light directionality is hindered for the light reflected
 1511 on foils, as the reflection is uniform in angle.

1512 3.4 Trigger and DAQ

1513 The LArIAT DAQ and trigger system governs the read out of all the many subsystems
1514 forming LArIAT. The CAEN V1495 module [34] and its user-programmable FPGA
1515 are the core of this system. Every 10 ns, this module checks for matches between
1516 sixteen logical inputs and user-defined patterns in the trigger menu; if it finds a match
1517 for two consecutive clock ticks, that trigger fires.

1518 LArIAT receives three logic signals from the Fermilab accelerator complex related
1519 to the beam timing which we use as input triggers: a pulse just before the beam, a
1520 pulse indicating beam-on, and a beam-off pulse.

1521 The beam instruments, the cosmic ray taggers, and the light collection system
1522 provide the other NIM-standard logic pulse inputs to the trigger decision. We auto-
1523 matically log the trigger inputs configuration with the rest of the DAQ configuration
1524 at the beginning of each run.

1525 Fundamental inputs to the trigger card come from the TOF (see section 3.2.3)
1526 and the wire chambers (see section 3.2.2), as activity in these systems points to the
1527 presence of a charged particle in tertiary beam line. In particular, the discriminated
1528 pulses from the TOF PMTs form a NIM logic pulse for the trigger logic. We ask
1529 for a coincidence within a 20 ns window for all the pulses from the PMTs looking at
1530 the same scintillator block and use a delayed coincidence between the upstream and
1531 downstream paddle to inform the trigger decision. In order to form a coincidence
1532 between the upstream and downstream paddles, we delay the upstream paddle coin-
1533 cidence by 20 ns and widen it by 100 ns. The delay and widening are necessary to
1534 account for both lightspeed particles and slower particles (high-mass) to travel the
1535 6.5 m between the upstream and the downstream paddles. For the read out of the
1536 wire chambers, we use a total of sixteen multi-hit TDCs [72], four per chamber: two
1537 TDC per plane (horizontal and vertical), sixty-four wires per TDC. In each TDC, we
1538 keep the logical “OR” for any signal over threshold from the sixty-four wires. We

1539 then require a coincidence between the “OR” for the horizontal TDCs and the “OR”
1540 for the vertical TDCs: with this logic we make sure that at least one horizontal wire
1541 and one vertical wire saw significant signal in one wire chamber. The single logical
1542 pulse from each of the four wire chambers feeds into the first four inputs to the V1495
1543 trigger card. We require a coincidence within 20 ns of at least three logical inputs to
1544 form a trigger.

1545 The cosmic towers (see Section 3.2.5) provide another primary input to the trigger,
1546 in order to capture long tracks from cosmic muons crossing the TPC. We use NIM
1547 modules to require coincidences between one upper and one lower paddle set of any
1548 opposite cosmic towers. The OR all the opposite towers’ coincidences is fed as an
1549 input to the trigger card.

1550 We use the signal from the cryogenic PMTs (see Section 3.3.3) to form several
1551 interesting triggers. The coincidence of signals from all the PMT pulses within \sim 20 ns
1552 is an indication of ionizing radiation in the TPC and forms a trigger input. The
1553 coincidence of two subsequent scintillation logic pulses delayed by a maximum of $7 \mu\text{s}$
1554 forms the Michel electron trigger.

1555 3.5 Control Systems

1556 LArIAT is a complex ensemble of systems which needed to be monitored simultane-
1557 ously during data taking. We performed the monitoring of the systems operations
1558 with a slow control system, a DAQ monitoring system and a low level data quality
1559 monitoring described in the following sections.

1560 Slow Control

1561 We used the Synoptic Java Web Start framework [19] as a real-time display of subsys-
1562 tem conditions. Synoptic provides a Graphical User Interface that talks to the Fer-

milab Accelerator Control System via the ACNET protocol. Its simple GUI allowed us to change the operating parameters and to graph the trends of several variables of interest for all of the tertiary beam detectors. Among the most important quantities monitored by Synoptic there are the level of argon in both the inner vessel and the external dewar, the operating voltages of cathode and wire planes, of the PMTs and SiPMs, and of the four wire chambers, as well as the magnet temperatures. Figure 3.13 shows an example of the monitoring system. LArIAT uses the Accelerator Control NETwork system (ACNET) to monitor the beam conditions of the MCcenter beamline. For example, the horizontal and vertical position of the beam at the first two wire chambers (WC1 and WC2) are shown in 3.14 as seen by the shifter during data taking.

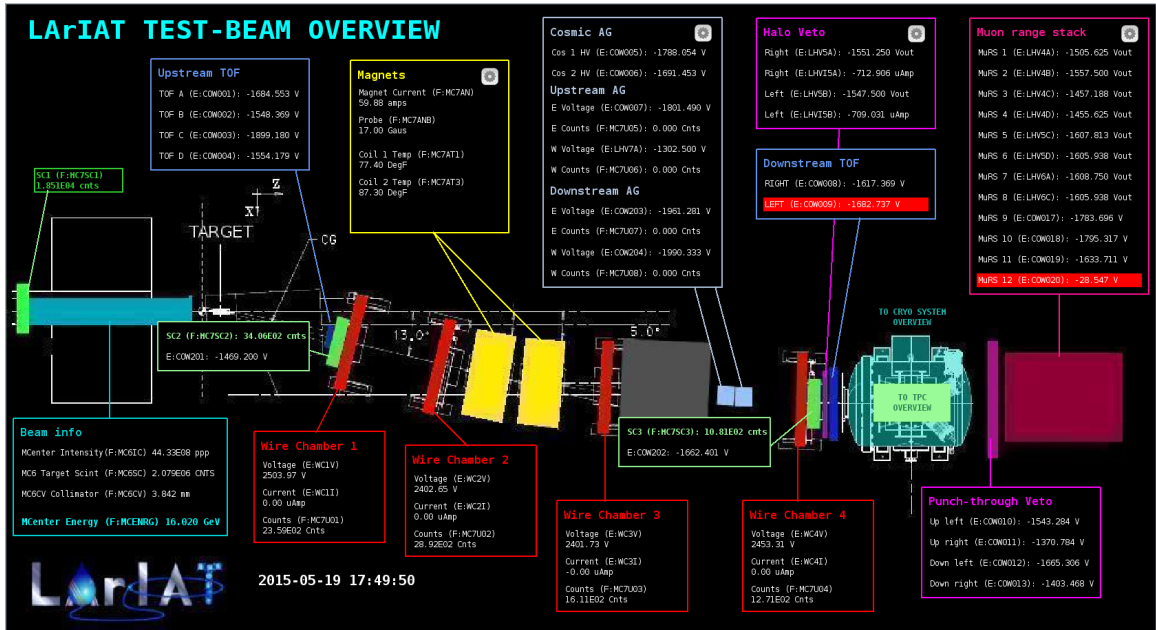


Figure 3.13: Interface of the Synoptic slow control system

1574 DAQ Monitoring

1575 We monitor the data taking and the run time evolution with the Run Status Webpage
 1576 (<http://lariat-wbm.fnal.gov/lariat/run.html>), a webpage updated in real-time. The

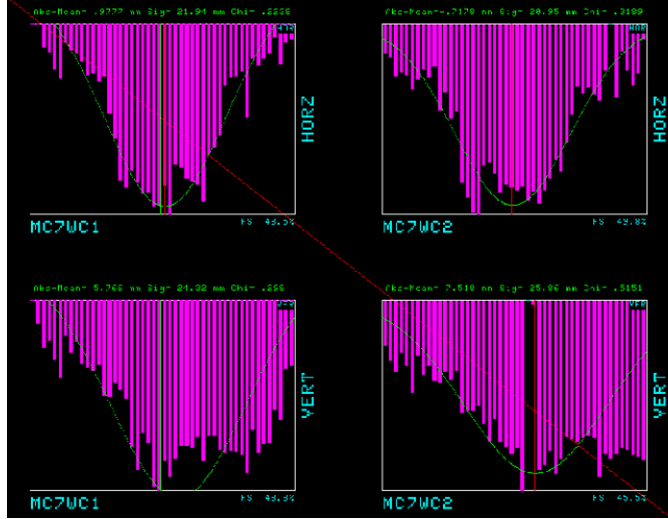


Figure 3.14: Beam position at the upstream wire chambers monitored with ACNET.

1577 page displays, among other information, the total number of triggers in the event,
 1578 the total number of detectors triggered during a beam spill, the trigger patterns, the
 1579 number of times a particular trigger pattern was satisfied during a beam spill, and
 1580 the current time relative to the Fermilab accelerator complex supercycle. A screen
 1581 shot of the page is show in figure 3.15.

1582 Data Quality Monitoring

1583 We employ two systems to ensure the quality of our data during data taking: the
 1584 Near-Real-Time Data Quality Monitoring and the Event Viewer.

1585 The Near-Real-Time Data Quality Monitoring (DQM) is a webpage which receives
 1586 updates from all the VME boards in the trigger system and displays the results of
 1587 a quick analysis of the DAQ stream of raw data on a spill-by-spill basis. The DQM
 1588 allows the shifter to monitor almost in real time (typically with a 2-minute delay)
 1589 a series of low level-quantities and compare them to past collections of beam spills.
 1590 Some of the variables monitored in the DQM are the pedestal mean and RMS on
 1591 CAEN digitizer boards of the TPC wires and PMTs of the beamline detectors, the
 1592 hit occupancy and timing plots on the wire chambers, and number of data fragments

1593 recorded that are used to build a TPC event. Abnormal values for low-level quantity
1594 in the data activates a series of alarms in the DQM; this quick feedback on the DAQ
1595 and beam conditions is fundamental to assure a fast debugging of the detector and a
1596 very efficient data taking during beam uptime.

1597 The online Event Viewer displays a two dimensional representation (Wire vs Time)
1598 of LArIAT TPC events on both the Induction and the Collection planes in near real
1599 time. The raw pulses collected by the DAQ on each wire are plotted as a function
1600 of drift time, resulting in an image of the TPC event easily readable by the shifter.
1601 This tool guarantees a particularly good check of the TPC operation which activate
1602 an immediate feedback for troubleshooting a number of issues. For example, it is
1603 easy for the shifter to spot high occupancy events and request a reduction of the
1604 primary beam intensity, or to spot a decrease of the argon purity which requires the
1605 regeneration of filters, or to catch the presence of electronic noise and reboot the
1606 ASICs. An example of high occupancy event is shown in 3.16.

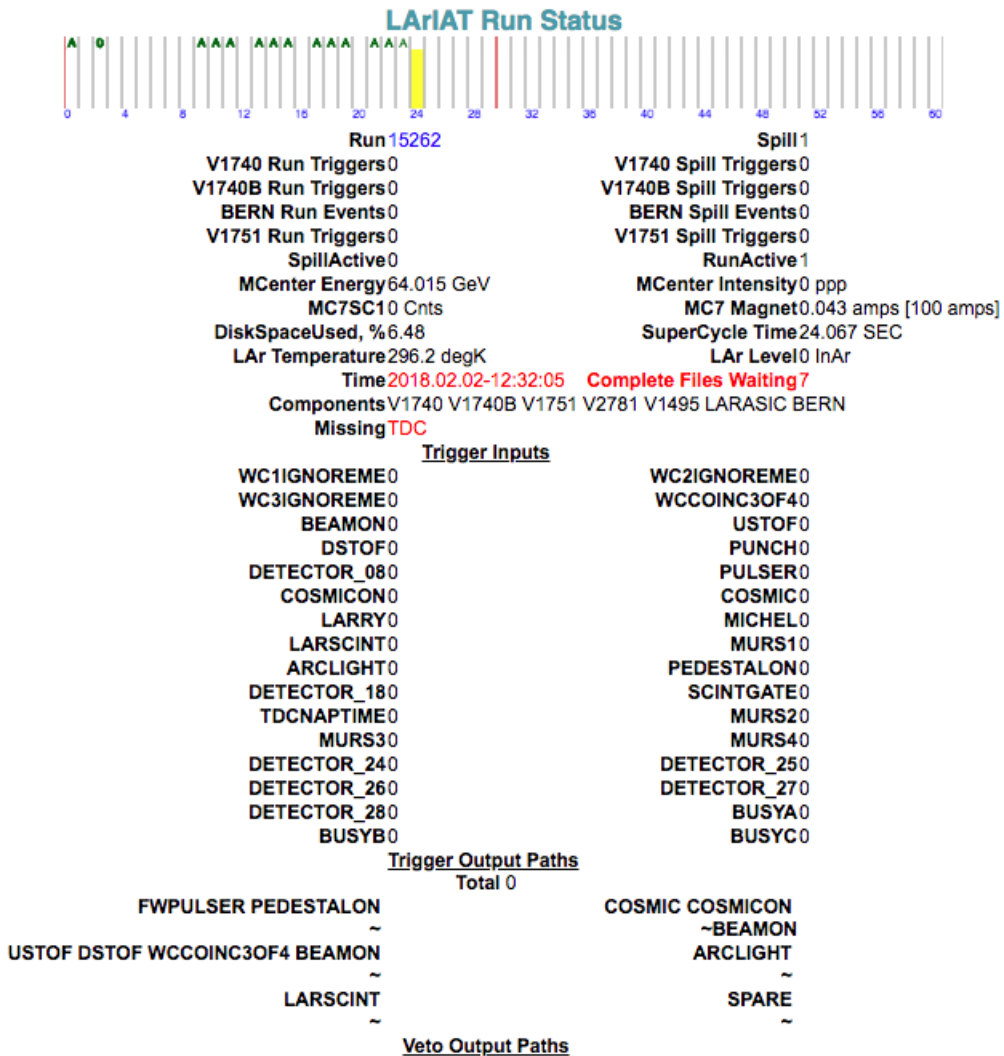


Figure 3.15: Run Status page at LArIAT downtime. At the top the yellow bar displays the current position in the Fermilab supercycle. Interesting information to be monitored by the shifter were the run number and number of spills, time elapsed from data taking (here in red), the energy of the secondary beam and the trigger paths.

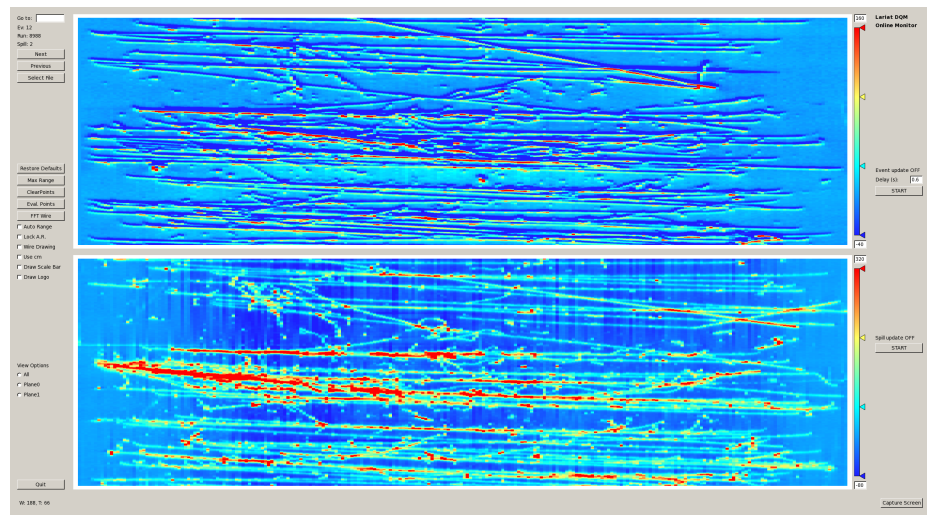


Figure 3.16: High occupancy event display: induction plane (top) and collection plane (bottom).

1607 **Chapter 4**

1608 **Total Hadronic Cross Section**

1609 **Measurement Methodology**

1610 “Like a lemon to the lime and the bubble to the bee”

1611 – Eazy-E, Gimmie that *, 1993 –

1612 This chapter describes the general procedure employed to measure a total hadronic
1613 differential cross section in LArIAT. Albeit with small differences, both the (π^- ,Ar)
1614 and (K^+ ,Ar) total hadronic cross section measurements rely on the same procedure.
1615 We start by selecting the particle of interest using a combination of beamline detectors
1616 and TPC information (Section 4.1). We then perform a handshake between the
1617 beamline information and the TPC tracking to assure the selection of the correct
1618 TPC track (Section 4.2). Finally, we apply the “thin slice” method and measure the
1619 “raw” hadronic cross section (Section 4.3). A series of corrections are then evaluated
1620 to obtain the “true” cross section (Section 4.3.3).

1621 At the end of this chapter, we show a sanity check of the methodology by applying
1622 the thin slice method employing only MC truth information and retrieving the Geant4
1623 tabulated cross section for pions and kaons (Section 4.4).

1624 **4.1 Event Selection**

1625 The measurement of the (π^- ,Ar) and (K^+ ,Ar) total hadronic cross section in LArIAT
1626 starts by selecting the pool of pion or kaon candidates and measuring their momen-
1627 tum. This is done through the series of selections on beamline and TPC information
1628 described in the next sections. The summary of the event selection in data is reported
1629 in Table 4.1.

1630 **4.1.1 Selection of Beamline Events**

1631 As shown in equation 4.5, we leverage the beamline particle identification and mo-
1632 mentum measurement before entering the TPC as an input to evaluate the kinetic
1633 energy for the hadrons used in the cross sections measurements. Thus, we select the
1634 LArIAT data to keep only events whose wire chamber and time of flight information
1635 is registered (line 1 in Table 4.1). Additionally, we perform a check of the plausi-
1636 bility of the trajectory inside the beamline detectors: given the position of the hits
1637 in the four wire chambers, we make sure the particle's trajectory does not cross any
1638 impenetrable material such as the collimator and the magnets steel (line 2 in Table
1639 4.1).

	Run-II Neg Pol	Run-II Pos Pol
1. Events Reconstructed in Beamline	158396	260810
2. Events with Plausible Trajectory	147468	240954
3. Beamline $\pi^-/\mu^-/e^-$ Candidate	138481	N.A.
4. Beamline K^+ Candidate	N.A	2837
5. Events Surviving Pile Up Filter	108929	2389
6. Events with WC2TPC Match	41757	1081
7. Events Surviving Shower Filter	40841	N.A.
8. Available Events For Cross Section	40841	1081

Table 4.1: Number of data events for Run-II Negative and Positive polarity

1640 4.1.2 Particle Identification in the Beamline

1641 In data, the main tool to establish the identity of the hadron of interest is the LArIAT
1642 tertiary beamline, in its function of mass spectrometer. We combine the measurement
1643 of the time of flight, TOF , and the beamline momentum, p_{Beam} , to reconstruct the
1644 invariant mass of the particles in the beamline, m_{Beam} , as follows

$$m_{Beam} = \frac{p_{Beam}}{c} \sqrt{\left(\frac{TOF * c}{l}\right)^2 - 1}, \quad (4.1)$$

1645 where c is the speed of light and l is the length of the particle's trajectory between
1646 the time of flight paddles.

1647 Figure 4.1 shows the mass distribution for the Run II negative polarity runs on
1648 the left and positive polarity runs on the right. We perform the classification of events
1649 into the different samples as follows:

- 1650 • $\pi/\mu/e$: mass $< 350 \text{ MeV}/c^2$
- 1651 • kaon: $350 \text{ MeV} < \text{mass} < 650 \text{ MeV}/c^2$
- 1652 • proton: $650 \text{ MeV} < \text{mass} < 3000 \text{ MeV}/c^2$.

1653 Lines 3 and 4 in Table 4.1 show the number of negative $\pi/\mu/e$ and positive K
1654 candidates which pass the mass selection for LArIAT Run-II data.

1655 4.1.3 TPC Selection: Halo Mitigation

1656 The secondary beam impinging on LArIAT secondary target produces a plethora of
1657 particles which propagates downstream. The presence of upstream and downstream
1658 collimators greatly abates the number of particles tracing down the LArIAT tertiary
1659 beamline. However, it is possible that more than one particle sneaks into the LArTPC
1660 during its readout time: the TPC readout is triggered by the particle firing the

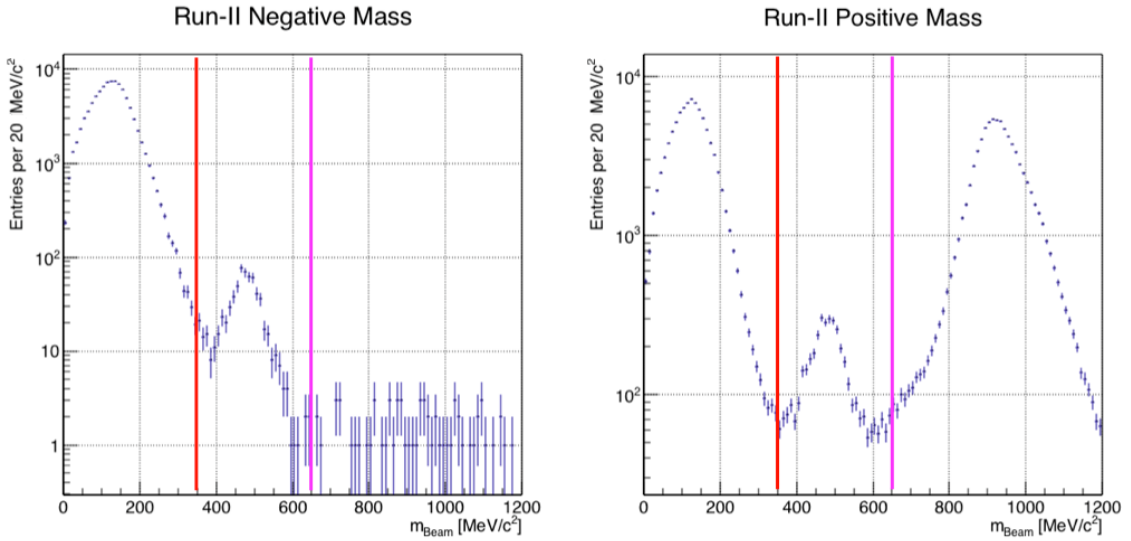


Figure 4.1: Distribution of the beamline mass as calculated according to equation 4.1 for the Run-II events reconstructed in the beamline, negative polarity runs on the left and positive polarity runs on the right. The classification of the events into $\pi^\pm/\mu^\pm/e^\pm$, K^\pm , or (anti)proton is based on these distributions, whose selection cut are represented by the vertical colored lines.

1661 beamline detectors, but particles from the beam halo might be present in the TPC at
 1662 the same time. We call “pile up” the additional traces in the TPC. We adjusted the
 1663 primary beam intensity between LArIAT Run I and Run II to reduce the presence of
 1664 events with high pile up particles in the data sample. For the cross section analyses,
 1665 we remove events with more than 4 tracks in the first 14 cm upstream portion of the
 1666 TPC from the sample (line 5 in in Table 4.1).

1667 4.1.4 TPC Selection: Shower Removal

1668 In the case of the (π^-,Ar) cross section, the resolution of beamline mass spectrometer
 1669 is not sufficient to select a beam of pure pions. In fact, muons and electrons survive
 1670 the selection on the beamline mass. It is important to notice that the composition of
 1671 the negative polarity beam is mostly pions, as will be discussed in section 5.2.1. Still,
 1672 we devise a selection on the TPC information to mitigate the presence of electrons

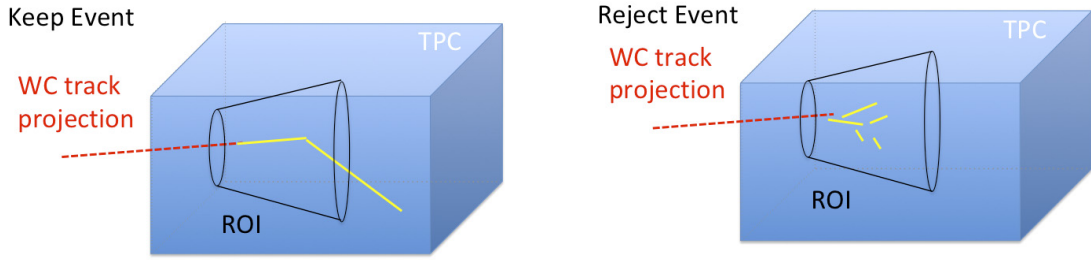


Figure 4.2: Visual rendering of the shower filter. The ROI is a cut cone, with a small radius of 4 cm, a big radius of 10 cm and an height of 42 cm (corresponding to 3 radiation lengths for electrons in Argon).

1673 in the sample used for the pion cross section. The selection relies on the different
 1674 topologies of a pion and an electron event in the argon: while the former will trace
 1675 a track inside the TPC active volume, the latter will tend to “shower”, i.e. interact
 1676 with the medium, producing bremsstrahlung photons which pair convert into several
 1677 short tracks. In order to remove the shower topology, we create a region of interest
 1678 (ROI) around the TPC track corresponding to the beamline particle. We look for
 1679 short tracks contained in the ROI, as depicted in figure 4.4: if more than 5 tracks
 1680 shorter than 10 cm are in the ROI, we reject the event. Line 7 in Table 4.1 shows
 1681 the number of events surviving this selection.

1682 **4.2 Beamline and TPC Handshake: the Wire Cham- 1683 ber to TPC Match**

1684 For each event passing the selection on its beamline information, we need to identify
 1685 the track inside the TPC corresponding to the particle which triggered the beamline
 1686 detectors, a procedure we refer to as “WC to TPC match” (WC2TPC for short).
 1687 In general, the TPC tracking algorithm will reconstruct more than one track in the
 1688 event, partially due to the fact that hadrons interact in the chamber and partially
 1689 because of pile up particles during the triggered TPC readout time, as shown in

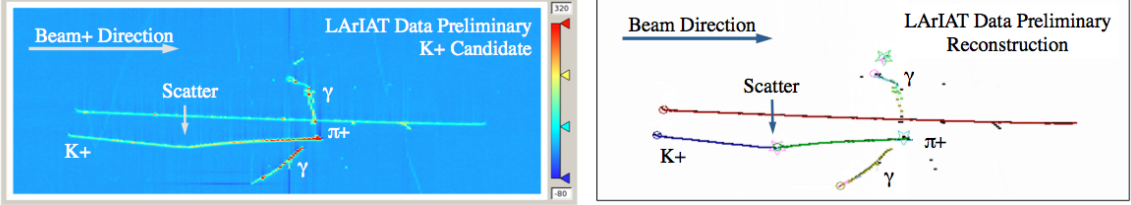


Figure 4.3: Kaon candidate event: on the right, event display showing raw quantities; on the left, event display showing reconstructed tracks. In the reconstructed event display, different colors represent different track objects. A kink is visible in the kaon ionization, signature of a hadronic interaction: the tracking correctly stops at the kink position and two tracks are formed. An additional pile-up track is so present in the event (top track in red).

1690 figure 4.3.

1691 We attempt to uniquely match one wire chamber track to one and only one recon-
 1692 structed TPC track. In order to determine if a match is present, we apply a geomet-
 1693 rical selection on the relative the position of the wire chamber and TPC tracks. We
 1694 start by considering only TPC tracks whose first point is in the first 2 cm upstream
 1695 portion of the TPC for the match. We project the wire chamber track to the TPC
 1696 front face where we define the coordinates of the projected point as x_{FF} and y_{FF} . For
 1697 each considered TPC track, we define ΔX as the difference between the x position of
 1698 the most upstream point of the TPC track and x_{FF} . ΔY is defined analogously. We
 1699 define the radius difference, ΔR , as $\Delta R = \sqrt{\Delta X^2 + \Delta Y^2}$. We define as α the angle
 1700 between the incident WC track and the TPC track in the plane that contains them.
 1701 If $\Delta R < 4$ cm, $\alpha < 8^\circ$, a match between WC-track and TPC track is found. We
 1702 describe how we determine the value for the radius and angular selection in Section
 1703 A.0.1. We discard events with multiple WC2TPC matches. We use only those TPC
 1704 tracks that are matched to WC tracks in the cross section calculation. Line 6 in Table
 1705 4.1 shows the number of events where a unique WC2TPC match was found.
 1706 In MC, we mimic the matching between the WC and the TPC track by construct-
 1707 ing a fake WC track using truth information at wire chamber four. We then apply
 1708 the same WC to TPC matching algorithm as in data.

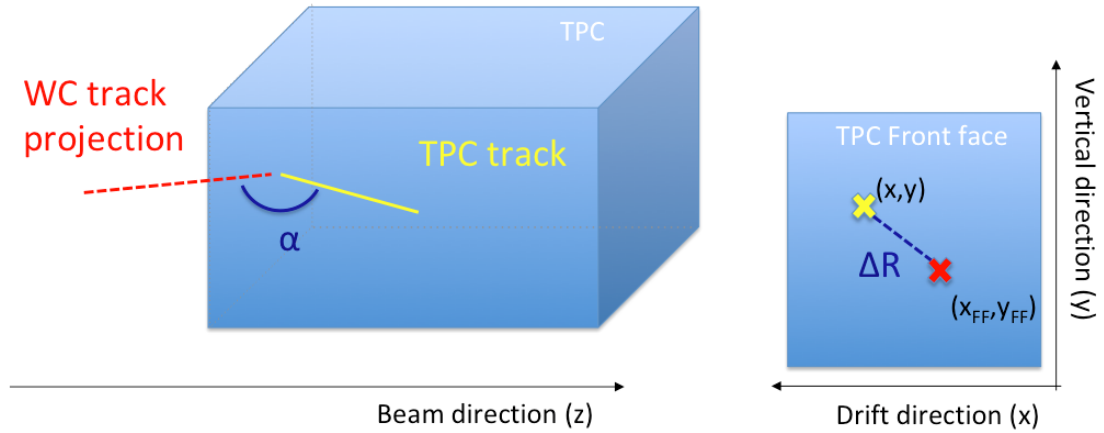


Figure 4.4: Visual rendering of the wire chamber to TPC match.

1709 4.3 The Thin Slice Method

1710 Once we have selected the pool of hadron candidates and we have identified the TPC
1711 track corresponding to the beamline event, we apply the thin slice method to measure
1712 the cross section, as the following sections describe.

1713 4.3.1 Cross Sections on Thin Target

1714 Cross section measurements on a thin target have been the bread and butter of
1715 nuclear and particle experimentalists since the Geiger-Marsden experiments [66]. At
1716 their core, this type of experiments consists in shooting a beam of particles with a
1717 known flux on a thin slab of material and recording the outgoing flux.

1718 In general even in the case of thin target, the target is not a single particle,
1719 but rather a slab of material containing many diffusion centers. The so-called “thin
1720 target” approximation assumes that the target centers are uniformly distributed in
1721 the material and that the target is thin compared to the projectile interaction length,
1722 so that no center of interaction sits in front of another. In this approximation, the
1723 ratio between the number of particles interacting in the target N_{Int} and the number of
1724 incident particles N_{Inc} on the target determines the interaction probability $P_{\text{Interacting}}$,

1725 which is the complementary to one of the survival probability $P_{Survival}$. Equation 4.2

$$P_{Survival} = 1 - P_{Interacting} = 1 - \frac{N_{Int}}{N_{Inc}} = e^{-\sigma_{TOT} n \delta X} \quad (4.2)$$

1726 describes the probability for a particle to survive the thin target. This formula relates
1727 the interaction probability to the total hadronic cross section (σ_{TOT}), the density of
1728 the target centers (n)¹ and the thickness of the target along the incident hadron
1729 direction (δX). If the target is thin compared to the interaction length of the process
1730 considered, we can Taylor expand the exponential function in equation 4.2 and find
1731 a simple proportionality relationship between the cross section and the number of
1732 incident and interacting particles, as shown in equation 4.3:

$$1 - \frac{N_{Int}}{N_{Inc}} = 1 - \sigma_{TOT} n \delta X + O(\delta X^2). \quad (4.3)$$

1733 Solving for the cross section, we find:

$$\sigma_{TOT} = \frac{1}{n \delta X} \frac{N_{Int}}{N_{Inc}}. \quad (4.4)$$

1734 4.3.2 Not-so-Thin Target: Slicing the Argon

1735 The interaction length of pions and kaons in argon is expected to be of the order
1736 of 50 cm for pions and 100 cm for kaons. Thus, the LArIAT TPC, with its 90 cm
1737 of length, is not a thin target. However, the fine-grained tracking of the LArIAT
1738 LArTPC allows us to treat the argon volume as a sequence of many adjacent thin
1739 targets.

1740 As described in Chapter 3, LArIAT wire planes consist of 240 wires each. The
1741 wires are oriented at +/- 60° from the vertical direction at 4 mm spacing, while the

1. The scattering center density in the target, n , relates to the argon density ρ , the Avogadro number N_A and the argon molar mass m_A as $n = \frac{\rho N_A}{m_A}$.

1742 beam direction is oriented 3 degrees off the z axis in the XZ plane. The wires collect
 1743 signals proportional to the energy loss of the hadron along its path in a $\delta X = 4$
 1744 mm/(sin(60°)cos(3°)) ≈ 4.7 mm slab of liquid argon. Thus, one can think to slice
 1745 the TPC into many thin targets of $\delta X = 4.7$ mm thickness along the direction of the
 1746 incident particle, making a measurement at each wire along the path.

1747 Considering each slice j a “thin target”, we can apply the cross section calculation
 1748 from Equation 4.4 iteratively, evaluating the kinetic energy of the hadron as it enters
 1749 each slice, E_j^{kin} . For each WC2TPC matched particle, the energy of the hadron
 1750 entering the TPC is known thanks to the momentum and mass determination by the
 1751 tertiary beamline,

$$E_{FrontFace}^{kin} = \sqrt{p_{Beam}^2 - m_{Beam}^2} - m_{Beam} - E_{loss}, \quad (4.5)$$

1752 where E_{loss} is a correction for the energy loss in the uninstrumented material between
 1753 the beamline and the TPC front face. The energy of the hadron at each slab is
 1754 determined by subtracting the energy released by the particle in the previous slabs.
 1755 For example, at the j^{th} point of a track, the kinetic energy will be

$$E_j^{kin} = E_{FrontFace}^{kin} - \sum_{i < j} E_{Dep,i}, \quad (4.6)$$

1756 where $E_{Dep,i}$ is the energy deposited at each argon slice before the j^{th} point as mea-
 1757 sured by the calorimetry associated with the tracking.

1758 If the particle enters a slice, it contributes to $N_{Inc}(E^{kin})$ in the energy bin corre-
 1759 sponding to its kinetic energy in that slice. If it interacts in the slice, it also contributes
 1760 to $N_{Int}(E^{kin})$ in the appropriate energy bin. The cross section as a function of kinetic
 1761 energy, $\sigma_{TOT}(E^{kin})$ will then be proportional to the ratio $\frac{N_{Int}(E^{kin})}{N_{Inc}(E^{kin})}$.

1762 Our goal is to measure the total interaction cross section, independently from the
 1763 topology of the interaction. Thus, we determine that a hadron interacted simply by

	min	max
X	1 cm	46 cm
Y	-15 cm	15 cm
Z	0 cm	86 cm

Table 4.2: Fiducial volume boundaries used to determine cross section interaction point.

requiring that the last point of the WC2TPC matched track lies inside the fiducial volume, whose boundaries are defined in Table 4.2. If the TPC track stops within the fiducial volume, its last point will be the interaction point; if the track crosses the boundaries of the fiducial volume, the track will be considered “through going” and no interaction point will be found. The only points of the hadronic candidate track considered to fill the N_{Inc}) and N_{Inc} plots are the ones contained in the fiducial volume.

4.3.3 Corrections to the Raw Cross Section

Equation 4.4 is a prescription for measuring the cross section in case of a pure beam of the hadron of interest and 100% efficiency in the determination of the interaction point. For example, if LArIAT had a beam of pure pions and were 100% efficient in determining the interaction point within the TPC, the pion cross section in each energy bin would be given by

$$\sigma_{TOT}^{\pi^-}(E_i) = \frac{1}{n\delta X} \frac{N_{\text{Int}}^{\pi^-}(E_i)}{N_{\text{Inc}}^{\pi^-}(E_i)}. \quad (4.7)$$

Unfortunately, this is not the case. In fact, the selection used to isolate pions in the LArIAT beam allows for the presence of some muons and electrons as background, while the kaon selection allows for a small percentage of protons (see Section 5.2.1). Also, the LArIAT TPC is not 100% efficient in determining the interaction point. Therefore we need to apply two corrections evaluated on the MC in order to

1782 extract the true cross section from LArIAT data: the background subtraction and
 1783 the efficiency correction. Still using the pion case as example, we estimate the pion
 1784 cross section in each energy bin changing Equation 4.7 into

$$\sigma_{TOT}^{\pi^-}(E_i) = \frac{1}{n\delta X} \frac{N_{Int}^{\pi^-}(E_i)}{N_{Inc}^{\pi^-}(E_i)} = \frac{1}{n\delta X} \frac{\epsilon^{Inc}(E_i)[N_{Int}^{TOT}(E_i) - B_{Int}(E_i)]}{\epsilon^{Int}(E_i)[N_{Inc}^{TOT}(E_i) - B_{Inc}(E_i)]}, \quad (4.8)$$

1785 where $N_{Int}^{TOT}(E_i)$ and $N_{Inc}^{TOT}(E_i)$ is the measured content of the interacting and
 1786 incident histograms for events that pass the event selection, $B_{Int}(E_i)$ and $B_{Inc}(E_i)$
 1787 represent the contributions from the background to the interacting and incident his-
 1788 tograms respectively, and $\epsilon^{Int}(E_i)$ and $\epsilon^{Inc}(E_i)$ are the efficiency corrections for said
 1789 histograms.

1790 As we will show in section 5.3, the background subtraction for the interacting
 1791 and incident histograms can be translated into a corresponding relative pion content
 1792 $C_{Interacting}^{\pi MC}(E_i)$ and $C_{Incident}^{\pi MC}(E_i)$ and the cross section re-written as follows

$$\sigma_{TOT}^{\pi^-}(E_i) = \frac{1}{n\delta X} \frac{\epsilon^{Inc}(E_i)}{\epsilon^{Int}(E_i)} \frac{C_{Int}^{\pi MC}(E_i)}{C_{Inc}^{\pi MC}(E_i)} \frac{N_{Int}^{TOT}(E_i)}{N_{Inc}^{TOT}(E_i)}. \quad (4.9)$$

1793 4.4 Procedure testing with truth quantities

1794 The (π^-, Ar) and (K^+, Ar) total hadronic cross section implemented in Geant4 can be
 1795 used as a tool to validate the measurement methodology. We describe here a closure
 1796 test done on Monte Carlo to prove that the methodology of slicing the TPC retrieves
 1797 the underlying cross section distribution implemented in Geant4 within the statistical
 1798 uncertainty.

1799 For pions and kaons in the considered energy range, the Geant4 inelastic model
 1800 adopted is “BertiniCascade”; the pion elastic cross sections are tabulated from on
 1801 Chips, while the kaon elastic cross sections are tabulated on Gheisha and Chips.

1802 For the validation test, we fire a sample of pions and a sample of kaons inside the

1803 LArIAT TPC active volume using the Data Driven Monte Carlo (see section 5.2.2).
1804 We apply the thin-sliced method using only true quantities to calculate the hadron
1805 kinetic energy at each slab in order to decouple reconstruction effects from possible
1806 issues with the methodology. For each slab of 4.7 mm length along the path of the
1807 hadron, we integrate the true energy deposition as given by the Geant4 transportation
1808 model. Then, we recursively subtracted it from the hadron kinetic energy at the TPC
1809 front face to evaluate the kinetic energy at each slab until the true interaction point is
1810 reached. Since the MC is a pure beam of the hadron of interest and truth information
1811 is used to retrieve the interaction point, no correction is applied. Doing so, we obtain
1812 the true interacting and incident distributions for the considered hadron, from which
1813 we derive the true MC cross section as a function of the hadron true kinetic energy.

1814 Figure 4.5 shows the total hadronic cross section for argon implemented in Geant4
1815 10.03.p1 (solid lines) overlaid with the true MC cross section as obtained with the
1816 sliced TPC method (markers) for pions on the left and kaons on the right; the total
1817 cross section is shown in green, the elastic cross section in blue and the inelastic
1818 cross section in red. The nice agreement with the Geant4 distribution and the cross
1819 section obtained with the sliced TPC method gives us confidence in the validity of
1820 the methodology.

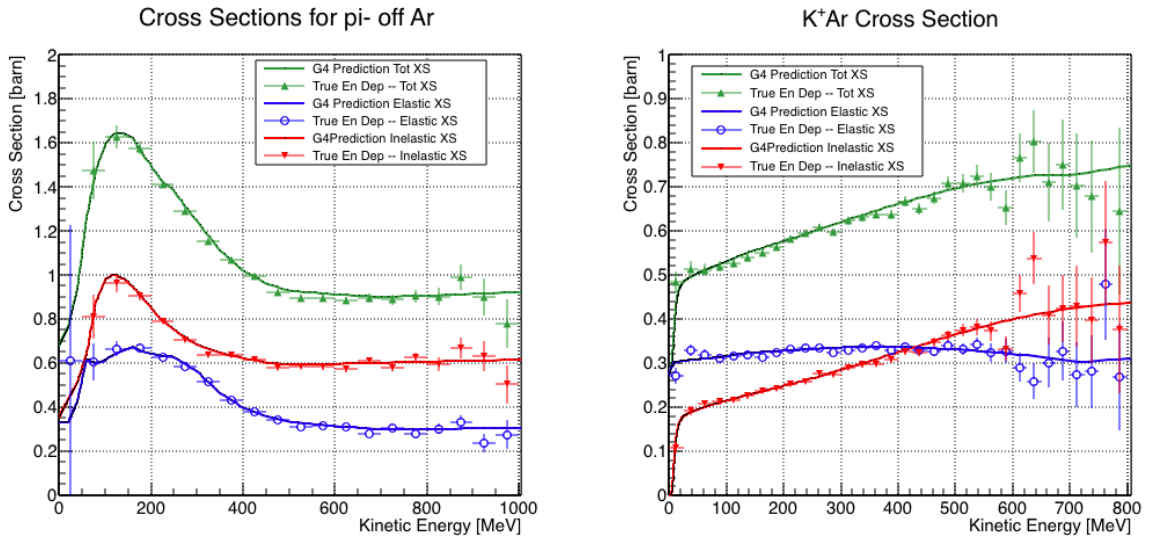


Figure 4.5: Hadronic cross sections for (π^- ,Ar) on the left and (K^+ ,Ar) on the right as implemented in Geant4 10.03.p1 (solid lines) overlaid the true MC cross section as obtained with the sliced TPC method (markers). The total cross section is shown in green, the elastic cross section in blue and the inelastic cross section in red.

1821 **Chapter 5**

1822 **Data and MC preparation for the**
1823 **Cross Section Measurements**

1824 “*Il dolce non lo mangi mai, ma qualche volta ti rifai.*
1825 *Abbracciami*”
1826 – Pietro Ciampi, L’amore e’ tutto qui, 1971 –

1827 This chapter describes the work done on the data and Monte Carlo samples in
1828 preparation for the cross section analyses. This entails the choice of the datasets
1829 and the production of the information needed to construct the Monte Carlo Simula-
1830 tion (Section 5.1), the construction and use of said Monte Carlo simulation (section
1831 5.2), the study of backgrounds for the pion cross section (Section 5.3), the study of
1832 the energy loss between WC4 and TPC (Section 5.4), the study of the tracking in the
1833 TPC (Section 5.5), and study of the calorimetry response (Section 5.6).

1834 **5.1 Cross Section Analyses Data Sets**

1835 We choose LArIAT Run-II as the data period for the (π^- ,Ar) and (K^+ ,Ar) total
1836 hadronic cross section analyses. Data taking for the this period started on 03/15/2016

1837 and ended on 07/31/2016. Since we are interested in beamline and TPC information,
1838 we ask basic requirements on the operational status of the time of flight, wire chambers
1839 and TPC to form the good run list for this period, which we informally call “lovely
1840 runs”.

1841 The subset of lovely runs chosen for the (π^- ,Ar) total hadronic cross section
1842 analysis includes only the -60A and -100A magnet configurations in negative polarity,
1843 even if LArIAT explored several other beamline configurations during Run-II. The -
1844 60A and -100A combined data set accounts for approximately 90% of the total Run-II
1845 negative polarity runs. The choice of the main two beamline settings limits the need
1846 for the production of many different MC sets and related corrections, still maintaining
1847 a high number of events.

1848 Similarly, the subset of lovely runs chosen for the (K^+ ,Ar) total hadronic cross
1849 section analysis includes only the +60A and +100A magnet configurations in positive
1850 polarity. It should be noted that kaons are extremely rare in the +60A sample, thus
1851 the data sample for the (K^+ ,Ar) cross section after the mass selection is about 90%
1852 +100A runs, as shown in Table 5.1.

1853 For the first measurements in LArIAT that uses both beamline and TPC infor-
1854 mation, we choose strict requirements on the reconstruction of the WC tracks, the
1855 so-called “Picky Track” sample (see Section 3.2.2). This choice presents two ad-
1856 vantages: the uncertainty on the momentum reconstruction for the “Picky Tracks”
1857 sample is smaller compared to the “High Yield” sample, and the comparison with
1858 the beamline MC results is straightforward. A possible future update and cross check
1859 of these analysis would be the use of the High Yield sample, where the statistics is
1860 about three times higher.

1861 The breakdown of beamline events as a function of the magnets settings is shown
1862 in Table 5.1. The choice of the data sets determines the production of beamline MC
1863 and serves as basis for the production of Data Driven MC, as shown in the next

1864 sections.

1865 5.2 Construction of a Monte Carlo Simulation for 1866 LArIAT

1867 For the simulation of LArIAT events and for the simulation of the datasets' particle
1868 make up, we use a combination of two MC generators: the G4Beamline Monte Carlo
1869 and the Data Driven single particle Monte Carlo (DDMC). We use the G4Beamline
1870 MC to simulate the particle transportation in the beamline and calculate the particle
1871 composition of the beam just after the fourth Wire Chamber (WC4). In order to
1872 simulate the beamline particles after WC4 and in the TPC, we use the DDMC.

1873 5.2.1 G4Beamline

1874 G4Beamline simulates the beam collision with the LArIAT secondary target, the
1875 energy deposited by the particles in the LArIAT beamline detectors, and the action
1876 of the LArIAT magnets, effectively accounting for particle transportation through the
1877 beamline from the LArIAT target until "Big Disk", a fictional, void detector located
1878 just before the LArIAT cryostat. At the moment of this writing, G4Beamline does
1879 not simulated the responses of the beamline detectors. It is possible to interrogate the
1880 truth level information of the simulated particles in several points of the geometry.
1881 In order to ease the handshake between G4Beamline and the DDMC, we ask for
1882 the beam composition just after WC4. Since LArIAT data are taken under different

	I = 60 A	I = 100 A	Total
Data Events after $\pi/\mu/e$ Mass Selection	67068	71413	138481
Data Events after K Mass Selection	274	2563	2837

Table 5.1: Number of data events which fit the $\pi/\mu/e$ or K mass hypothesis as a function of magnet settings.

beam conditions, we need to simulate separately the beam composition according to the magnets' settings and the secondary beam intensity with G4Beamline. For the pion cross section analysis the relevant beam conditions are secondary beam energy of 64 GeV, negative polarity magnet with current of 100 A and 60 A. For the kaon cross section analysis the relevant beam conditions is a secondary beam energy of 64 GeV, positive polarity magnet with current of 100 A.

Beam Composition for Negative Pion Cross Section

Even if pions are by far the biggest beam component in negative polarity runs, the LArIAT tertiary beam is not a pure pion beam. While useful to discriminate between pions, kaons, and protons, the beamline detectors are not sensitive enough to discriminate among the lighter particles in the beam: electrons, muons and pions fall under the same mass hypothesis. Thus, we need to assess the contamination from beamline particles other than pions in the event selections used for the pion cross section analysis and correct for its effects. The first step of this process is assessing the percentage of electrons and muons in the $\pi/\mu/e$ beamline candidates via the G4Beamline MC. Since the beamline composition is a function of the magnet settings, we simulate separately events for magnet current of -60A and -100A. Figure 5.1 shows the momentum predictions from G4Beamline overlaid with data for the 60A runs (left) and for the 100A runs (right). The predictions for electrons, muons and pions have been staggered and their sum is area normalized to data. Albeit not perfect, these plots show a reasonable agreement between the momentum shapes in data and MC. We attribute the difference in shape to a two approximations performed in the MC. Firstly, G4Beamline lacks the simulation of the WC efficiency which is momentum dependent and leads to enhance the number events in the center of the momentum distribution. Secondly, G4Beamline stop tracking pions and their products if they decay in after WC1; in data, pion decays in flight can still create a

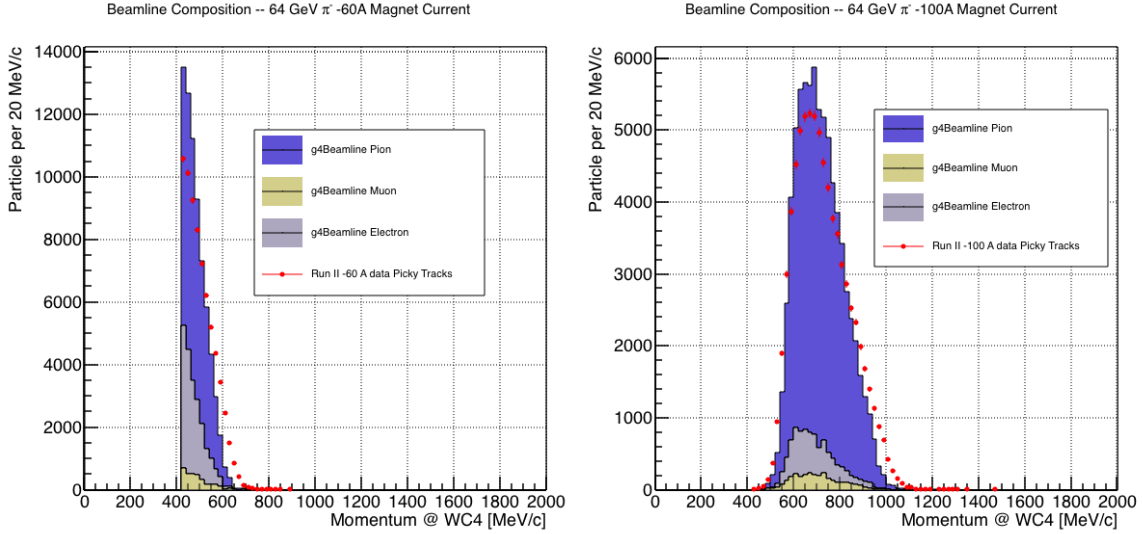


Figure 5.1: Beam composition for the -60A runs (left) and -100A runs (right). The solid blue plot represents the simulated pion content, the yellow plot represents the simulated muon content and the grey plot represents the simulated electron content. The plots are area normalized to the number of data events, shown in red.

	I = -60 A	I = -100 A
G4Pions	68.8 %	87.4 %
G4Muons	4.6 %	3.7 %
G4Electrons	26.6 %	8.9 %

Table 5.2: Simulated beamline composition per magnet settings

1909 trigger if the produced muon travels thought the beamline detectors. In the pion cross
 1910 section analysis, these differences between data and G4Beamline are accounted for as
 1911 a systematic uncertainty related to the beam composition (see Section 6.2.1).

1912 Table 5.2 shows the beam composition per magnet setting after the mass selection
 1913 according to the G4Beamline simulation.

1914 The estimated beam composition is used as a basis to estimate the background
 1915 contamination in the (π^-, Ar) cross section measurement, whose full treatment is
 1916 described in section 5.3.

1917 **Beam Composition for Positive Kaon Cross Section**

1918 In the positive polarity runs, the tertiary beam composition is mainly pions and
1919 protons. The left side of Figure 5.2 shows the predictions for the momentum spectra
1920 for the 100A positive runs according to G4Beamline (solid colors) overlaid with data
1921 (black points). Since the LArIAT beamline detectors can discriminate between kaons
1922 and other particles, we do not rely on the G4Beamline simulation to estimate the
1923 beamline contamination in the pool of kaon candidates (as in the case of the pion
1924 cross section), but rather we use a data driven approach. The basic idea of this data
1925 driven approach is to estimate the bleed over from high and low mass peaks under
1926 the kaon peak by fitting the tails of the $\pi/\mu/e$ and proton mass distributions, as
1927 shown in Figure 5.2 right side. Since the shape of the tails is unknown, the estimate
1928 is done multiple times varying the range and shape for reasonable functions. For
1929 example, to estimate the proton content under the kaon peak, we start by fitting the
1930 left tail of the proton mass distribution with a gaussian function between $650 \text{ MeV}/c^2$
1931 and $750 \text{ MeV}/c^2$. We extend the fit function under the kaon peak and integrate the
1932 extended fit function between $350-650 \text{ MeV}/c^2$. We integrate the mass histogram
1933 in the same range and calculate the proton contamination as the ratio between the
1934 two integrals. We repeat this procedure for several fit shapes (gaussian, linear and
1935 exponential functions) and tail ranges. Finally, we calculate the contamination as
1936 the weighted average of single estimates, where the weights are calculated to be the
1937 $1./|1 - \chi^2|$ of the tail fits. The procedure is repeated for lighter particles mass peak
1938 independently. With 12 iterations of this method we find a proton contamination of
1939 $5.0 \pm 2.0 \%$ and a contamination from the lighter particles of $0.2 \pm 0.5 \%$. The
1940 estimate of the proton background is currently not used in the kaon cross section
1941 analysis, but it is a fundamental step to retrieve the true kaon cross section which
1942 will be implemented in the further development of the analysis.

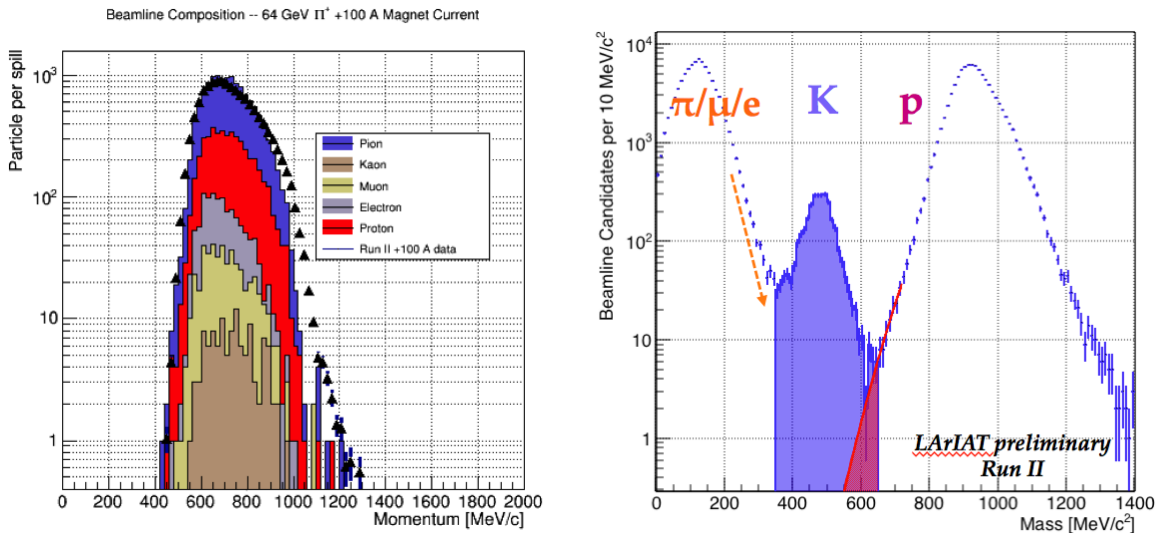


Figure 5.2: *Left:* Beam composition for the +100A runs after WC4 (no mass selection applied). The solid colors represent the contributions from the G4Beamline simulated particles: blue plot represents the simulated pion content, the yellow plot represents the simulated muon content and the grey plot represents the simulated positron content, the red the proton content and the mustard the kaon content. The plots are area normalized to the number of data events, shown in black. *Right:* Mass distribution for the Run-II positive runs, where the area under the kaon mass peak is highlighted in purple. The area under the extension of a possible fit for the proton tail is highlighted in red.

1943 **5.2.2 Data Driven MC**

1944 The Data Driven single particle Monte Carlo (DDMC) is a single particle gun which
1945 simulates the particle transportation from WC4 into the TPC leveraging on the beam-
1946 line data information. The DDMC uses the data momentum and position at WC4
1947 to derive the event generation: a general sketch of the DDMC workflow is shown in
1948 Figure 5.3.

1949 When producing a DDMC sample, beamline data from a particular running pe-
1950 riod and/or running condition are selected first. For example, data for the negative
1951 60A runs and for the negative 100A runs inform the event generation stage of two
1952 different DDMC samples. Figure 5.4 schematically shows the data quantities of in-
1953 terest leveraged from data: the momentum (P_x, P_y, P_z) and position (X, Y) at WC4.
1954 For each data event, we obtain the particle position (X, Y) at WC4 directly from the
1955 data measurement; we calculate the components of the momentum using the beam-
1956 line measurement of the momentum magnitude in conjunction with the hits on WC3
1957 and WC4 to determine the direction of the momentum vector, as described in section
1958 3.2.2. The momentum and position of the selected data form a 5-dimensional tuple,
1959 which we sample thousands of times through a 5-dimensional hit-or-miss sampling
1960 procedure to generate the MC events. This sampling generates MC events with the
1961 same momentum and position distributions as data, with the additional benefit of
1962 accounting for the correlations between the P_x, P_y, P_z, X, Y variables. As an example,
1963 the results of the DDMC generation compared to data for the kaon +100A sample
1964 are shown in figure 5.5 for the P_z, X and Y distributions; as expected, MC and data
1965 agree within the statistical uncertainty by construction. A LArSoft simulation mod-
1966 ule then launches single particle MC from $z = -100$ cm (the location of the WC4)
1967 using the generated events. The particles are free to decay and interact in their path
1968 from WC4 to the TPC according to the Geant4 simulation.

1969 Using the DDMC technique ensures that the MC and data particles have very

1970 similar momentum, position and angular distributions at WC4 and allows us to use
 1971 the MC sample in several occasions: to estimate the background contamination to
 1972 the pion cross section (see Section 5.3), to calibrate the energy loss upstream of the
 1973 TPC (see Section 5.4), or to study the tracking and the calorimetric performance
 1974 (sections 5.5 and 5.6). A small caveat is in order here: the DDMC is a single particle
 1975 Monte Carlo, which means that the beam pile-up is not simulated.

1976 We generate six samples for the pion cross section measurement: three samples
 1977 of ~ 330000 pions, muons and electrons to simulate the negative 60A runs, and three
 1978 samples of ~ 340000 pions, muons and electrons for the negative 100A runs. We
 1979 generate a sample of 195000 kaons for the kaon cross section analysis.

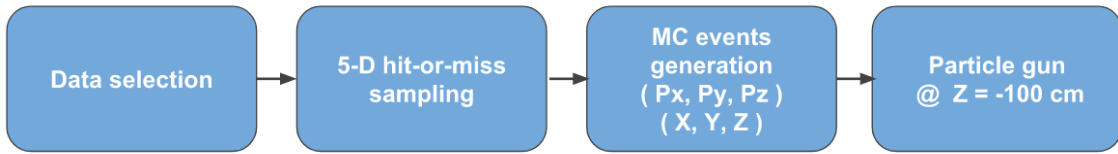


Figure 5.3: Workflow for Data Driven single particle Monte Carlo production.

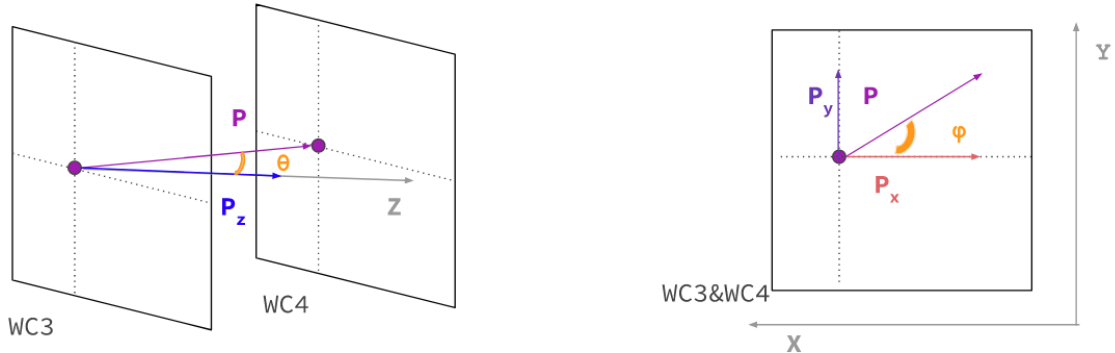


Figure 5.4: Scheme of the quantities of interest for the DDMC event generation:
 P_x, P_y, P_z, X, Y at WC4.

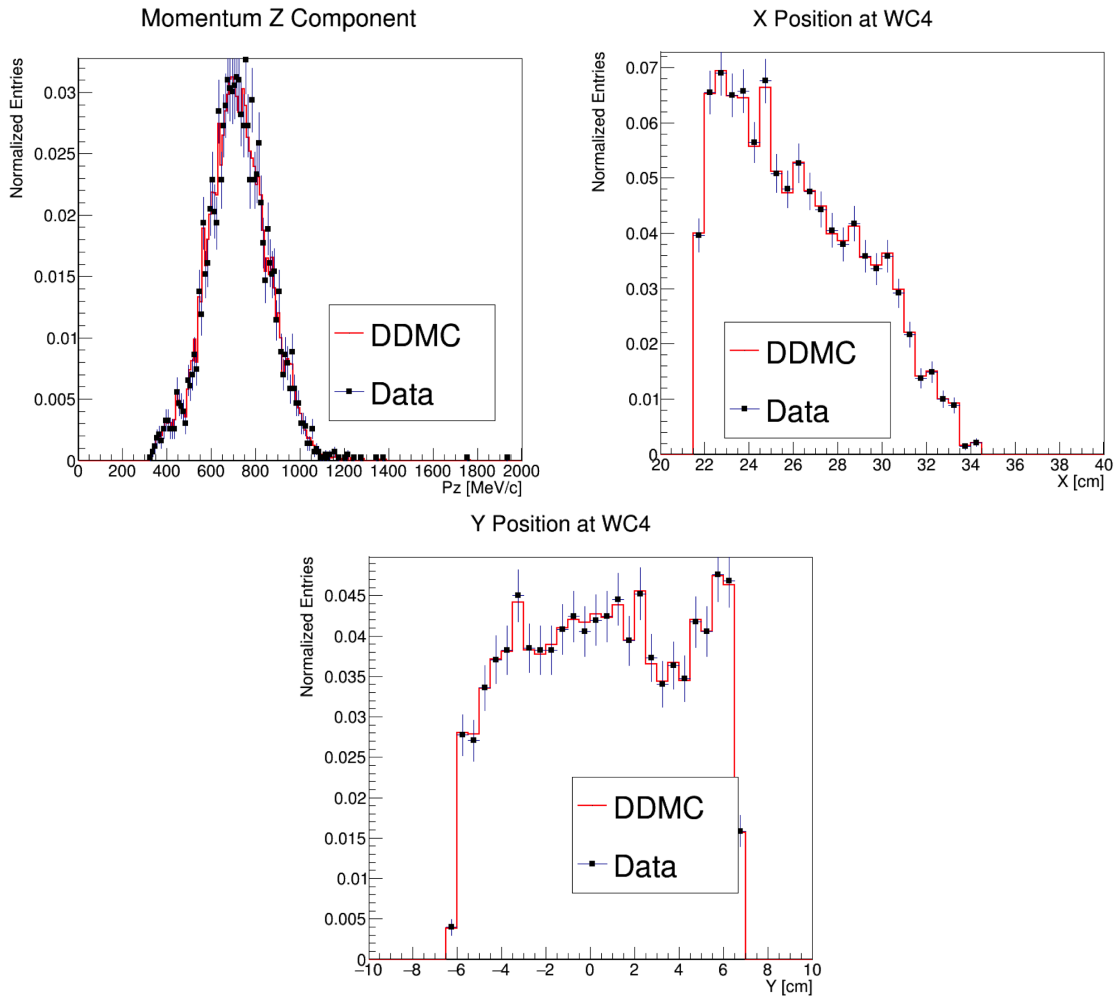


Figure 5.5: Comparison between generated quantities and data distributions for the 100A kaon sample: Z component of the momentum at WC4 (top left), X position at Wire Chamber 4 (top right), Y position at Wire Chamber 4 (bottom).

1980 **5.3 Estimate of Backgrounds in the Pion Cross**
1981 **Section**

1982 We use the beamline simulation and the DDMC simulation to estimate the back-
1983 ground in the total hadronic pion cross section. Two categories of background exists
1984 for the negative pion cross section measurement: the one related to the pion interac-
1985 tion in the chamber, discussed in Section 5.3.1 and the one related to the beamline
1986 contamination, discussed in Section 5.3.2.

1987 **5.3.1 Background from Pion Capture and Decay**

1988 Our goal is to measure the total hadronic cross section for negative pions in argon.
1989 Since pion capture can be classified as an electromagnetic process and pion decay is a
1990 weak process, capture and decay represent unwanted interactions. We present here a
1991 study of capture and decay in Monte Carlo and the solution we adopted to mitigate
1992 their occurrence in the data sample.

1993 For this MC study, we use a sample of MC pions generated according to the
1994 –60A beam profile with the DDMC (see Section 5.2.2). It is important to notice
1995 that capture occurs predominantly at rest, while decay may occur both in flight and
1996 at rest. Thus, we can highly mitigate capture and decay at rest by removing pions
1997 which would release all their energy in the TPC and stop. This translates into a
1998 momentum selection, where we keep only events whose WC momentum is above a
1999 certain threshold. Figure 5.6 shows the true momentum distribution for the primary
2000 pions¹ that arrive to the TPC (pink), that capture (green) or decay (blue) inside the
2001 TPC, on a linear scale (left) and on a log scale (right) vertical axis.

1. We use here the Geant4 denomination “primary” to indicate that the pion considered does not undergo interactions modifying its energy before getting to the TPC. In fact, not every pion shot from wire chamber four will arrive to the TPC as primary, some will decay or interact before the TPC.

2002 In order to choose the selection value for the wire chamber momentum, it is
2003 beneficial to estimate the ratio of events which capture or decay that survive the
2004 selection in MC as a function of the momentum threshold, and compare it with the
2005 survival ratio for all the 60A events. This is done in figure 5.7. We define the survival
2006 ratio simply as the number of events surviving the true momentum selection divided
2007 by the number of events of that category. We calculate the survival ratio separately
2008 for the three event categories explained above: total (pink), capture (green) and decay
2009 (blue). Selecting pions with momentum greater than 420 MeV/c reduces the capture
2010 events by 99% while maintaining about 80% of the 60A data sample and almost
2011 the entire 100A sample. Figure 5.8 shows the ratio of events which end their life in
2012 capture (green) or decay (blue) over the total number of events as a function of
2013 the true momentum at wire chamber four. This ratio is slightly dependent on the
2014 inelastic cross section implemented in Geant4, as we are able to register a pion capture
2015 (or decay) only if it did not interact inelastically in the TPC. We choose a momentum
2016 threshold of 420 MeV/c because the percentage of capture events drops below 1% and
2017 the percentage of decays is never above 2% for momenta greater than 420 MeV/c.
2018 After the momentum selection, we evaluate the contribution of capture and decay to
2019 be a negligibly small background to the cross section measurement compared to the
2020 background related to the beamline which we will address in the next section.

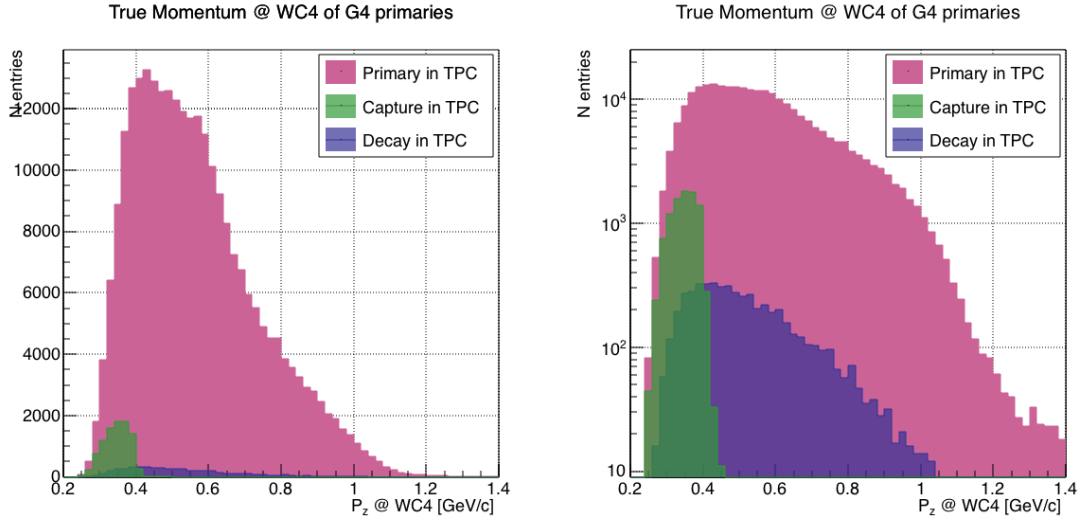


Figure 5.6: True momentum distribution at wire chamber 4 for every simulated pion arriving in the TPC (pink), ending its life in capture (green) or in decay (blue) in the TPC, linear vertical axis on the left, logarithmic on the right.

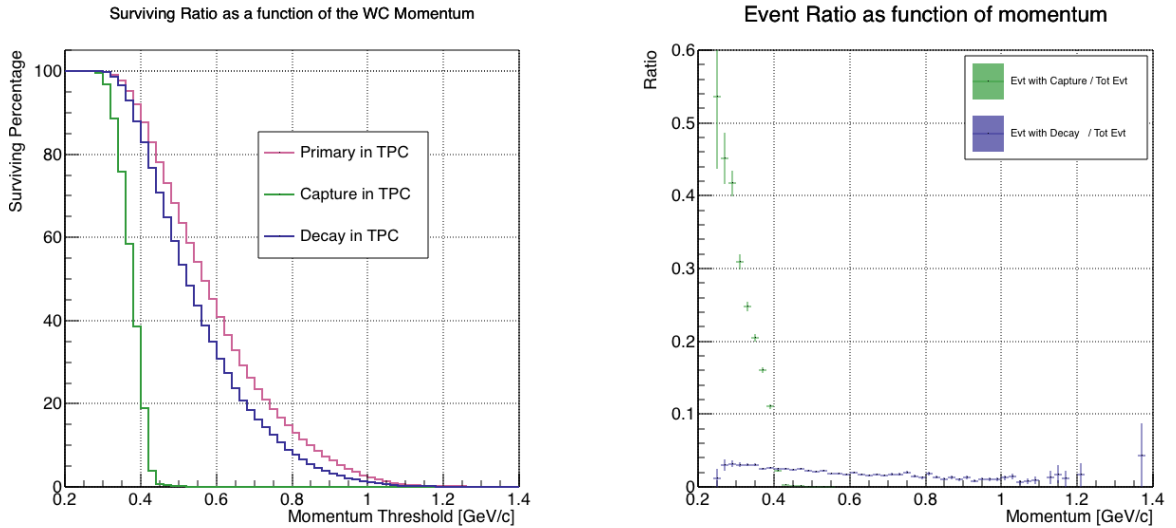


Figure 5.7: Survival ratio as a function of selection threshold on true momentum at wire chamber four for every simulated pion arriving in the TPC (pink), capture (green) or in decay (blue).

Figure 5.8: Ratio between the capture (green) and decay (blue) events over the total number of events as a function of the true momentum at wire chamber four.

2021 **5.3.2 Contributions from the Beamline Background**

2022 We define beamline background every TPC track matched to the WC track which is
2023 not a primary pion. Potentially, there are 4 different types of beamline background:

2024 1) electrons,

2025 2) muons,

2026 3) secondaries from pion events,

2027 4) matched pile up events.

2028 The first step to quantify the effect of the beamline background on the pion cross
2029 section is to estimate what percentage of events used in the cross section calculation
2030 is not a primary pion. We start by noting that the last type of background, the
2031 “matched pile up” events, is a negligible fraction, because of the definition of the
2032 WC2TPC match: we deem the probability of a single match with a halo particle in
2033 the absence of a beamline particle² negligibly small. As shown in Section 5.2.1, we
2034 use G4Beamline to estimate the percentage of pions, muons and electrons at WC4,
2035 obtaining the composition shown in Table 5.2. The next step is to simulate those
2036 pions, muons and electrons from WC4 to the TPC with the DDMC and evaluate their
2037 contribution to the cross section. To do so, we start by simulating the same number
2038 of electrons, muons and pions with the DDMC and we apply the same selection chain
2039 (i.e. track multiplicity rejection, WC2TPC acceptance and shower rejection) on the
2040 three samples. The number of events per particle species surviving this selection is
2041 shown on table 5.3. In order to reproduce the closest make up of the beam to data,
2042 we weight each event of a given particle species according to the estimated beam
2043 composition. In case of 60A runs, for example, the weights are 0.688 for pions, 0.046
2044 for muons and 0.266 for electrons.

2. Events with multiple WC2TPC matches are always rejected.

	Magnet Current -60A			Magnet Current -100 A		
	MC π^-	MC μ^-	MC e^-	MC π^-	MC μ^-	MC e^-
Total Initial events	334500	334500	334500	344500	344500	344500
After Multiplicity Rejection	330668	333420	198065	326576	344208	201380
After WC2TPC Selection	218239	296333	91139	230418	300228	98834
Evts After Shower Rejection	208063	288914	20293	219882	293585	17780
Selection Survival Rate	62.3%	86.6%	6.1%	63.8%	85.5%	5.2%
Beam Composition @WC4	68.8%	4.6 %	26.6 %	87.4 %	3.7 %	8.9 %
Beam Composition @TPC FF	88.5%	8.2%	3.3 %	94.0%	5.3%	0.7%

Table 5.3: MC selection flow per particle species.

2045 It should be noted that pions may interact hadronically in the steel or in the
 2046 non-instrumented argon upstream to the TPC front face while travelling the length
 2047 of between WC4 and the TPC. Or, they could decay in flight between WC4 and the
 2048 TPC. One of the interaction products can leak into the TPC and be matched with the
 2049 WC track, contributing to the pool of events used for the cross section calculation. We
 2050 call this type of particles “secondaries” from pion events, with a terminology inspired
 2051 by Geant4. We estimate the number of secondaries using the DDMC pion sample.
 2052 The percentage of secondaries is given by the number of matched WC2TPC tracks
 2053 whose corresponding particle is not flagged as primary by Geant4. The secondary to
 2054 pion ratio is 4.9% in the 60A sample and 4.3% in the 100A sample.

2055 We evaluate the beamline background contribution to the cross section by pro-
 2056 ducing the interacting and incident histograms for the events surviving the selection,
 2057 staggering the contributions for each particle species, as shown in Figure 5.9. From
 2058 those histograms, we are able to evaluate the contribution of pions and beamline
 2059 backgrounds to each bin of the interacting and incident histograms separately and
 2060 obtain the relative pion content. The relative pion content in each bin for the inter-
 2061 acting and incident histograms represents the correction applied to data. We take

here the interacting histogram as example, noting that the derivation of the correction for the incident histogram is identical. The number of entries in each bin of the interacting plot (Figure 5.9 left) is $N_{\text{Int}}^{\text{TOT}}(E_i)$, equal to the sum of the pions and beamline backgrounds in that bin, namely

$$N_{\text{Int}}^{\text{TOT}}(E_i) = N_{\text{Int}}^{\pi}(E_i) + \underbrace{N_{\text{Int}}^{\mu}(E_i) + N_{\text{Int}}^e(E_i) + N_{\text{Int}}^{\text{Secondary}}(E_i)}_{B_{\text{Int}}(E_i)}. \quad (5.1)$$

Thus, the relative pion content to each bin in MC can be calculated as follows

$$C_{\text{Int}}^{\pi MC}(E_i) = \frac{N_{\text{Int}}^{\pi MC}}{N_{\text{Int}}^{\text{TOTMC}}(E_i)} = \frac{N_{\text{Int}}^{\text{TOTMC}}(E_i) - B_{\text{Int}}^{MC}(E_i)}{N_{\text{Int}}^{\text{TOTMC}}(E_i)}. \quad (5.2)$$

In order to evaluate the pion content of each bin in data, we scale the measured bin by the corresponding relative pion content found in MC, as follows

$$N_{\text{Int}}^{\pi RecoData} = N_{\text{Int}}^{\text{TOTData}}(E_i) - B_{\text{Int}}^{\text{Data}}(E_i) = C_{\text{Int}}^{\pi MC}(E_i)N_{\text{Int}}^{\text{TOTData}}(E_i). \quad (5.3)$$

The pion content is evaluated separately in the interacting and incident histograms. Their ratio determines a correction to the measured raw cross section. For example, the measured raw cross section of a sample with enhanced muons content will tend to be lower than the raw cross section of a muon free sample. This is because most of the muons will cross the TPC without stopping, thus contributing almost exclusively to the incident histogram, forcing the pion content to be lower in the incident histogram than in the interacting; thus, the correction will tend to enhance the cross section.

2077 5.4 Estimate of Energy Loss before the TPC

2078 The beamline particles travel a path from where their momentum is measured in
2079 the beamline until they are tracked again inside the TPC. In the LArIAT geometry,
2080 a particle leaving the WC4 will encounter the materials listed in Table 5.4 before
2081 being registered again. The energy lost by the particle in this non-instrumented
2082 material modifies the particle's kinetic energy and directly affects the cross section
2083 measurement, as shown in equation 4.5.

Material	density [g/cm ³]	width [cm]
Fiberglass laminate (G10)	1.7	1.28
Liquid Argon	1.4	3.20
Stainless Steel	7.7	0.23
Titanium	4.5	0.04
Air	$1.2 \cdot 10^{-3}$	89.43
Plastic Scintillator	1.03	1.20 (+ 1.30)

Table 5.4: LArIAT material budget from WC4 to the TPC Front Face.

We derive an estimate of the energy loss between the beamline momentum measurement and the TPC (E_{loss}) from the pion and kaon DDMC samples, since this quantity is not measurable directly on data. The E_{loss} distribution for the 60A and 100A pion sample is shown in figure 5.10, left and right respectively. The E_{loss} distribution for the whole kaon sample is shown in figure 5.11. A clear double peaked structure is visible, which is due to the particles either missing or hitting the HALO paddle: a schematic rendering of this occurrence is shown in figure 5.12. The kinematic at WC4 determines the trajectory of a particle and whether or not it will hit the halo paddle. In figure 5.13 , we plot the true horizontal component of the momentum P_x versus the true X position at WC4 for pions missing the halo paddle (left) and for pions hitting the halo paddle (right) for the -60A MC simulation runs – analogous plots are obtained with the -100A pion simulation and with the kaon simulation. These distributions can be separated drawing a line in this position-momentum space.

We use a logistic regression [13] as a classifier to find the best separating line, shown in both plots as the red line. We classify as “hitting the halo paddle” all pions whose P_x and X are such that

$$P_x + 0.02 * X - 0.4 < 0$$

and as “missing the halo paddle” all pions whose P_x and X are such that

$$P_x + 0.02 * X - 0.4 > 0,$$

where the coefficients of the line are empirically found by the logistic regression estimation. Overall, this simple method classifies in the right category (hit or miss) about 86% of the pion events. In MC, we assign $E_{loss} = 32 \pm 4$ MeV for pion events classified as “hitting the halo paddle”; we assign $E_{loss} = 24 \pm 3$ MeV for pion events classified as “missing the halo paddle”. We apply the same classifier on data.

A scan of the simulated geometry showed an excess of 3 cm of uninstrumented argon compared with the surveyed detector geometry. We account for this difference by assigning in data $E_{loss} = 24 \pm 6$ MeV for pion events classified as “hitting the halo paddle” and $E_{loss} = 17 \pm 6$ MeV for pion events classified as “missing the halo paddle”, where the uncertainty is derived as the standard deviation of the double peaked distribution.

The summary of the values for used for E_{Loss} for the pion sample is listed in table 5.5 with the analogous results for the study on the kaon case.

	E_{loss} [MeV]	
	Hitting Halo	Missing Halo
Pion MC	32 ± 4	24 ± 3
Pion Data	25 ± 6	17 ± 6
Kaon MC	38 ± 6	31 ± 5
Kaon Data	26 ± 7	22 ± 7

Table 5.5: Energy loss for pions and kaons.

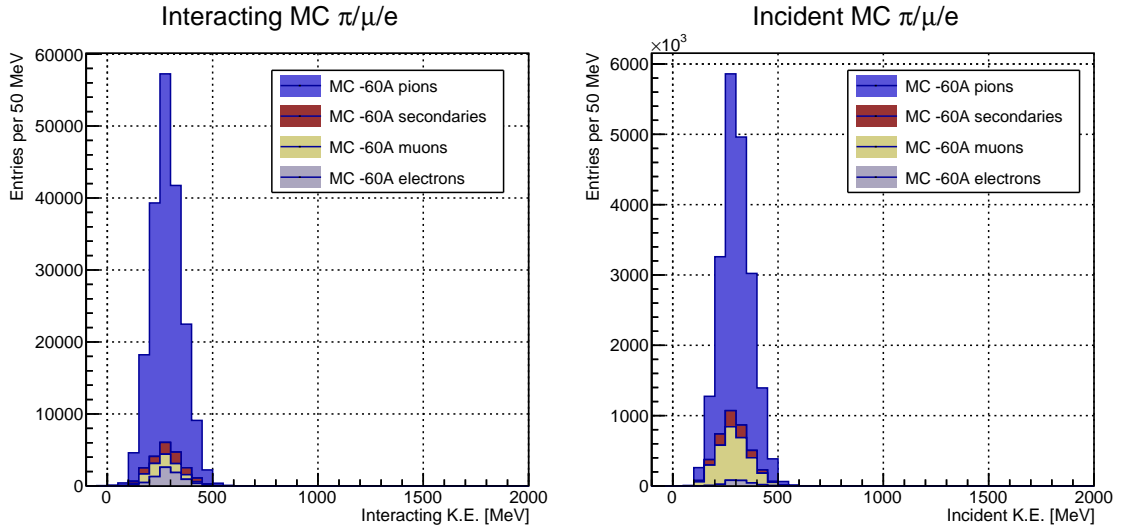


Figure 5.9: Left: staggered contributions to the interacting kinetic energy distribution for electron (grey), muons (yellow) and pion (blue) in the 60A simulation sample. Right: staggered contributions to the incident kinetic energy distribution for electron (grey), muons (yellow) and pion (blue) in the 60A simulation sample.

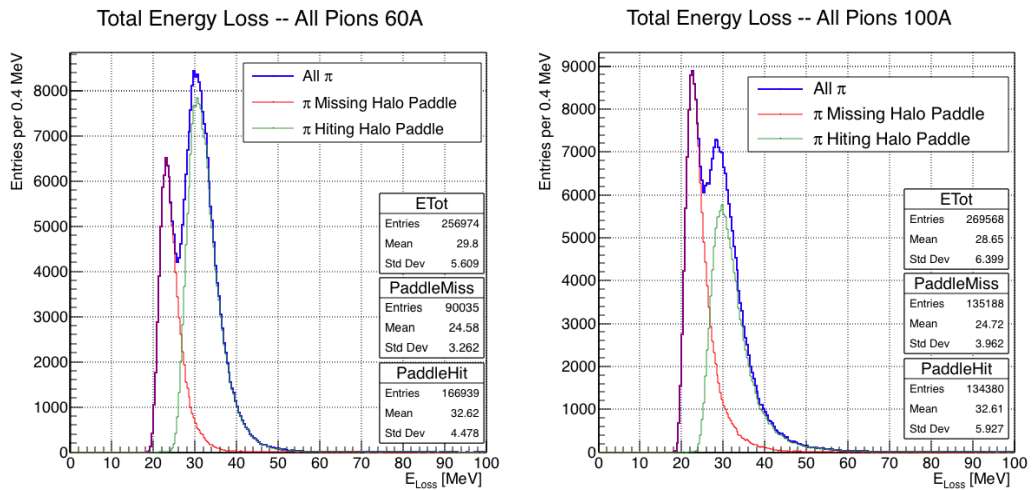


Figure 5.10: True energy loss between WC4 and the TPC front face according to the MC simulation of negative pions of the 60A runs (left) and of the 100A runs (right). The distribution for the whole data sample is shown in blue, the distribution for the pions missing the halo is shown in red, and the distribution for the pions hitting the halo is shown in green.

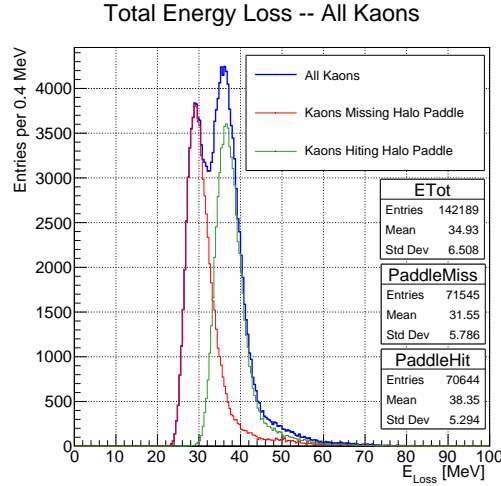


Figure 5.11: True energy loss between WC4 and the TPC front face according to the MC simulation of positive kaons in the 60A and 100A combined sample. The distribution for the whole data sample is shown in blue, the distribution for the kaons missing the halo is shown in red, and the distribution for the kaons hitting the halo is shown in green.

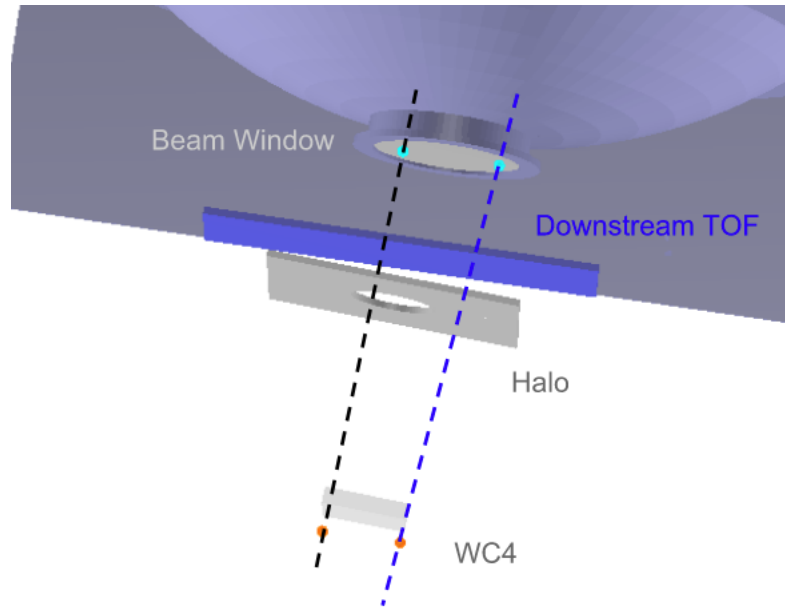


Figure 5.12: Schematic rendering of the particle path between WC4 and the TPC front face. The paddle with the hollow central circle represents the Halo paddle. We illustrate two possible trajectories: in black, a trajectory that miss the paddle and goes through the hole in the Halo, in blue a trajectory that hits the Halo paddle and goes through the scintillation material.

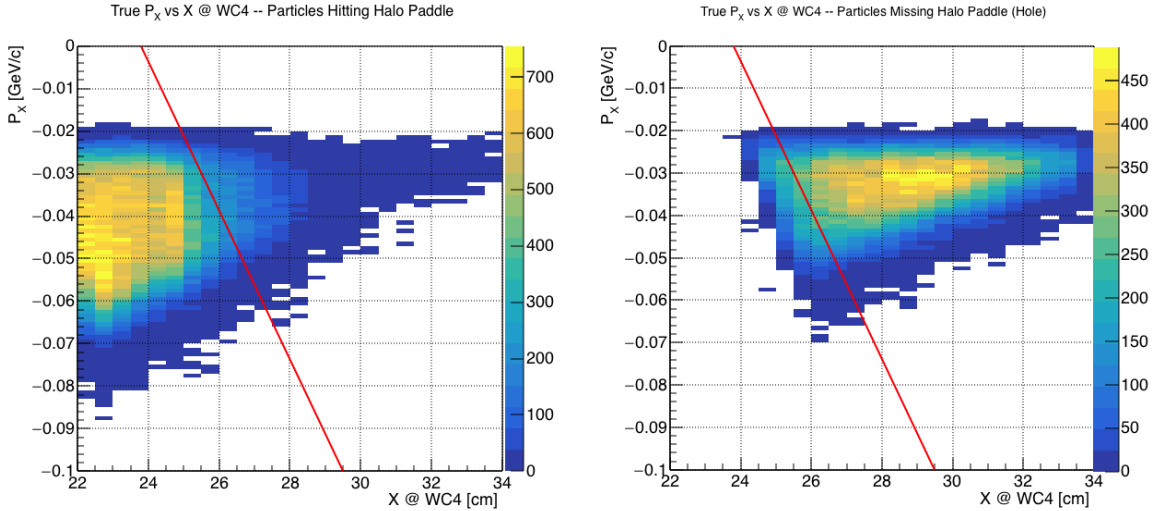


Figure 5.13: Horizontal component of the true momentum vs the horizontal position at WC4 for MC simulated pions of the 60A runs. The plot on the left shows the distribution for pion that miss the halo paddle and the plot on the right shows the distributions for pions that hit the halo. The form of the classifier is overlaid to both plots (red line).

2097 5.5 Tracking Studies

2098 The tracking of hadrons in the TPC determines both the beamline to TPC hand-
 2099 shake and the identification of the interaction point within the TPC. Thus, it plays
 2100 a fundamental role in the cross section measurements. We performed several studies
 2101 geared towards the optimization of the package for tracking in the TPC. In particular,
 2102 we studied a suitable set of parameters for the WC2TPC match and we optimized
 2103 the clustering algorithm to maximize the efficiency of finding the interaction point on
 2104 MC. Given the technical nature of these studies, we report them in Appendix A. We
 2105 report here the evaluation of the angular resolution of the tracking algorithm in data
 2106 and MC, due to its implication on the physics measurement.

2107 5.5.1 Angular Resolution

2108 Scope of this study is to understand and compare the tracking performances and
 2109 angular resolution of the TPC tracking on data and MC. We use the angular resolution

2110 of the tracking to determine the value of smallest angle that we can reconstruct with
2111 a non-zero efficiency, effectively determining a selection on the angular distribution
2112 of the cross section measurement due to the tracking performance.

2113 We start by selecting all the WC2TPC matched tracks used for the cross section
2114 analysis. These tracks can contain from a minimum of 3 3D-space points to a maxi-
2115 mum of 240 3D-space points. We fit a line to all the 3D-space points associated with
2116 the track. For each track we calculate the average distance between each point in
2117 space and the fit line as follows

$$\bar{d} = \frac{\sum_i^N d_i}{N}, \quad (5.4)$$

2118 where N is the number of 3D-space points of the track and d_i is the distance of the
2119 i -th space point to the line fit. Several tests to compare the goodness of fit between
2120 data and MC have been considered. We decided to use \bar{d} for its straightforward
2121 interpretation. The \bar{d} distribution for data and MC is shown in Figure 5.16 for pions
2122 and in Figure 5.18 for kaons and shows a relatively good agreement between data and
2123 MC.

2124 A visual representation of the procedure used to evaluate the angular resolution
2125 is shown in Figure 5.14. For each track, we order the space points according to their
2126 Z position along the positive beam direction (panel a) and we split them in two sets:
2127 the first set contains all the points belonging to the first half of the track and the
2128 second set contains all the points belonging the second half of the track. We remove
2129 the last four points in the first set and the first four points in the second set, so to
2130 have a gap in the middle of the original track (panel b). We fit the first and the second
2131 set of points with two lines (panel c). We then calculate the angle between the fit of
2132 the first and second half α (panel d). The angle α determines the spatial resolution
2133 of the tracking. The distributions for data and MC for α are given in Figure 5.17 for
2134 pions and in Figure 5.19 for kaons. The mean of the data and MC angular resolution
2135 are reported in Table tab:AngRes for pions and kaons in data and MC.

2136 Interaction angles smaller than the angle resolution are indistinguishable for the
 2137 reconstruction. Therefore, we assess our ability to measure the cross section to be
 2138 limited to interaction angles greater than 5.0 deg. More accurate studies of the angular
 2139 resolution as a function of the kinetic energy and track length, albeit interesting, are
 2140 left for an improvement of the analysis.

2141 It is beneficial to take a moment to describe the definition of interaction angle.
 2142 In case of elastic scattering, the definition is straightforward: the interaction angle is
 2143 the angle between the incoming and outgoing hadron, i.e.

$$\theta = \cos^{-1} \left(\frac{\vec{p}_{\text{incoming}} \cdot \vec{p}_{\text{outgoing}}}{|\vec{p}_{\text{incoming}}| |\vec{p}_{\text{outgoing}}|} \right). \quad (5.5)$$

2144 In case of inelastic scattering, the presence of several topologies requires a more
 2145 complex definition, as shown in figure 5.15. We define the scattering angle as the
 2146 biggest of the angles between the incoming hadron and the visible daughters, where
 2147 the visible daughters are charged particles that travel more than 0.47 cm in the
 2148 detector (see panel a); in case all the daughters are invisible, the angle is assigned
 2149 to be 90 deg (see panel b). We chose this working definition of scattering angle
 2150 for inelastic scattering keeping in mind how our tracking reconstruction works: the
 2151 tracking will stop correctly if none of the daughters are visible in the detector and it
 2152 is likely to stop correctly if multiple daughters form an interaction vertex. The only
 2153 “dangerous” case is the production of one charged daughter plus neutrals, which we
 2154 can study with this working definition of scattering angle (see panel c).

2155 We can see the effects of the angular resolution on the cross section by plotting the
 2156 true Geant4 cross section for interaction angles greater than a minimum interaction

	Data	MC
Pions	$\bar{\alpha}_{Data} = (5.0 \pm 4.5) \text{ deg}$	$\bar{\alpha}_{MC} = (4.5 \pm 3.9) \text{ deg}$
Kaons	$\bar{\alpha}_{Data} = (4.3 \pm 3.7) \text{ deg}$	$\bar{\alpha}_{MC} = (4.4 \pm 3.6) \text{ deg}$

Table 5.6: Angular resolution for Pion and Kaon tracking in both data and MC.

angle. Figure 5.20 shows the true Geant4 cross section for interaction angles greater than 0 deg (green), 4.5 deg (red), 5.0 deg (blue) and 9.0 deg (yellow). A small 0.5 deg systematic shift between the mean of the data and MC angular resolution is present.

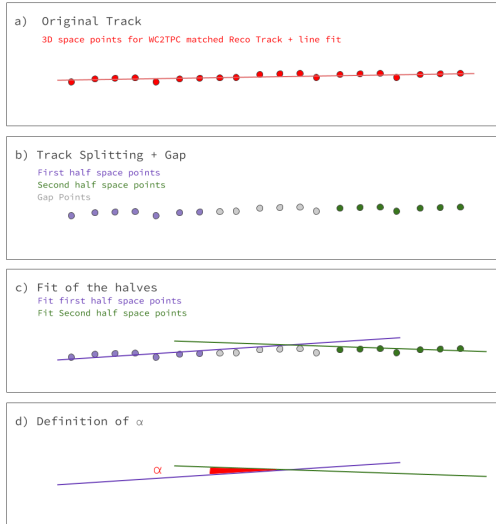


Figure 5.14: A visual representation of the procedure used to evaluate the angular resolution.

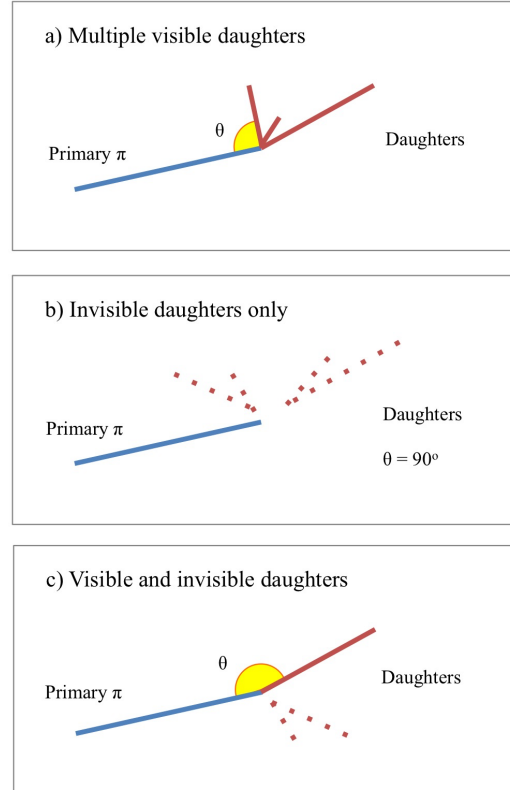


Figure 5.15: A visual representation of the scattering angle definition in case of inelastic scattering.

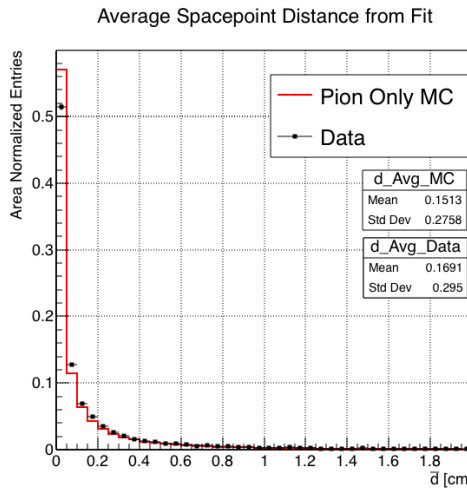


Figure 5.16: Distributions of the average distance between each 3D point in space and the fit line, \bar{d} for the data used in the pion cross section analysis and the pion only DDMC. The distributions are area normalized.

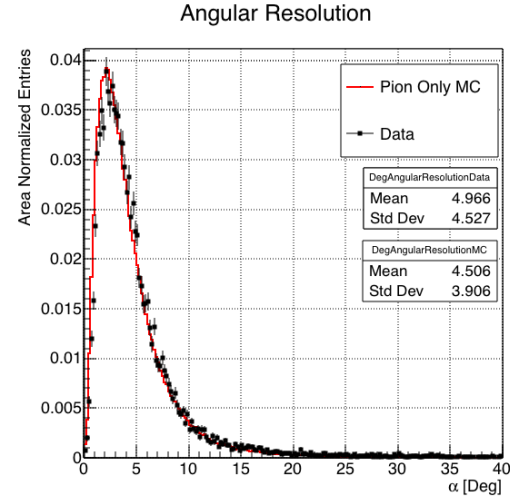


Figure 5.17: Distributions of angular resolution α for data used in the pion cross section analysis and pion only DDMC. The distributions are area normalized.

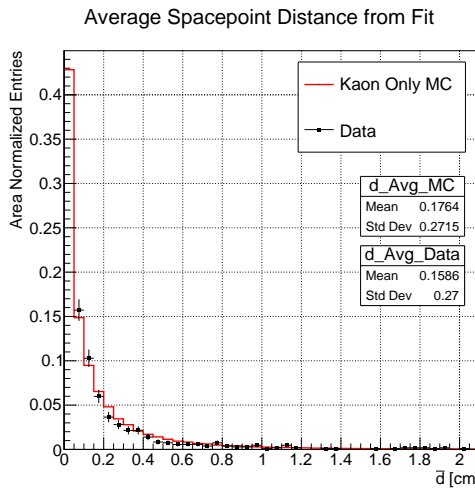


Figure 5.18: Distributions of the average distance between each 3D point in space and the fit line, \bar{d} for the data used in the kaon cross section analysis and the kaon only DDMC. The distributions are area normalized.

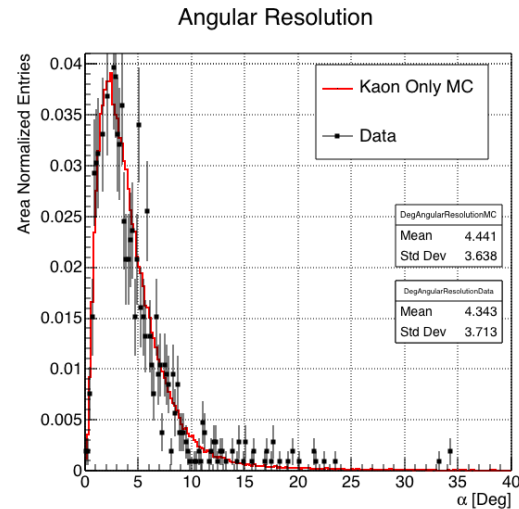


Figure 5.19: Distributions of angular resolution α for data used in the kaon cross section analysis and kaon only DDMC. The distributions are area normalized.

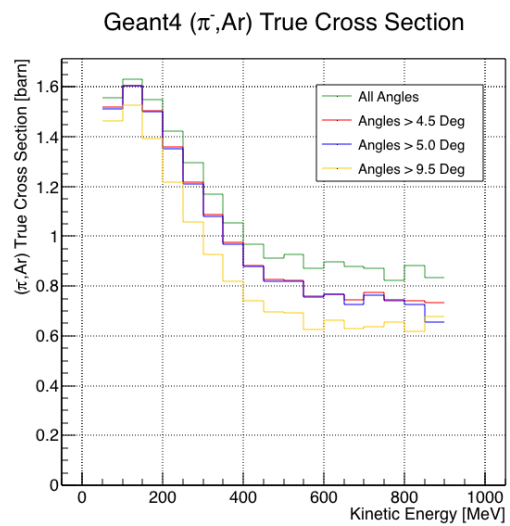


Figure 5.20: True (π^- , Ar) cross section for interaction angles greater than 0 deg (green), 4.5 deg (red), 5.0 deg (blue) and 9.0 deg (yellow).

2160 5.6 Calorimetry Studies

2161 The measured kinetic energy of a hadron candidate at each argon slab determines
2162 which bins of the interacting and incident histograms a selected event is going to fill.
2163 Thus, the energy measurement provided by the LArTPC is fundamental for the cross
2164 section analysis. In Appendix B, we describe how we calibrate the TPC calorimetric
2165 response. In the following section, we describe how we measure the kinetic energy of
2166 the hadrons in the TPC.

2167 5.6.1 Kinetic Energy Measurement

2168 In this section, we define the measurement on the kinetic energy and determine the
2169 related uncertainty. We will propagate this uncertainty into the cross section mea-
2170 surement, as discussed in Section 6.1.2 for the pion cross section and in Section ??
2171 for the kaon cross section.

2172 The kinetic energy of a hadron at the j^{th} slice of argon in the TPC is given by

$$KE_j = \sqrt{p_{\text{Beam}}^2 + m_{\text{Beam}}^2} - m_{\text{Beam}} - E_{\text{Loss}} - E_{\text{FF-j}}, \quad (5.6)$$

2173 where p_{Beam} is the momentum measured by the beamline detectors, m_{Beam} is the
2174 mass of the hadron as reported in the PDG, E_{Loss} is the energy loss between the
2175 beamline and the TPC, and $E_{\text{FF-j}}$ is the energy that the hadron deposited from the
2176 TPC front face until the j^{th} slice. The uncertainty on KE_j is then given by

$$\delta KE_j = \sqrt{\delta p_{\text{Beam}}^2 + \delta E_{\text{Loss}}^2 + \delta E_{\text{dep FF-j}}^2}, \quad (5.7)$$

2177 where we have dropped the uncertainty on the mass, since it is orders of magnitude
2178 smaller than the other uncertainties. We assume the relative uncertainty on p_{Beam} to
2179 be 2%, and the uncertainty on the energy loss upstream to be 7 MeV, as calculated

2180 in Section 5.4. We describe the estimate of the uncertainty on $E_{\text{FF-j}}$ in the rest of
2181 this section.

2182 The energy deposited by the hadron from the TPC front face until the j^{th} slice is
2183 the sum of the measured energy deposited in each previous slabs E_i , i.e.

$$E_{\text{FF-j}} = \sum_{i < j} E_i, \quad (5.8)$$

2184 where E_i is measured in each slab as the product of the stopping power, dE/dX_i ,
2185 and the track pitch, Pitch_i , for that point. If we assume conservatively that the
2186 measurements of E_i are not independent from one another, the uncertainty on $E_{\text{FF-j}}$
2187 becomes

$$\delta E_{\text{FF-j}} = (j - 1)\delta E_i, \quad (5.9)$$

2188 where δE_i is the uncertainty on the energy loss in one slab of argon.

2189 The left side of Figure 5.21 shows the distribution of the energy deposited in each
2190 slab of argon, for the 60A negative pion dataset in black and for the pion only MC
2191 in blue. The analogous plot for the -100A negative pion data set is show on the right
2192 side of Figure 5.21. The distributions are fitted with a landau displayed in red for
2193 data and in teal for MC. The uncertainty on E_i is given by the width of the Landau
2194 fit to the data. A small systematic uncertainty is given by a 1.0% difference between
2195 the most probable value of the landau fits in data and MC.

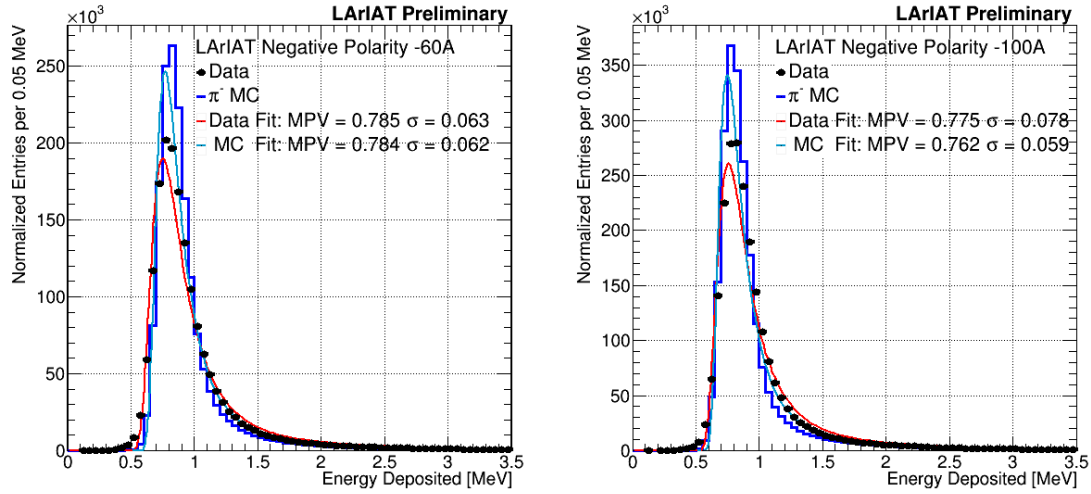


Figure 5.21: Energy deposited E_i in a single slab of argon for the pion -60A runs (left) and -100A runs (right). The data is shown in black, the MC in blue. The distributions are fitted with a landau displayed in red for data and in teal for MC.

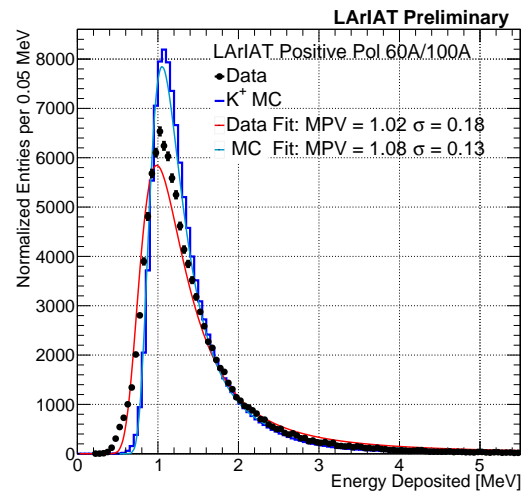


Figure 5.22: Energy deposited E_i in a single slab of argon for the kaons of the +60A runs and +100A runs. The data is shown in black, the MC in blue. The distributions are fitted with a landau displayed in red for data and in teal for MC.

2196 **Chapter 6**

2197 **Negative Pion Cross Section**

2198 **Measurement**

2199 “*Y ella es flama que se eleva, Y es un pájaro a volar.*
2200 *En la noche que se incendia, estrella de oscuridad*
2201 *que busca entre la tiniebla, la dulce hoguera del beso.*”
2202 – Lila Downs, Benediction And Dream, 2002 –

2203 In this chapter, we show the result of the thin slice method to measure the (π^- -
2204 Ar) total hadronic cross section. In Section 6.1, we start by measuring the raw
2205 cross section, i.e. the cross section obtained exclusively using data reconstruction,
2206 without any additional corrections. In Section 6.2, we apply a statistical subtraction
2207 of the background contributions based on simulation and a correction for detection
2208 inefficiency. The final results are presented in Section 6.3.

2209 **6.1 Raw Cross Section**

2210 We measure the raw (π^- -Ar) total hadronic cross section as a function of the kinetic
2211 energy in the two chosen data sets, the -60A and -100A negative runs. As we will

clarify in Section 6.2, the corrections to the raw cross section depend on the beam conditions and need to be calculated independently for the two datasets. Thus, we present here the measurement of the raw cross section on the two datasets separately.

As stated in section 4.3.2, the raw cross section is given by the equation 4.4

$$\sigma_{TOT}(E_i) = \frac{1}{n\delta X} \frac{N_{Int}^{TOT}(E_i)}{N_{Inc}^{TOT}(E_i)}, \quad (6.1)$$

where N_{Int}^{TOT} is the measured number of particles interacting at kinetic energy E_i , N_{Inc}^{TOT} is the measured number of particles incident on an argon slice at kinetic energy E_i , n is the density of the target centers and δX is the thickness of the argon slice. The density of the target centers and the slab thickness are $n = 0.021 \cdot 10^{24} \text{ cm}^{-3}$ and $\delta X = 0.47 \text{ cm}$, respectively.

Figure 6.1 shows the distribution of N_{Int}^{TOT} as a function of the kinetic energy for the 60A dataset on the left and for the 100A dataset on the right. The data central points are represented by black dots, the statistical uncertainty is shown in black, while the systematic uncertainty is shown in red. Data is displayed over the N_{Int}^{TOT} distribution obtained with a MC mixed sample of pions, muon and electrons (additional details on the composition will be provided in Section ??). The contribution from the simulated pions is shown in blue, the one from secondaries in red, the one from muons in yellow and the ones from electrons in gray. The simulated pion's and backgrounds' contributions are stacked; the sum of the integrals from each particle species is normalized to the integral of the data.

Figure 6.2 shows the distribution of N_{Inc}^{TOT} for the 60A dataset on the left and for the 100A dataset on the right. Data is displayed over the MC. The same color scheme and normalization procedure is used for both the interacting and incident histograms.

Figure 6.3 shows the raw cross section for the 60A dataset on the left and for the 100A dataset on the right, statistical uncertainty in black and systematic uncertainty

2236 in red. The raw data cross section is overlaid to the reconstructed cross section for
 2237 the MC mixed sample, displayed in azure. Since the background contributions and
 2238 the detector effects for the 60A and 100A sample are different, it is premature to
 2239 compare the raw cross sections obtained from the two samples at this point.

2240 We describe the calculation of the statistical uncertainty for the interacting, in-
 2241 cident and cross section distributions in Section 6.1.1; we describe the procedure to
 2242 calculate the corresponding systematics uncertainty on Section 6.1.2.

2243 6.1.1 Statistical Uncertainty

2244 The statistical uncertainty for a given kinetic energy bin of the cross section is cal-
 2245 culated by error propagation from the statistical uncertainty on $N_{\text{Inc}}^{\text{TOT}}$ and $N_{\text{Int}}^{\text{TOT}}$
 2246 correspondent bin. Since the number of incident particles in each energy bin is given
 2247 by a simple counting, we assume that $N_{\text{Inc}}^{\text{TOT}}$ is distributed as a poissonian with mean
 2248 and variance equal to $N_{\text{Inc}}^{\text{TOT}}$ in each bin. On the other hand, $N_{\text{Int}}^{\text{TOT}}$ follows a bino-
 2249 mial distribution: a particle in a given energy bin might or might not interact. The
 2250 variance for the binomial is given by

$$\text{Var}[N_{\text{Int}}^{\text{TOT}}] = \mathcal{N}P_{\text{Interacting}}(1 - P_{\text{Interacting}}). \quad (6.2)$$

2251 Since the interaction probability $P_{\text{Interacting}}$ is $\frac{N_{\text{Int}}^{\text{TOT}}}{N_{\text{Inc}}^{\text{TOT}}}$ and the number of tries \mathcal{N} is
 2252 $N_{\text{Inc}}^{\text{TOT}}$, equation 6.2 translates into

$$\text{Var}[N_{\text{Int}}^{\text{TOT}}] = N_{\text{Inc}}^{\text{TOT}} \frac{N_{\text{Int}}^{\text{TOT}}}{N_{\text{Inc}}^{\text{TOT}}} \left(1 - \frac{N_{\text{Int}}^{\text{TOT}}}{N_{\text{Inc}}^{\text{TOT}}}\right) = N_{\text{Int}}^{\text{TOT}} \left(1 - \frac{N_{\text{Int}}^{\text{TOT}}}{N_{\text{Inc}}^{\text{TOT}}}\right). \quad (6.3)$$

2253 $N_{\text{Inc}}^{\text{TOT}}$ and $N_{\text{Int}}^{\text{TOT}}$ are not independent. The statistical uncertainty on the cross
 2254 section is thus calculated as

$$\delta\sigma_{\text{TOT}}(E) = \sigma_{\text{TOT}}(E) \left(\frac{\delta N_{\text{Int}}^{\text{TOT}}}{N_{\text{Int}}^{\text{TOT}}} + \frac{\delta N_{\text{Inc}}^{\text{TOT}}}{N_{\text{Inc}}^{\text{TOT}}} \right) \quad (6.4)$$

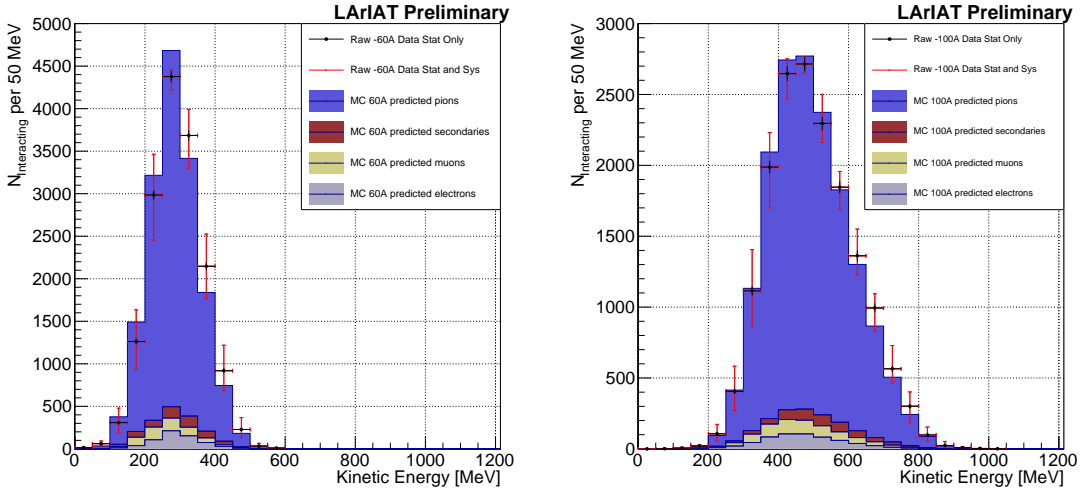


Figure 6.1: Raw number of interacting pion candidates as a function of the reconstructed kinetic energy for the 60A runs (left) and for the 100A runs (right). The statistical uncertainties are shown in black, the systematic uncertainties in red.

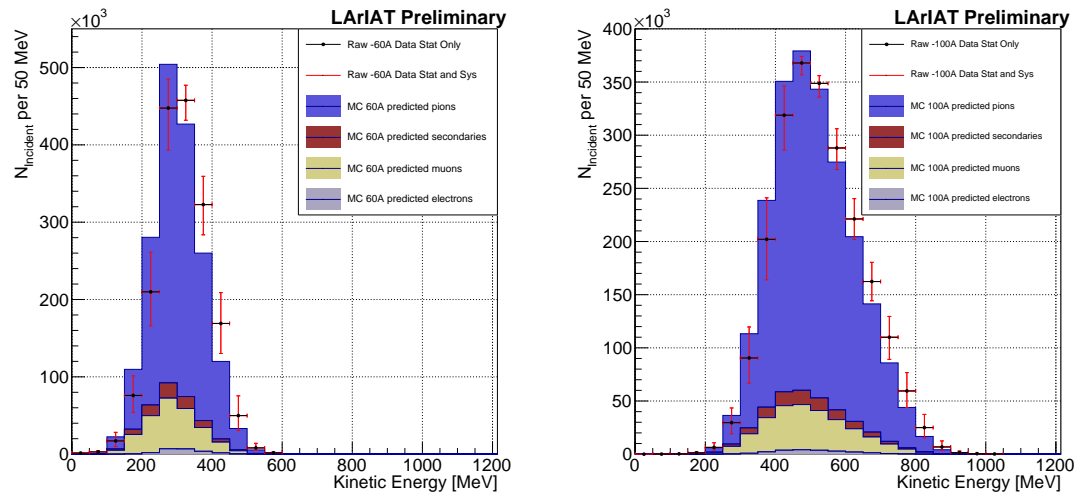


Figure 6.2: Raw number of incident pion candidates as a function of the reconstructed kinetic energy for the 60A runs (left) and for the 100A runs (right). The statistical uncertainty is shown in black, the systematic uncertainties in red.

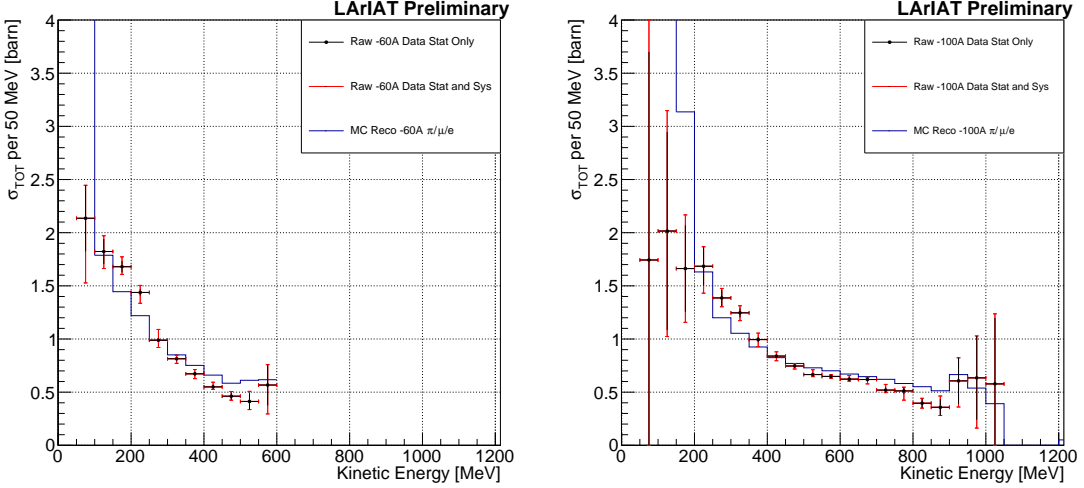


Figure 6.3: Raw (π^- -Ar) total hadronic cross section for the 60A runs (left) and for the 100A runs (right). The statistical uncertainty is shown in black, the systematic uncertainties in red. The raw cross section obtained with a MC mixed sample of pions, muon and electrons in the percentage predicted by G4Beamline is shown in azure.

2255 where:

$$\delta N_{\text{Inc}}^{\text{TOT}} = \sqrt{N_{\text{Inc}}^{\text{TOT}}} \quad (6.5)$$

$$\delta N_{\text{Int}}^{\text{TOT}} = \sqrt{N_{\text{Int}}^{\text{TOT}} \left(1 - \frac{N_{\text{Int}}^{\text{TOT}}}{N_{\text{Inc}}^{\text{TOT}}}\right)}. \quad (6.6)$$

2256 6.1.2 Treatment of Systematics

2257 The only systematic effect considered in the measurement of the raw cross section
 2258 results from the propagation of the uncertainty associate with the measurement of
 2259 the kinetic energy at each argon slab. As shown in Section 5.6.1, the uncertainty on
 2260 the kinetic energy of a pion candidate at the j^{th} slab of argon is given by

$$\delta KE_j = \sqrt{\delta p_{\text{Beam}}^2 + \delta E_{\text{Loss}}^2 + \delta E_{\text{dep FF-j}}^2} \quad (6.7)$$

$$= \sqrt{(2\% p_{\text{Beam}})^2 + (6 \text{ [MeV]})^2 + (j - 1)^2 (\sim 0.08 \text{ [MeV]})^2}. \quad (6.8)$$

2261 We propagate this uncertainty by varying the energy measurement KE_j at each
 2262 argon slab. We measure $N_{\text{Inc}}^{\text{TOT}}$, $N_{\text{Int}}^{\text{TOT}}$ and the cross section in three cases: first
 2263 assigning the measured KE_j at each kinetic energy sampling, then assigning $KE_j +$
 2264 δKE_j , and finally assigning $KE_j - \delta KE_j$. The difference between the values obtained
 2265 using the KE_j sampling and the maximum and minimum values in each kinetic energy
 2266 bin determines the systematic uncertainty.

2267 **6.2 Corrections to the Raw Cross Section**

2268 As described in section 4.3.3, we need to apply a background correction and an
 2269 efficiency correction in order to derive the true pion cross section from the raw cross
 2270 section. The true cross section is given in equation 4.9,

$$\sigma_{\text{TOT}}^{\pi^-}(E_i) = \frac{1}{n\delta X} \frac{\epsilon^{\text{Inc}}(E_i)}{\epsilon^{\text{Int}}(E_i)} \frac{C_{\text{Int}}^{\pi MC}(E_i)}{C_{\text{Inc}}^{\pi MC}(E_i)} \frac{N_{\text{Int}}^{\text{TOT}}(E_i)}{N_{\text{Inc}}^{\text{TOT}}(E_i)}. \quad (4.9)$$

2271 Section 6.2.1 describes the evaluation of pion content in the interacting and inci-
 2272 dent histograms, ($C_{\text{Int}}^{\pi MC}(E_i)$ and $C_{\text{Inc}}^{\pi MC}(E_i)$) and the propagation to the cross section
 2273 measurement of the relative systematic uncertainties.

2274 Section 6.2.2 describes the procedure employed to obtain the efficiency corrections
 2275 $\epsilon^{\text{Int}}(E_i)$ and $\epsilon^{\text{Inc}}(E_i)$ and the propagation to the cross section measurement of the
 2276 relative uncertainties.

2277 **6.2.1 Background subtraction**

2278 We use the procedure described in 5.3.2 to evaluate the relative pion content in
 2279 the interacting histogram $C_{\text{Int}}^{\pi MC}(E_i)$ and the relative pion content in the incident
 2280 $C_{\text{Inc}}^{\pi MC}(E_i)$. We start by evaluating the relative pion content assuming the beamline
 2281 composition simulated by G4Beamline, whose pion, muon and electron percentages
 2282 per beam condition are reported again in the first line of Table 6.1. The left side of

2283 Figure 6.4 shows the MC estimated relative pion content for the interacting histogram
2284 as function of kinetic energy for the 60A runs (top) and 100A runs (bottom). The
2285 right side of the same figure shows the MC estimated relative pion content for the
2286 incident histogram as function of kinetic energy for the 60A runs (top) and 100A
2287 runs (bottom). In Figure 6.4 the central curves displayed in light blue are obtained
2288 using the beamline composition as predicted by G4Beamline: these are the correction
2289 curves for the relative pion content applied to data.

2290 So, the question now becomes: how well do we know the beamline composition?
2291 In absence of additional data constraints, we take a 100% systematic uncertainty on
2292 the electron content, reported in lines 3 and 4 of Table 6.1. The effect of doubling or
2293 halving the electron percentage in the beam on the pion relative content is displayed
2294 in red in Figure 6.4. We reserve a slightly different treatment for the muon content.
2295 Since G4Beamline tracks only particles which cross all the wire chambers, pion events
2296 that decay in flight from WC1 to WC4 are not recorded by G4Beamline. Pion decays
2297 in the beamline could be trigger the beamline detectors in data, if the produced muon
2298 proceeds in the beamline. Thus, we take the G4Beamline prediction for muons as a
2299 lower bound in the composition: the effect of doubling the muon content (line 2 in
2300 Table 6.1) is shown in blue on Figure 6.4. A future study of data from additional
2301 beamline detectors such as the Aerogel Chernkov detectors [42] or the muon range
2302 stack (see Section 3.2.4) has the potential of a narrowing the systematics uncertainty
2303 coming from the beamline composition.

2304 We propagate the uncertainty on the beamline composition as a systematic un-
2305 certainty to the cross section by varying the beam composition for all the cases listed
2306 in Table 6.1 and evaluating variation of obtained data cross sections in each bin. This
2307 systematic uncertainty is summed in quadrature with the statistical uncertainty and
2308 the systematic uncertainty related to the kinetic energy measurement.

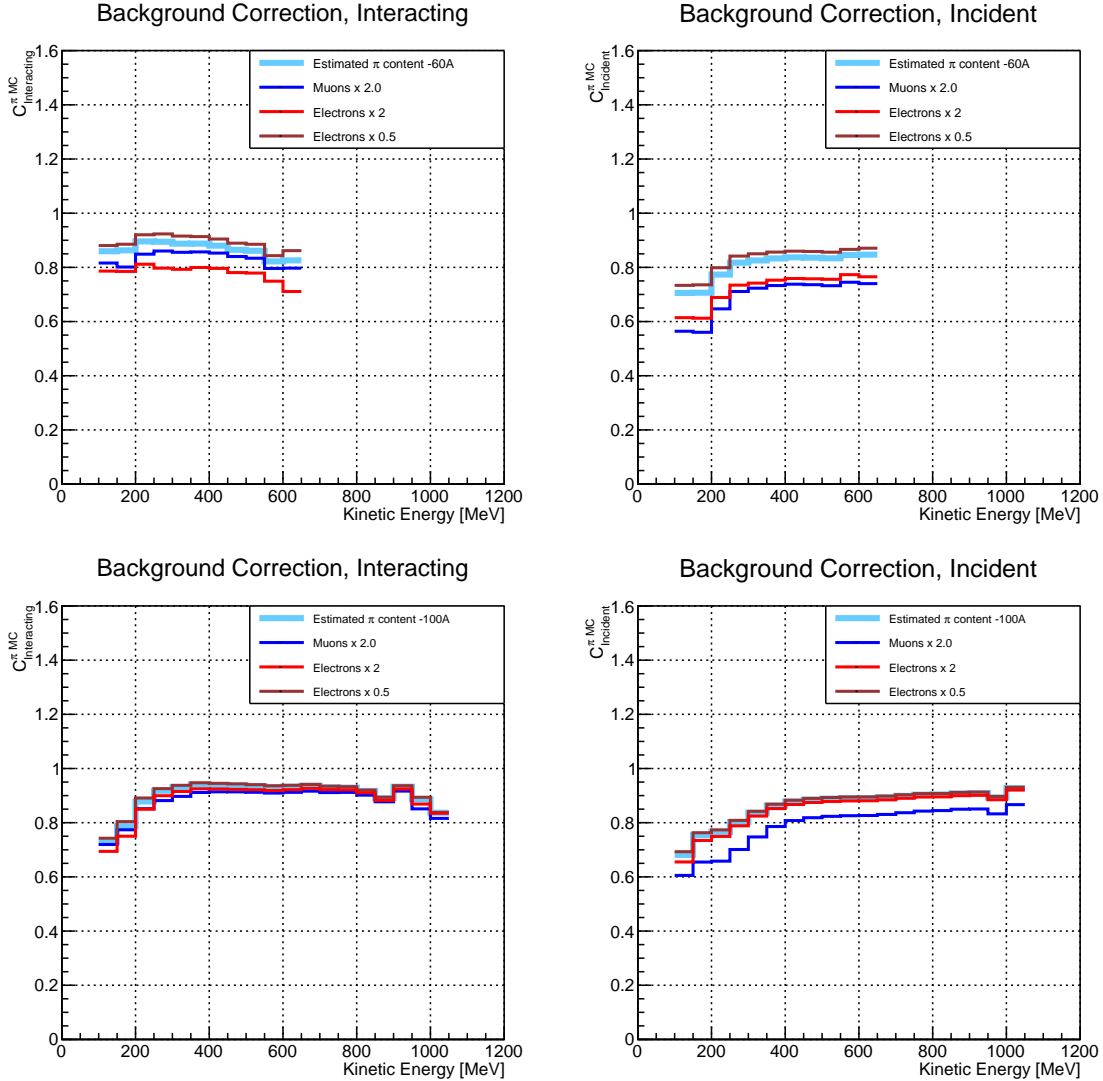


Figure 6.4: *Left:* MC estimated relative pion content for interacting histogram a function of kinetic energy for the 60A runs (top) and 100A runs (bottom), predicted background content in azure and muon and electron content variation in blue and red. *Right:* MC estimated relative pion content for incident histogram a function of kinetic energy for the 60A runs (top) and 100A (bottom), predicted background content in azure and muon and electron content variation in blue and red

2309 **6.2.2 Efficiency Correction**

2310 The interaction point for a track used in the total hadronic cross section analysis
2311 is defined to be the last point of the WC2TPC matched track which lies inside the
2312 fiducial volume. This definition is independent from the topology of the interaction.
2313 If the TPC track stops within the fiducial volume, its last point will be the interaction
2314 point, no matter what the products of the interaction look like; if the track crosses the
2315 boundaries of the fiducial volume, the track will be considered “through going” and no
2316 interaction point will be found. Given this definition, it is evident that we rely on the
2317 tracking algorithm to discern where the interaction occurred in the TPC and correctly
2318 stop the tracking. The tracking algorithm has an intrinsic angle resolution as shown
2319 in section 5.5.1, which limits its efficiency, especially in the case of elastic scattering
2320 occurring at low angles. Thus, we need to apply an efficiency correction to data in order
2321 to retrieve the true cross section. The efficiency correction is evaluated separately for
2322 the interacting and incident histograms, namely ϵ_i^{int} and ϵ_i^{inc} , and propagated to the
2323 cross section as shown in equation 4.9.

2324 **Efficiency Correction: Procedure**

2325 We describe here the procedure to calculate the efficiency correction taking the in-
2326 teracting histogram as example and noting that the procedure is identical for the
2327 incident histogram.

2328 We derive the correction on a set of pure pion MC, calculating its value bin by
2329 bin as the ratio between the true bin content and the correspondent reconstructed
2330 bin content. The correction is then applied to the relevant bin in data. In formulae,
2331 the efficiency correction is calculated to be

$$\epsilon^{\text{Int}}(E_i) = \frac{N_{\text{Interacting}}^{\pi \text{ Reco MC}}(E_i)}{N_{\text{Interacting}}^{\pi \text{ True MC}}(E_i)}, \quad (6.9)$$

2332 where $N_{\text{Int}}^{\pi \text{ True MC}}(E_i)$ is the content of the i -th bin in for the true interacting
 2333 histogram, and $N_{\text{Int}}^{\pi \text{ Reco MC}}(E_i)$ is the content of the i -th bin in for the reconstructed
 2334 interacting histogram. The correction is applied to data as follows

$$N_{\text{Int}}^{\pi \text{ True Data}}(E_i) = \frac{N_{\text{Int}}^{\pi \text{ Reco Data}}(E_i)}{\epsilon^{\text{Int}}(E_i)} = N_{\text{Int}}^{\pi \text{ Reco Data}}(E_i) \frac{N_{\text{Int}}^{\pi \text{ True MC}}(E_i)}{N_{\text{Int}}^{\pi \text{ Reco MC}}(E_i)}. \quad (6.10)$$

2335 where $N_{\text{Int}}^{\pi \text{ Reco Data}}(E_i)$ is the background subtracted bin content of the i -th bin in
 2336 for the reconstructed interacting histogram for data, i.e.

$$N_{\text{Int}}^{\pi \text{ Reco Data}}(E_i) = N_{\text{Int}}^{\text{TOT Data}}(E_i) - B_{\text{Int}}^{\text{Data}}(E_i) = C_{\text{Int}}^{\pi \text{ MC}}(E_i) N_{\text{Int}}^{\text{TOT Data}}(E_i). \quad (6.11)$$

2337 In section 5.5.1, we estimated the angular resolution for data and MC to be
 2338 $\bar{\alpha}_{\text{Data}} = (5.0 \pm 4.5)$ deg and $\bar{\alpha}_{\text{MC}} = (4.5 \pm 3.9)$ deg, respectively. Most interaction
 2339 angles smaller than the angular resolution will thus be indistinguishable for the re-
 2340 construction. Thus, we claim we are able to measure the cross section for interaction
 2341 angles greater than 5.0 deg. Geant4 simulates interactions at all angles, as shown in
 2342 figure 6.7. In order to calculate the efficiency correction, we select events which have
 2343 an interaction angle greater than a given α_{res} to construct the true interacting and
 2344 incident histograms (the denominator of the efficiency correction). The systematics
 2345 on the efficiency correction is estimated by varying the value of α_{res} between 0 deg
 2346 and 4.5 deg and propagating the uncertainty on the cross section.

2347 Figure 6.5 shows $\epsilon^{\text{Int}}(E_i)$ in the left side and $\epsilon^{\text{Inc}}(E_i)$ on the right as a function of
 2348 the kinetic energy for the 60A runs and their systematic uncertainty. Similarly, figure
 2349 6.6 shows $\epsilon^{\text{Int}}(E_i)$ in the left side and $\epsilon^{\text{Inc}}(E_i)$ on the right as a function of the kinetic
 2350 energy for the 100A runs and their systematic uncertainty.

	Magnet Current -60A			Magnet Current -100 A		
	MC π^-	MC μ^-	MC e^-	MC π^-	MC μ^-	MC e^-
Expected Composition	68.8 %	4.6 %	26.6 %	87.4 %	3.7 %	8.9 %
Composition 2x Muons	64.2 %	9.2 %	26.6 %	83.7 %	7.4 %	8.9 %
Composition 2x Electrons	42.2 %	4.6 %	53.2 %	78.5 %	3.7 %	17.8 %
Composition 0.5x Electrons	82.1 %	4.6 %	13.3 %	91.9 %	3.7 %	4.4 %

Table 6.1: Beam composition variation for the study of systematics due to beam contamination.

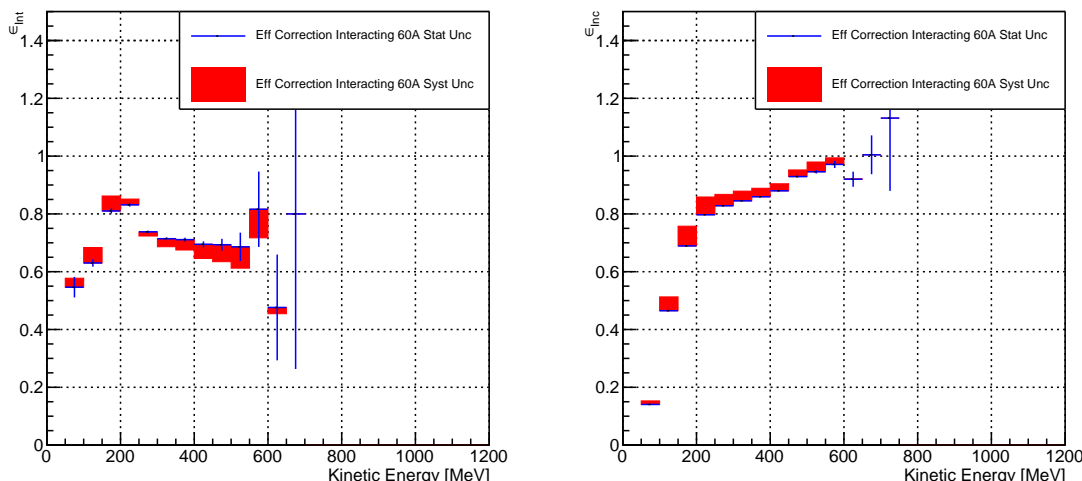


Figure 6.5: *Left:* Efficiency correction on the 60A interacting histogram, statistical uncertainty in blue, systematic uncertainty in red. *Right:* Efficiency correction on the 60A incident histogram, statistical uncertainty in blue, systematic uncertainty in red.

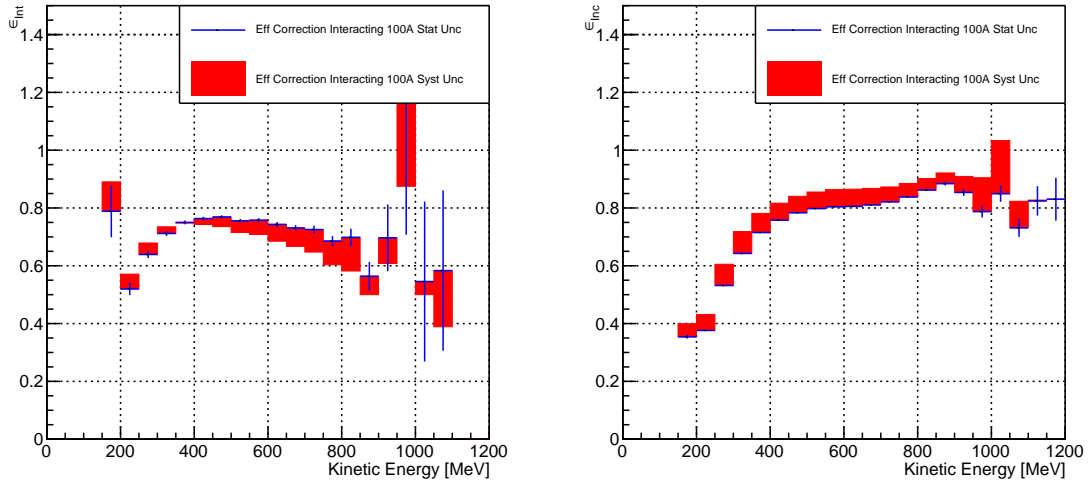


Figure 6.6: *Left*: Efficiency correction on the 100A interacting histogram, statistical uncertainty in blue, systematic uncertainty in red. *Right*: Efficiency correction on the 100A incident histogram, statistical uncertainty in blue, systematic uncertainty in red.

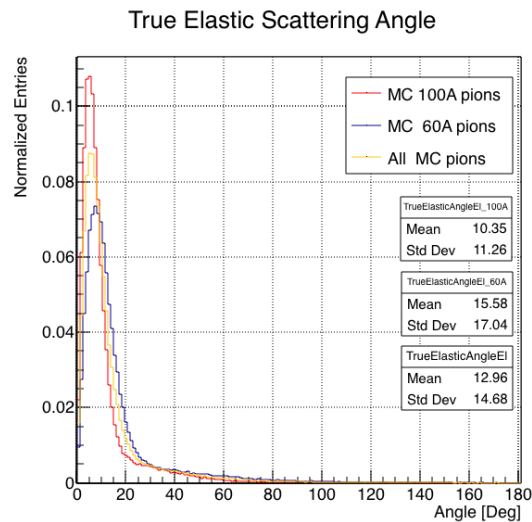


Figure 6.7: Distribution of the true scattering angle for a pion elastic scattering off the argon nucleus as simulated by Geant4.

2351 **6.3 Results**

2352 Figure 6.8 show the measurement of the (π^- -Ar) total hadronic cross section for
2353 scattering angles greater than 5° , as the result of the background subtraction and
2354 efficiency correction to the raw cross section. The top left plot is the measurement
2355 obtained on the 60A data, statistical uncertainty in black and systematic uncertainty
2356 in red. The top right plot is the measurement obtained on the 100A data, statistical
2357 uncertainty in black and systematic uncertainty in blue. The bottom plot shows the
2358 two measurements overlaid. In all three plot, the Geant4 prediction for the total
2359 hadronic cross section for angle scattering greater than 5° is displayed in green.

2360 The systematic uncertainty on the cross section is the sum in quadrature of the
2361 statistical uncertainty, the systematic uncertainty related to the kinetic energy mea-
2362 surement, the systematic uncertainty related to the beam composition and the sys-
2363 tematic uncertainty related to the efficiency correction.

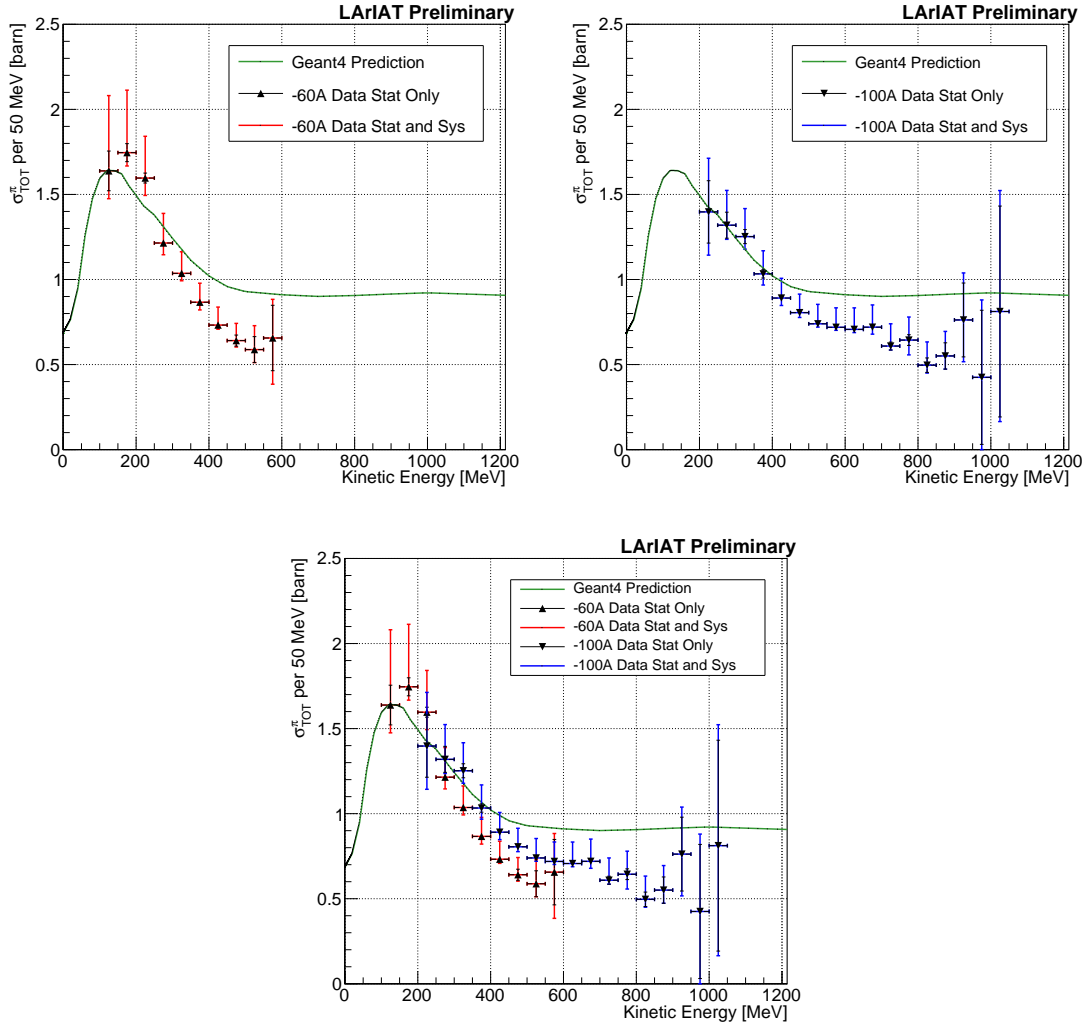


Figure 6.8: *Top Left:* (π^- -Ar) total hadronic cross section for scattering angles greater than 5° measured in the 60A sample, statistical uncertainty in black and systematic uncertainty in red. The Geant4 prediction for the total hadronic cross section for angle scattering greater than 5° is displayed in green.

Top Right: (π^- -Ar) total hadronic cross section for scattering angles greater than 5° measured in the 100A sample, statistical uncertainty in black and systematic uncertainty in blue. The Geant4 prediction for the total hadronic cross section for angle scattering greater than 5° is displayed in green.

Bottom: (π^- -Ar) total hadronic cross section measurements in the 60A and 100A samples overlaid with the Geant4 prediction (green).

2364 **Chapter 7**

2365 **Positive Kaon Cross Section**

2366 **Measurement**

2367 “Beat-up little seagull, on a marble stair
2368 Tryin’ to find the ocean, lookin’ everywhere.”
2369 – Nina Simone, Baltimore, 1978 –

2370 In this chapter, we show the result of the thin slice method to measure the (K^+ -
2371 Ar) total hadronic cross section. In Section 7.1, we start by measuring the raw
2372 cross section. In Section 7.2, we apply a statistical subtraction of the background
2373 contributions based on simulation and a correction for detection inefficiency. The
2374 final results are presented in Section 7.3.

2375 **7.1 Raw Cross Section**

2376 We measure the raw (K^+ -Ar) total hadronic cross section as a function of the kinetic
2377 energy in the combined +60A and +100A dataset.

2378 Similar to the pion case, the raw cross section is given by the equation 4.4

$$\sigma_{TOT}(E_i) = \frac{1}{n\delta X} \frac{N_{Int}^{TOT}(E_i)}{N_{Inc}^{TOT}(E_i)}, \quad (7.1)$$

2379 where N_{Int}^{TOT} is the measured number of particles interacting at kinetic energy E_i ,
2380 N_{Inc}^{TOT} is the measured number of particles incident on an argon slice at kinetic energy
2381 E_i , n is the density of the target centers and δX is the thickness of the argon slice.
2382 The density of the target centers and the slab thickness are $n = 0.021 \cdot 10^{24} \text{ cm}^{-3}$ and
2383 $\delta X = 0.47 \text{ cm}$, respectively.

2384 As in the case of pions, kaons might decay or interact between WC4 and the TPC
2385 front face. Some of the interaction products may be wrongly matched to the WC
2386 track, forming the “secondary” particle’s background in the kaon sample. We estimate
2387 the effect of the contamination of secondaries through the DDMC kaon sample. Figure
2388 7.1 shows the distribution of N_{Int}^{TOT} as a function of the kinetic energy. The data
2389 central points are represented by black dots, the statistical uncertainty is shown in
2390 black, while the systematic uncertainty is shown in red. Data is displayed over the
2391 N_{Int}^{TOT} distribution obtained with a DDMC sample of kaons shot from WC4. The
2392 contribution from the simulated kaons which interact hadronically is shown in pink,
2393 the contributions from kaon decay is shown in orange and the one from secondaries
2394 in red. The simulated kaon’s and secondaries’ contributions are stacked; the sum of
2395 their integrals is normalized to the integral of the data.

2396 Figure 7.2 shows the distribution of N_{Inc}^{TOT} . Data is displayed over the MC. For the
2397 N_{Inc}^{TOT} distribution we do not make a distinction between kaons that decay or interact
2398 hadronically because any kaon independently from its final interaction contributes
2399 to the flux of incident particles at given kinetic energy. The same normalization
2400 procedure is used for both the interacting and incident histograms.

2401 Figure 7.3 shows the raw cross section, statistical uncertainty in black and system-

atic uncertainty in red. The raw data cross section is overlaid to the reconstructed cross section for the MC mixed sample, displayed in azure. We calculate the statistical uncertainty for the interacting, incident and cross section distributions in a similar fashion to the pion case as described in Section 6.1.1.

As in the pion case, the only systematic effect considered in the measurement of the raw cross section results from the propagation of the uncertainty associate with the measurement of the kinetic energy at each argon slab. For kaons, the uncertainty on the kinetic energy of a candidate at the j^{th} slab of argon is given by

$$\delta KE_j = \sqrt{\delta p_{Beam}^2 + \delta E_{Loss}^2 + \delta E_{dep\ FF-j}^2} \quad (7.2)$$

$$= \sqrt{(2\% p_{Beam})^2 + (7\text{ [MeV]})^2 + (j - 1)^2(\sim 0.18\text{ [MeV]})^2}. \quad (7.3)$$

We propagate this uncertainty by varying the energy measurement KE_j at each argon slab. We measure N_{Inc}^{TOT} , N_{Int}^{TOT} and the cross section in three cases: first assigning the measured KE_j at each kinetic energy sampling, then assigning $KE_j + \delta KE_j$, and finally assigning $KE_j - \delta KE_j$. The difference between the values obtained using the KE_j sampling and the maximum and minimum values in each kinetic energy bin determines the systematic uncertainty.

7.2 Corrections to the Raw Cross Section

As described in section 4.3.3, we need to apply a background correction and an efficiency correction in order to derive the true Kaon cross section from the raw cross section. The true cross section is given in equation 4.9,

$$\sigma_{TOT}^{K^+}(E_i) = \frac{1}{n\delta X} \frac{\epsilon^{Inc}(E_i)}{\epsilon^{Int}(E_i)} \frac{C_{Int}^{KMC}(E_i)}{C_{Inc}^{KMC}(E_i)} \frac{N_{Int}^{TOT}(E_i)}{N_{Inc}^{TOT}(E_i)}. \quad (4.9)$$

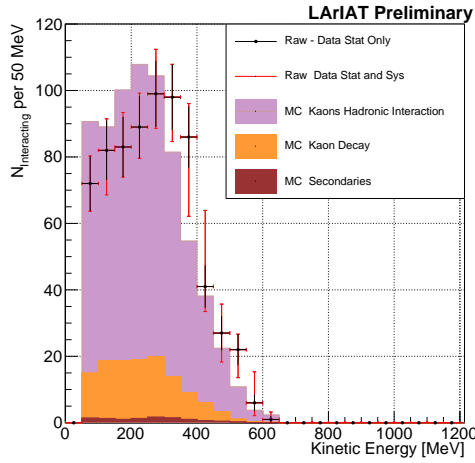


Figure 7.1: Raw number of interacting kaon candidates as a function of the reconstructed kinetic energy. The statistical uncertainties are shown in black, the systematic uncertainties in red.

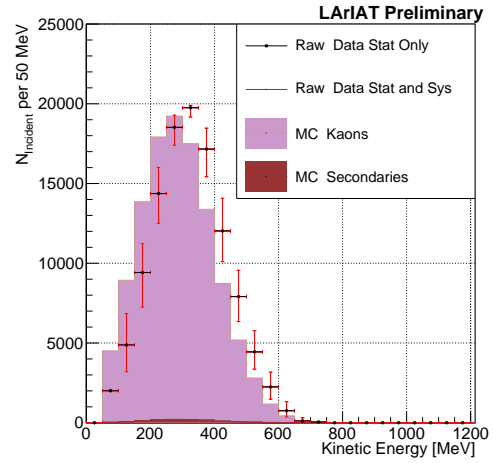


Figure 7.2: Raw number of incident kaon candidates as a function of the reconstructed kinetic energy. The statistical uncertainty is shown in black, the systematic uncertainties in red.

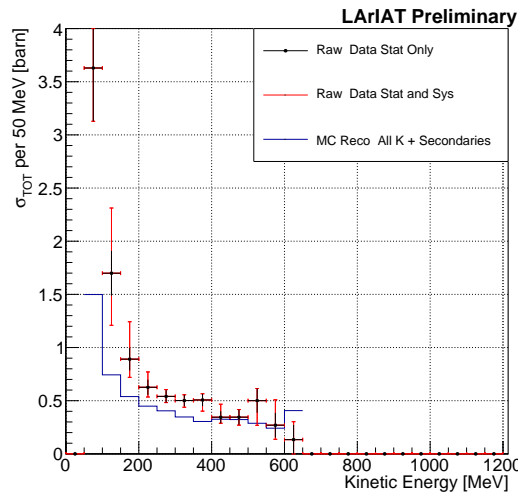


Figure 7.3: Raw (K^+ -Ar) total hadronic cross section. The statistical uncertainty is shown in black, the systematic uncertainties in red. The raw cross section obtained with a MC sample of kaons is shown in blue. For the MC cross section, we include the contributions from secondaries.

2420 Currently, the only background considered for the kaon hadronic cross section
2421 comes from the presence of secondaries. A further development of the analysis will
2422 need to account for the presence of a small proton contamination. Figure 7.4 shows
2423 the relative kaon content for the interacting and incident histograms.

2424 As described in 6.2.2 for the pion case, we derive the correction on a set of pure
2425 kaon MC, calculating its value bin by bin as the ratio between the true bin content
2426 and the correspondent reconstructed bin content. The correction is then applied to
2427 the relevant bin in data. The efficiency correction is evaluated separately for the
2428 interacting and incident histograms, namely ϵ_i^{int} and ϵ_i^{inc} , and propagated to the cross
2429 section as shown in equation 4.9.

2430 In section 5.5.1, we estimated the angular resolution for data and MC to be
2431 $\bar{\alpha}_{\text{Data}} = (4.3 \pm 3.7)$ deg and $\bar{\alpha}_{\text{MC}} = (4.4 \pm 3.6)$ deg, respectively. Most interaction
2432 angles smaller than the angular resolution will thus be indistinguishable for the re-
2433 construction. Thus, we claim we are able to measure the cross section for interaction
2434 angles greater than 4.5 deg. Geant4 simulates interactions at all angles: in order to
2435 calculate the efficiency correction, we select events which have an interaction angle
2436 greater than a α_{res} to construct the true interacting and incident histograms (the de-
2437 nominator of the efficiency correction). The systematics on the efficiency correction
2438 is estimated by varying the value of α_{res} between 0 deg and 4.5 deg and propagating
2439 the uncertainty on the cross section.

2440 Figure 7.5 shows $\epsilon^{\text{Int}}(E_i)$ in the left side and $\epsilon^{\text{Inc}}(E_i)$ on the right as a function of
2441 the kinetic energy for the kaon sample and their systematic uncertainty.

2442 7.3 Results

2443 Figure 7.6 show the measurement of the (K^+ -Ar) total hadronic cross section for
2444 scattering angles greater than 5° , as the result of the background subtraction and

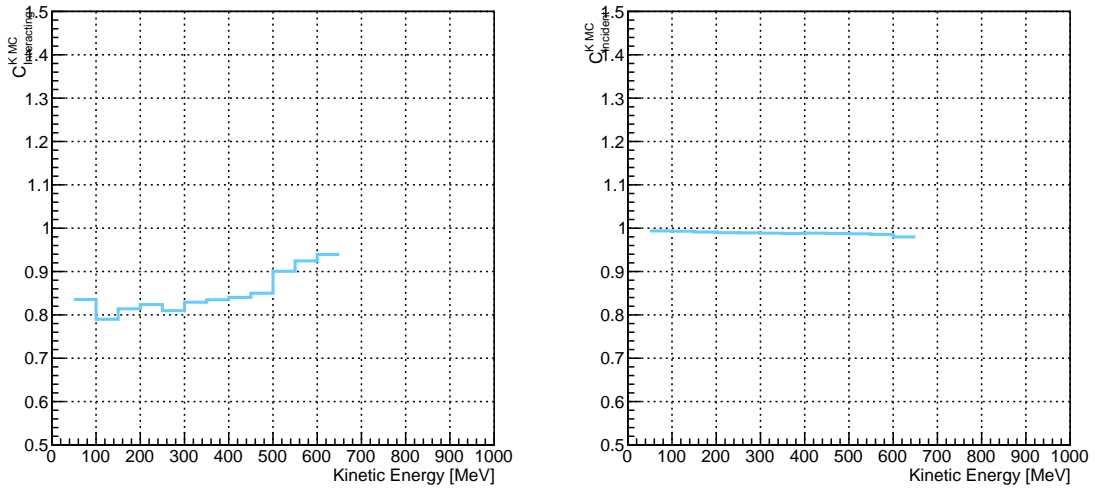


Figure 7.4: *Left:* MC estimated relative kaon content for kaons interacting hadronically as function of kinetic energy. *Right:* MC estimated relative kaon content for incident histogram a function of kinetic energy.

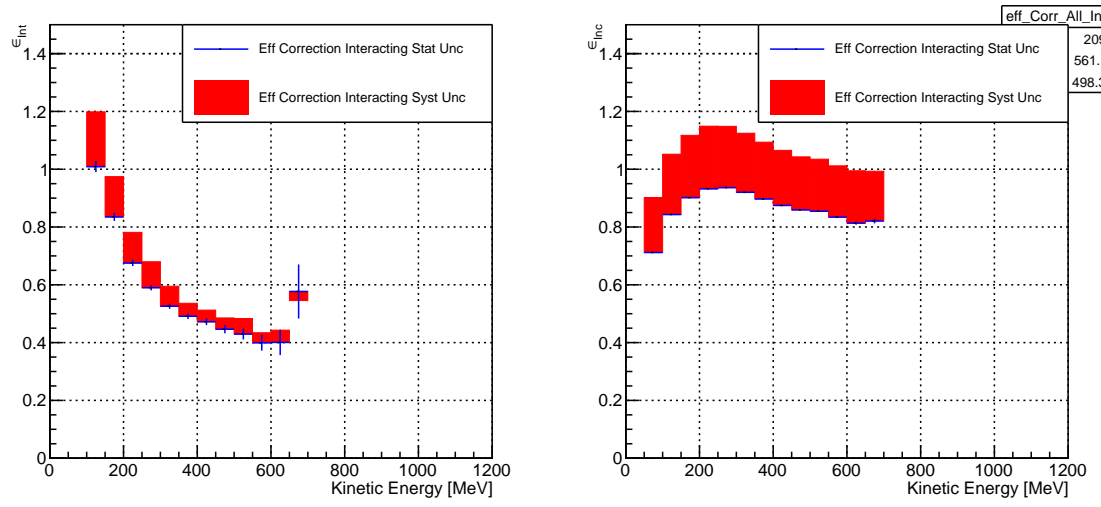


Figure 7.5: *Left:* Efficiency correction on the interacting histogram, statistical uncertainty in blue, systematic uncertainty in red. *Right:* Efficiency correction on the incident histogram, statistical uncertainty in blue, systematic uncertainty in red.

2445 efficiency correction to the raw cross section. The plot shows the measurement ob-
 2446 tained on the full dataset, statistical uncertainty in black and systematic uncertainty
 2447 in red. The Geant4 prediction for the total hadronic cross section for angle scattering
 2448 greater than 5° is displayed in green.

2449 The systematic uncertainty on the cross section is the sum in quadrature of the
 2450 statistical uncertainty, the systematic uncertainty related to the kinetic energy mea-
 2451 surement and the systematic uncertainty related to the efficiency correction.

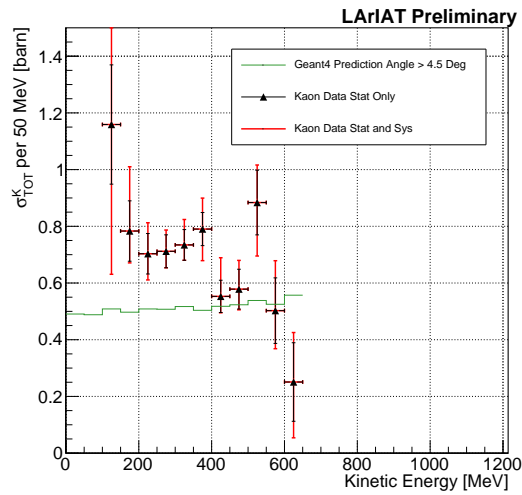


Figure 7.6: (K^+ -Ar) total hadronic cross section for scattering angles greater than 5° measured in the 60A sample, statistical uncertainty in black and systematic uncertainty in red. The Geant4 prediction for the total hadronic cross section for angle scattering greater than 5° is displayed in green.

2452 **Appendix A**

2453 **Additional Tracking Studies for
2454 LArIAT Cross Section Analyses**

2455 In this section, we describe two studies. The first is a justification of the selection
2456 criteria for the beamline handshake with the TPC information. We perform this
2457 study to boost the correct identification of the particles in the TPC associated with
2458 the beamline information, while maintaining sufficient statistics for the cross section
2459 measurement. The second study is an optimization of the tracking algorithm, with
2460 the scope of maximizing the identification of the hadronic interaction point inside the
2461 TPC. These two studies are related, since the optimization of the tracking is per-
2462 formed on TPC tracks which have been matched to the wire chamber track; in turn,
2463 the tracking algorithm for TPC tracks determines the number of reconstructed tracks
2464 in each event used to try the matching with the wire chamber track. Starting with
2465 a sensible tracking reconstruction, we perform the WC2TPC matching optimization
2466 first, then the tracking optimization. The WC2TPC match purity and efficiency are
2467 then calculated again with the optimized tracking.

2468 **A.0.1 Study of WC to TPC Match**

2469 Plots I want in this section:

- 2470 1. WC2TPC MC DeltaX, DeltaY and α

2471 Scope of this study is assessing the goodness of the wire chamber to TPC match
2472 on Monte Carlo and decide the selection values we will use on data. A word of caution
2473 is necessary here. With this study, we want to minimize pathologies associated with
2474 the presence of the primary hadron itself, e.g. the incorrect association between the
2475 beamline hadron and its decay products inside the TPC. Assessing the contamination
2476 from pile-up¹, albeit related, is beyond the scope of this study.

2477 In MC, we are able to define a correct WC2TPC match using the Geant4 truth
2478 information. We are thus able to count how many times the WC tracks is associated
2479 with the wrong TPC reconstructed track.

2480 We define a correct match if the all following conditions are met:

- 2481 - the length of the true primary Geant4 track in the TPC is greater than 2 cm,
- 2482 - the length of the reconstructed track length is greater than 2 cm,
- 2483 - the Z position of the first reconstructed point is within 2 cm from the TPC
2484 front face
- 2485 - the distance between the reconstructed track and the true entering point is the
2486 minimum compared with all the other reconstructed tracks.

2487 In order to count the wrong matches, we consider all the reconstructed tracks
2488 whose Z position of the first reconstructed point lies within 2 cm from the TPC front
2489 face. Events with true length in TPC < 2 cm are included. Since hadrons are shot

1. We remind the reader that the DDMC is a single particle Monte Carlo, where the beam pile up is not simulated.

2490 100 cm upstream from the TPC front face, the following two scenarios are possible
2491 from a truth standpoint:

2492 [Ta] the primary hadron decays or interact strongly before getting to the TPC,

2493 [Tb] the primary hadron enters the TPC.

2494 As described in Section 4.2, we define a WC2TPC match according to the relative
2495 position of the WC and TPC track parametrized with ΔR and the angle between
2496 them, parametrized with α . Once we choose the selection values r_T and α_T to de-
2497 termine a reconstructed WC2TPC match, the following five scenarios are possible in
2498 the truth to reconstruction interplay :

2499 1) only the correct track is matched

2500 2) only one wrong track is matched

2501 3) the correct track and one (or more) wrong tracks are matched

2502 4) multiple wrong tracks matched.

2503 5) no reconstructed tracks are matched

2504 Since we keep only events with one and only one match, we discard cases 3), 4)
2505 and 5) from the events used in the cross section measurement. For each set of r_T and
2506 α_T selection value, we define purity and efficiency of the selection as follows:

$$\text{Efficiency} = \frac{\text{Number of events correctly matched}}{\text{Number of events with primary in TPC}}, \quad (\text{A.1})$$

$$\text{Purity} = \frac{\text{Number of events correctly matched}}{\text{Total number of matched events}}. \quad (\text{A.2})$$

2507 Figure A.1 shows the efficiency (left) and purity (right) for WC2TPC match as
2508 a function of the radius, r_T , and angle, α_T , selection value. It is apparent how both

efficiency and purity are fairly flat as a function of the radius selection value at a given angle. This is not surprising. Since we are studying a single particle gun Monte Carlo sample, the wrong matches can occur only for mis-tracking of the primary or for association with decay products; decay products will tend to be produced at large angles compared to the primary, but could be fairly close to the in x and y projection of the primary. The radius cut would play a key role in removing pile up events.

For LArIAT cross section measurements, we generally prefer purity over efficiency, since a sample of particles of a pure species will lead to a better measurement. Obviously, purity should be balanced with a sensible efficiency to avoid rejecting the whole sample.

We choose $(\alpha_T, r_T) = (8 \text{ deg}, 4 \text{ cm})$ and get a MC 85% efficiency and 98% purity for the kaon sample and a MC 95% efficiency and 90% purity for the pion sample.

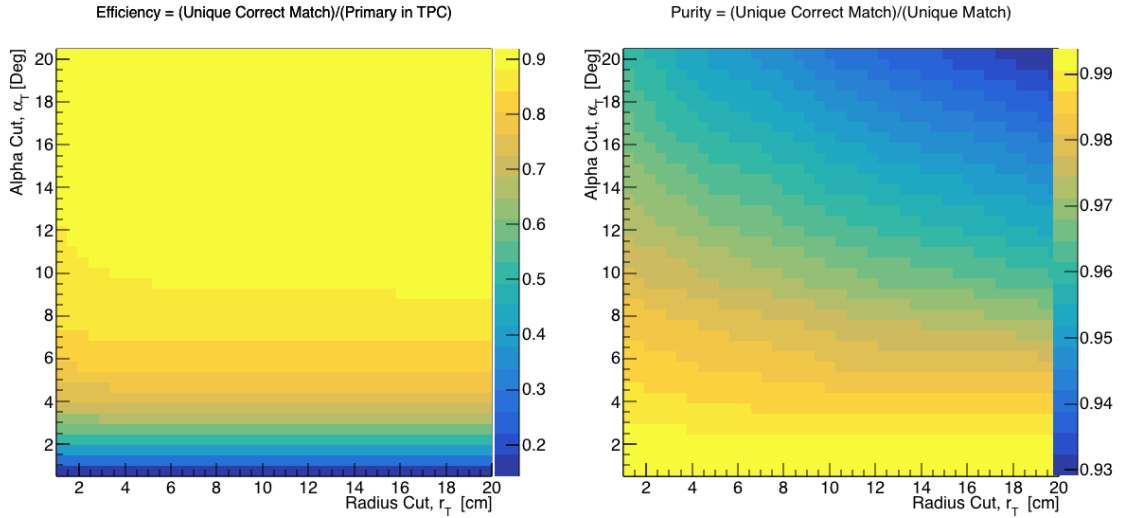


Figure A.1: Efficiency (left) and purity (right) for WC2TPC match as a function of the radius and angle selections for the kaon sample.

A.0.2 Tracking Optimization

2522 **Appendix B**

2523 **Energy Calibration**

2524 Scope of the energy calibration is to identify the factors which convert the charge
2525 collected (dQ) to energy deposited in the chamber (dE). As described in section
2526 2.1.5, this is a multi-step procedure. In LArIAT, we first correct the raw charge by
2527 the electronic noise on the considered wire [102], then by the electron lifetime [103],
2528 and then by the recombination using the ArgoNeut recombination values. Lastly, we
2529 apply overall calibration of the energy, i.e. we determine the “calorimetry constants”
2530 using the procedure described in this section.

2531 We independently determine the calorimetry constants for Data and Monte Carlo
2532 in the LArIAT Run-II Data samples using a parametrization of the stopping power
2533 (a.k.a. energy deposited per unit length, dE/dX) as a function of momentum. This is
2534 done by comparing the stopping power measured on reconstructed quantities against
2535 the Bethe-Bloch theoretical prediction for various particle species (see Equation 2.1).
2536 We obtain the theoretical expectation for the dE/dX most probable value of pions
2537 (π), muons (μ), kaons (K), and protons (p) in the momentum range most relevant
2538 for LArIAT (Figure B.1) using the tables provided by the Particle Data Group [100]
2539 for liquid argon [1].

2540 The basic idea of this calibration technique is to utilize a sample of beamline

2541 events with known particle species and momentum to measure the dE/dX of the
2542 corresponding tracks in the TPC. In particular, we decided to use positive pions as
2543 calibration sample and samples from all the other particle species as cross check. Once
2544 the dE/dX of the positive pion sample has been measured at various momenta, we
2545 tune to calorimetry constants within the reconstruction software to align the measured
2546 values to match the theoretical ones found in Figure B.1.

2547 In data, we start by selecting a sample of beamline positive pion beamline can-
2548 didates without any restriction on their measured momentum¹. We then apply the
2549 WC2TPC match and subtract the energy loss upstream to the TPC front face, de-
2550 termining the momentum at the TPC front face. For each surviving pion candidate,
2551 we measure the dE/dx at each of the first 12 spacepoints associated the 3D recon-
2552 structed track, corresponding to a ~ 5 cm portion. These dE/dX measurements are
2553 then put into a histogram that corresponds to measured momentum of the track.
2554 The dE/dX histograms are sampled every 50 MeV/c in momentum (e.g. 150 MeV/c
2555 $< P < 200$ MeV/c, 200 MeV/c $< P < 250$ /c MeV, etc...). This process of selecting,
2556 sampling, and recording the dE/dX for various momentum bins is repeated over the
2557 entire sample of events, allowing us to collect sufficient statistic in most of the mo-
2558 mentum bins between 150 MeV/c and 1100 MeV/c. On average, pions and muons
2559 only lose ~ 10 MeV in this 5 cm section of the track and protons lose ~ 20 MeV. Thus
2560 choosing 50 MeV/c size bins for our histograms covers the energy spread within those
2561 bins due to energy loss from ionization for all the particle species identifiable in the
2562 beamline. Each 50 MeV/c momentum binned dE/dX histogram is now fit with a
2563 simple Landau function. The most probable value (MPV) and the associated error
2564 on the MPV from the fit are extracted and plotted against the theoretical prediction
2565 Figure B.1. Depending on the outcome of the data-prediction comparison, we modify
2566 the calorimetry constants and we repeat the procedure until a qualitative agreement

1. it should be noted that some muon and position contamination is present in the π^+ sample

2567 is achieved. We perform this tuning for the collection and induction plane separately.
 2568 As a cross check to the calorimetry constants determined using the positive pions,
 2569 we lock the constants and plot the dE/dx versus momentum distribution of all the
 2570 other particle species identifiable in the beamline data ($\pi/\mu/e$, K , p, in both polarities)
 2571 against the corresponding Beth-Bloch prediction. The agreement between data
 2572 from the other particle species and the predictions is the expected result of this cross
 2573 check. The results of the tuning and cross check for Run-II data on the collection
 2574 plane is shown in Figure B.2 negative polarity data on top, positive polarity data on
 2575 the bottom.

2576 In MC, we simulate the corresponding positive pion sample with the DDMC (see
 2577 section 5.2.2) and follow the same steps as in data. More details on the calorimetry
 2578 tuning can be found in [78].

2579 **Add agreement between data and MC for dedx for pions**

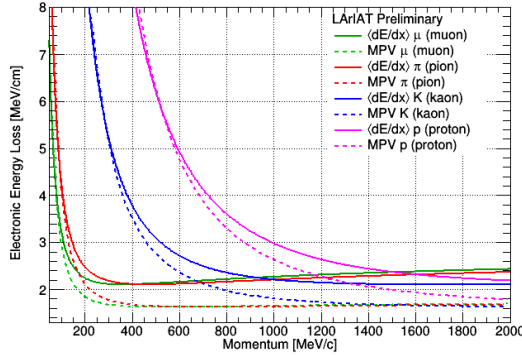


Figure B.1: Stopping power for pions, muons, kaons, and protons in liquid argon over the momentum range most relevant for LArIAT according to the Beth-Bloch equation. The solid lines represent the prediction for the mean energy dE/dX , while the dashed lines are the predictions for the MPV.

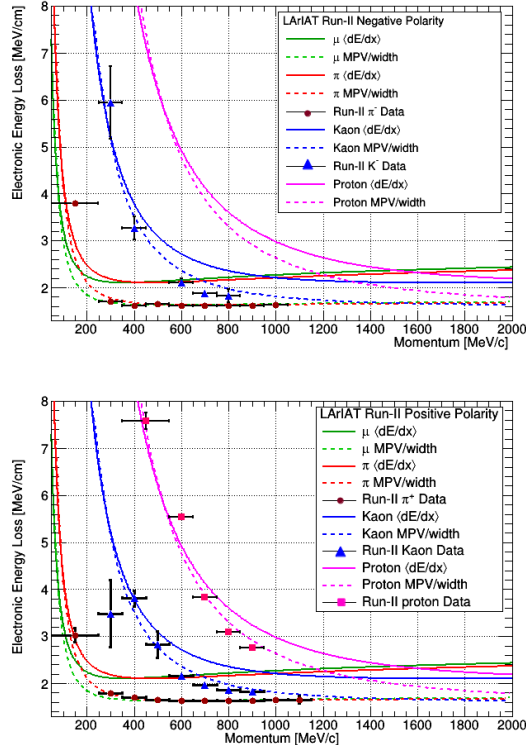


Figure B.2: Stopping power versus Momentum for Run-II negative (top) and positive (bottom) polarity data. We achieve the agreement between the Bethe-Bloch predictions and the distribution obtained with of the positive pions (top plot, red dots) by tuning the calorimetry constants. Once the calorimetry constants are locked in, the agreement between the other particle species and the Bethe-Bloch predictions follows naturally.

2580 **Bibliography**

- 2581 [1] PDG Tables for Liquid Argon. . Technical report.
- 2582 [2] Precision electroweak measurements on the Z resonance. *Physics Reports*,
2583 427(5):257 – 454, 2006.
- 2584 [3] K. Abe, J. Amey, C. Andreopoulos, M. Antonova, S. Aoki, A. Ariga, D. Au-
2585 tiero, S. Ban, M. Barbi, G. J. Barker, G. Barr, C. Barry, P. Bartet-Friburg,
2586 M. Batkiewicz, V. Berardi, S. Berkman, S. Bhadra, S. Bienstock, A. Blondel,
2587 S. Bolognesi, S. Bordoni, S. B. Boyd, D. Brailsford, A. Bravar, C. Bronner,
2588 M. Buizza Avanzini, R. G. Calland, T. Campbell, S. Cao, S. L. Cartwright,
2589 M. G. Catanesi, A. Cervera, C. Checchia, D. Cherdack, N. Chikuma,
2590 G. Christodoulou, A. Clifton, J. Coleman, G. Collazuol, D. Coplowe, A. Cudd,
2591 A. Dabrowska, G. De Rosa, T. Dealtry, P. F. Denner, S. R. Dennis, C. Densham,
2592 D. Dewhurst, F. Di Lodovico, S. Di Luise, S. Dolan, O. Drapier, K. E. Duffy,
2593 J. Dumarchez, M. Dziewiecki, S. Emery-Schrenk, A. Ereditato, T. Feusels,
2594 A. J. Finch, G. A. Fiorentini, M. Friend, Y. Fujii, D. Fukuda, Y. Fukuda,
2595 V. Galymov, A. Garcia, C. Giganti, F. Gizzarelli, T. Golan, M. Gonin, D. R.
2596 Hadley, L. Haegel, M. D. Haigh, D. Hansen, J. Harada, M. Hartz, T. Hasegawa,
2597 N. C. Hastings, T. Hayashino, Y. Hayato, R. L. Helmer, A. Hillairet, T. Hiraki,
2598 A. Hiramatsu, S. Hirota, M. Hogan, J. Holeczek, F. Hosomi, K. Huang, A. K.
2599 Ichikawa, M. Ikeda, J. Imber, J. Insler, R. A. Intonti, T. Ishida, T. Ishii, E. Iwai,
2600 K. Iwamoto, A. Izmaylov, B. Jamieson, M. Jiang, S. Johnson, P. Jonsson,

2601 C. K. Jung, M. Kabirnezhad, A. C. Kaboth, T. Kajita, H. Kakuno, J. Kameda,
2602 D. Karlen, T. Katori, E. Kearns, M. Khabibullin, A. Khotjantsev, H. Kim,
2603 J. Kim, S. King, J. Kisiel, A. Knight, A. Knox, T. Kobayashi, L. Koch, T. Koga,
2604 A. Konaka, K. Kondo, L. L. Kormos, A. Korzenev, Y. Koshio, K. Kowalik,
2605 W. Kropp, Y. Kudenko, R. Kurjata, T. Kutter, J. Lagoda, I. Lamont, M. Lam-
2606 oureux, E. Larkin, P. Lasorak, M. Laveder, M. Lawe, M. Licciardi, T. Lindner,
2607 Z. J. Liptak, R. P. Litchfield, X. Li, A. Longhin, J. P. Lopez, T. Lou, L. Ludovici,
2608 X. Lu, L. Magaletti, K. Mahn, M. Malek, S. Manly, A. D. Marino, J. F. Martin,
2609 P. Martins, S. Martynenko, T. Maruyama, V. Matveev, K. Mavrokordis, W. Y.
2610 Ma, E. Mazzucato, M. McCarthy, N. McCauley, K. S. McFarland, C. McGrew,
2611 A. Mefodiev, C. Metelko, M. Mezzetto, P. Mijakowski, A. Minamino, O. Mi-
2612 neev, S. Mine, A. Missent, M. Miura, S. Moriyama, Th. A. Mueller, J. Myslik,
2613 T. Nakadaira, M. Nakahata, K. G. Nakamura, K. Nakamura, K. D. Nakamura,
2614 Y. Nakanishi, S. Nakayama, T. Nakaya, K. Nakayoshi, C. Nantais, C. Nielsen,
2615 M. Nirko, K. Nishikawa, Y. Nishimura, P. Novella, J. Nowak, H. M. O'Keeffe,
2616 K. Okumura, T. Okusawa, W. Oryszczak, S. M. Oser, T. Ovsyannikova, R. A.
2617 Owen, Y. Oyama, V. Palladino, J. L. Palomino, V. Paolone, N. D. Patel,
2618 P. Paudyal, M. Pavin, D. Payne, J. D. Perkin, Y. Petrov, L. Pickard, L. Pick-
2619 ering, E. S. Pinzon Guerra, C. Pistillo, B. Popov, M. Posiadala-Zezula, J.-M.
2620 Poutissou, R. Poutissou, P. Przewlocki, B. Quilain, T. Radermacher, E. Radi-
2621 cioni, P. N. Ratoff, M. Ravonel, M. A. Rayner, A. Redij, E. Reinherz-Aronis,
2622 C. Riccio, P. A. Rodrigues, E. Rondio, B. Rossi, S. Roth, A. Rubbia, A. Rychter,
2623 K. Sakashita, F. Sánchez, E. Scantamburlo, K. Scholberg, J. Schwehr, M. Scott,
2624 Y. Seiya, T. Sekiguchi, H. Sekiya, D. Sgalaberna, R. Shah, A. Shaikhiev,
2625 F. Shaker, D. Shaw, M. Shiozawa, T. Shirahige, S. Short, M. Smy, J. T.
2626 Sobczyk, H. Sobel, M. Sorel, L. Southwell, J. Steinmann, T. Stewart, P. Stowell,
2627 Y. Suda, S. Suvorov, A. Suzuki, S. Y. Suzuki, Y. Suzuki, R. Tacik, M. Tada,

- 2628 A. Takeda, Y. Takeuchi, H. K. Tanaka, H. A. Tanaka, D. Terhorst, R. Terri,
2629 T. Thakore, L. F. Thompson, S. Tobayama, W. Toki, T. Tomura, C. Touramani,
2630 T. Tsukamoto, M. Tzanov, Y. Uchida, M. Vagins, Z. Vallari, G. Vasseur,
2631 T. Vladislavljevic, T. Wachala, C. W. Walter, D. Wark, M. O. Wascko, A. We-
2632 ber, R. Wendell, R. J. Wilkes, M. J. Wilking, C. Wilkinson, J. R. Wilson, R. J.
2633 Wilson, C. Wret, Y. Yamada, K. Yamamoto, M. Yamamoto, C. Yanagisawa,
2634 T. Yano, S. Yen, N. Yershov, M. Yokoyama, K. Yoshida, T. Yuan, M. Yu, A. Za-
2635 lewska, J. Zalipska, L. Zambelli, K. Zaremba, M. Ziembicki, E. D. Zimmerman,
2636 M. Zito, and J. Źmuda. Combined analysis of neutrino and antineutrino oscil-
2637 lations at t2k. *Phys. Rev. Lett.*, 118:151801, Apr 2017.
- 2638 [4] K. Abe, Y. Haga, Y. Hayato, M. Ikeda, K. Iyogi, J. Kameda, Y. Kishimoto,
2639 M. Miura, S. Moriyama, M. Nakahata, T. Nakajima, Y. Nakano, S. Nakayama,
2640 A. Orii, H. Sekiya, M. Shiozawa, A. Takeda, H. Tanaka, T. Tomura, R. A. Wen-
2641 dell, R. Akutsu, T. Irvine, T. Kajita, K. Kaneyuki, Y. Nishimura, E. Richard,
2642 K. Okumura, L. Labarga, P. Fernandez, J. Gustafson, C. Kachulis, E. Kearns,
2643 J. L. Raaf, J. L. Stone, L. R. Sulak, S. Berkman, C. M. Nantais, H. A.
2644 Tanaka, S. Tobayama, M. Goldhaber, W. R. Kropp, S. Mine, P. Weatherly,
2645 M. B. Smy, H. W. Sobel, V. Takhistov, K. S. Ganezer, B. L. Hartfiel, J. Hill,
2646 N. Hong, J. Y. Kim, I. T. Lim, R. G. Park, A. Himmel, Z. Li, E. O’Sullivan,
2647 K. Scholberg, C. W. Walter, T. Wongjirad, T. Ishizuka, S. Tasaka, J. S. Jang,
2648 J. G. Learned, S. Matsuno, S. N. Smith, M. Friend, T. Hasegawa, T. Ishida,
2649 T. Ishii, T. Kobayashi, T. Nakadaira, K. Nakamura, Y. Oyama, K. Sakashita,
2650 T. Sekiguchi, T. Tsukamoto, A. T. Suzuki, Y. Takeuchi, T. Yano, S. V. Cao,
2651 T. Hiraki, S. Hirota, K. Huang, T. Kikawa, A. Minamino, T. Nakaya, K. Suzuki,
2652 Y. Fukuda, K. Choi, Y. Itow, T. Suzuki, P. Mijakowski, K. Frankiewicz, J. Hig-
2653 night, J. Imber, C. K. Jung, X. Li, J. L. Palomino, M. J. Wilking, C. Yanag-
2654 isawa, D. Fukuda, H. Ishino, T. Kayano, A. Kibayashi, Y. Koshio, T. Mori,

- 2655 M. Sakuda, C. Xu, Y. Kuno, R. Tacik, S. B. Kim, H. Okazawa, Y. Choi,
2656 K. Nishijima, M. Koshiba, Y. Totsuka, Y. Suda, M. Yokoyama, C. Bronner,
2657 M. Hartz, K. Martens, Ll. Marti, Y. Suzuki, M. R. Vagins, J. F. Martin, A. Kon-
2658 aka, S. Chen, Y. Zhang, and R. J. Wilkes. Search for proton decay via $p \rightarrow e^+ \pi^0$
2659 and $p \rightarrow \mu^+ \pi^0$ in 0.31 megaton · years exposure of the super-kamiokande water
2660 cherenkov detector. *Phys. Rev. D*, 95:012004, Jan 2017.
- 2661 [5] R Acciarri, C Adams, J Asaadi, B Baller, T Bolton, C Bromberg, F Ca-
2662 vanna, E Church, D Edmunds, A Ereditato, S Farooq, B Fleming, H Greenlee,
2663 G Horton-Smith, C James, E Klein, K Lang, P Laurens, D McKee, R Mehdiyev,
2664 B Page, O Palamara, K Partyka, G Rameika, B Rebel, M Soderberg, J Spitz,
2665 A M Szelc, M Weber, M Wojcik, T Yang, and G P Zeller. A study of electron
2666 recombination using highly ionizing particles in the argoneut liquid argon tpc.
2667 *Journal of Instrumentation*, 8(08):P08005, 2013.
- 2668 [6] R Acciarri, M Antonello, B Baibussinov, M Baldo-Ceolin, P Benetti,
2669 F Calaprice, E Calligarich, M Cambiaghi, N Canci, F Carbonara, F Cavanna,
2670 S Centro, A G Cocco, F Di Pompeo, G Fiorillo, C Galbiati, V Gallo, L Grandi,
2671 G Meng, I Modena, C Montanari, O Palamara, L Pandola, G B Piano Mortari,
2672 F Pietropaolo, G L Raselli, M Roncadelli, M Rossella, C Rubbia, E Segreto,
2673 A M Szelc, S Ventura, and C Vignoli. Effects of nitrogen contamination in
2674 liquid argon. *Journal of Instrumentation*, 5(06):P06003, 2010.
- 2675 [7] R. Acciarri et al. Demonstration and Comparison of Operation of Photomulti-
2676 plier Tubes at Liquid Argon Temperature. *JINST*, 7:P01016, 2012.
- 2677 [8] R. Acciarri et al. Design and Construction of the MicroBooNE Detector. *JINST*,
2678 12(02):P02017, 2017.

- 2679 [9] R. Acciarri et al. First Observation of Low Energy Electron Neutrinos in a
2680 Liquid Argon Time Projection Chamber. *Phys. Rev.*, D95(7):072005, 2017.
2681 [Phys. Rev.D95,072005(2017)].
- 2682 [10] M Adamowski, B Carls, E Dvorak, A Hahn, W Jaskierny, C Johnson, H Jostlein,
2683 C Kendziora, S Lockwitz, B Pahlka, R Plunkett, S Pordes, B Rebel, R Schmitt,
2684 M Stancari, T Tope, E Voirin, and T Yang. The liquid argon purity demon-
2685 strator. *Journal of Instrumentation*, 9(07):P07005, 2014.
- 2686 [11] C. Adams et al. The Long-Baseline Neutrino Experiment: Exploring Funda-
2687 mental Symmetries of the Universe. 2013.
- 2688 [12] P. Adamson, L. Aliaga, D. Ambrose, N. Anfimov, A. Antoshkin, E. Arrieta-
2689 Diaz, K. Augsten, A. Aurisano, C. Backhouse, M. Baird, B. A. Bambah,
2690 K. Bays, B. Behera, S. Bending, R. Bernstein, V. Bhatnagar, B. Bhuyan,
2691 J. Bian, T. Blackburn, A. Bolshakova, C. Bromberg, J. Brown, G. Brunetti,
2692 N. Buchanan, A. Butkevich, V. Bychkov, M. Campbell, E. Catano-Mur, S. Chil-
2693 dress, B. C. Choudhary, B. Chowdhury, T. E. Coan, J. A. B. Coelho, M. Colo,
2694 J. Cooper, L. Corwin, L. Cremonesi, D. Cronin-Hennessy, G. S. Davies, J. P.
2695 Davies, P. F. Derwent, R. Dharmapalan, P. Ding, Z. Djurcic, E. C. Dukes,
2696 H. Duyang, S. Edayath, R. Ehrlich, G. J. Feldman, M. J. Frank, M. Gabrielyan,
2697 H. R. Gallagher, S. Germani, T. Ghosh, A. Giri, R. A. Gomes, M. C. Goodman,
2698 V. Grichine, R. Group, D. Grover, B. Guo, A. Habig, J. Hartnell, R. Hatcher,
2699 A. Hatzikoutelis, K. Heller, A. Himmel, A. Holin, J. Hylen, F. Jediny, M. Judah,
2700 G. K. Kafka, D. Kalra, S. M. S. Kasahara, S. Kasetti, R. Keloth, L. Kolupaeva,
2701 S. Kotelnikov, I. Kourbanis, A. Kreymer, A. Kumar, S. Kurbanov, K. Lang,
2702 W. M. Lee, S. Lin, J. Liu, M. Lokajicek, J. Lozier, S. Luchuk, K. Maan, S. Mag-
2703 ill, W. A. Mann, M. L. Marshak, K. Matera, V. Matveev, D. P. Méndez, M. D.
2704 Messier, H. Meyer, T. Miao, W. H. Miller, S. R. Mishra, R. Mohanta, A. Moren,

- 2705 L. Mualem, M. Muether, S. Mufson, R. Murphy, J. Musser, J. K. Nelson,
2706 R. Nichol, E. Niner, A. Norman, T. Nosek, Y. Oksuzian, A. Olshevskiy, T. Ol-
2707 son, J. Paley, P. Pandey, R. B. Patterson, G. Pawloski, D. Pershey, O. Petrova,
2708 R. Petti, S. Phan-Budd, R. K. Plunkett, R. Poling, B. Potukuchi, C. Principato,
2709 F. Psihas, A. Radovic, R. A. Rameika, B. Rebel, B. Reed, D. Rocco, P. Rojas,
2710 V. Ryabov, K. Sachdev, P. Sail, O. Samoylov, M. C. Sanchez, R. Schroeter,
2711 J. Sepulveda-Quiroz, P. Shanahan, A. Sheshukov, J. Singh, J. Singh, P. Singh,
2712 V. Singh, J. Smolik, N. Solomey, E. Song, A. Sousa, K. Soustruznik, M. Strait,
2713 L. Suter, R. L. Talaga, M. C. Tamsett, P. Tas, R. B. Thayyullathil, J. Thomas,
2714 X. Tian, S. C. Tognini, J. Tripathi, A. Tsaris, J. Urheim, P. Vahle, J. Vasel,
2715 L. Vinton, A. Vold, T. Vrba, B. Wang, M. Wetstein, D. Whittington, S. G. Wo-
2716 jcicki, J. Wolcott, N. Yadav, S. Yang, J. Zalesak, B. Zamorano, and R. Zwaska.
2717 Constraints on oscillation parameters from ν_e appearance and ν_μ disappearance
2718 in nova. *Phys. Rev. Lett.*, 118:231801, Jun 2017.
- 2719 [13] Alan Agresti. *Categorical Data Analysis*. Wiley Series in Probability and Statis-
2720 tics. Wiley, 2013.
- 2721 [14] A. Aguilar-Arevalo et al. Evidence for neutrino oscillations from the observation
2722 of anti-neutrino(electron) appearance in a anti-neutrino(muon) beam. *Phys.*
2723 *Rev.*, D64:112007, 2001.
- 2724 [15] A. A. Aguilar-Arevalo et al. Improved Search for $\bar{\nu}_\mu \rightarrow \bar{\nu}_e$ Oscillations in the
2725 MiniBooNE Experiment. *Phys. Rev. Lett.*, 110:161801, 2013.
- 2726 [16] S. Amoruso et al. Study of electron recombination in liquid argon with the
2727 ICARUS TPC. *Nucl. Instrum. Meth.*, A523:275–286, 2004.
- 2728 [17] C. Anderson et al. The ArgoNeuT Detector in the NuMI Low-Energy beam
2729 line at Fermilab. *JINST*, 7:P10019, 2012.

- 2730 [18] C. Andreopoulos et al. The GENIE Neutrino Monte Carlo Generator. *Nucl.*
2731 *Instrum. Meth.*, A614:87–104, 2010.
- 2732 [19] Timofei Bolshakov Andrey Petrov. Java synoptic toolkit. Technical report,
2733 Sept 2010.
- 2734 [20] M. Antonello, B. Baibussinov, P. Benetti, E. Calligarich, N. Canci, S. Cen-
2735 tro, A. Cesana, K. Cieslik, D. B. Cline, A. G. Cocco, A. Dabrowska, D. De-
2736 qual, A. Dermenev, R. Dolfini, C. Farnese, A. Fava, A. Ferrari, G. Fiorillo,
2737 D. Gibin, S. Gninenko, A. Guglielmi, M. Haranczyk, J. Holeczek, A. Ivashkin,
2738 J. Kisiel, I. Kochanek, J. Lagoda, S. Mania, A. Menegolli, G. Meng, C. Monta-
2739 nari, S. Otwinowski, A. Piazzoli, P. Picchi, F. Pietropaolo, P. Plonski, A. Rap-
2740 poldi, G. L. Raselli, M. Rossella, C. Rubbia, P. Sala, A. Scaramelli, E. Seg-
2741 reto, F. Sergiampietri, D. Stefan, J. Stepaniak, R. Sulej, M. Szarska, M. Ter-
2742 rani, F. Varanini, S. Ventura, C. Vignoli, H. Wang, X. Yang, A. Zalewska,
2743 and K. Zaremba. Precise 3d track reconstruction algorithm for the ICARUS
2744 t600 liquid argon time projection chamber detector. *Advances in High Energy*
2745 *Physics*, 2013:1–16, 2013.
- 2746 [21] M. Antonello et al. A Proposal for a Three Detector Short-Baseline Neutrino
2747 Oscillation Program in the Fermilab Booster Neutrino Beam. 2015.
- 2748 [22] D. Ashery, I. Navon, G. Azuelos, H. K. Walter, H. J. Pfeiffer, and F. W.
2749 Schlepütz. True absorption and scattering of pions on nuclei. *Phys. Rev. C*,
2750 23:2173–2185, May 1981.
- 2751 [23] C. Athanassopoulos et al. Evidence for $\nu(\mu) \rightarrow \nu(e)$ neutrino oscillations
2752 from LSND. *Phys. Rev. Lett.*, 81:1774–1777, 1998.

- 2753 [24] Borut Bajc, Junji Hisano, Takumi Kuwahara, and Yuji Omura. Threshold
2754 corrections to dimension-six proton decay operators in non-minimal {SUSY}
2755 $\text{su}(5)$ {GUTs}. *Nuclear Physics B*, 910:1 – 22, 2016.
- 2756 [25] B. Baller. Trajcluster user guide. Technical report, apr 2016.
- 2757 [26] Gary Barker. Neutrino event reconstruction in a liquid argon TPC. *Journal of*
2758 *Physics: Conference Series*, 308:012015, jul 2011.
- 2759 [27] BASF Corp. 100 Park Avenue, Florham Park, NJ 07932 USA.
- 2760 [28] R. Becker-Szendy, C. B. Bratton, D. R. Cady, D. Casper, R. Claus, M. Crouch,
2761 S. T. Dye, W. Gajewski, M. Goldhaber, T. J. Haines, P. G. Halverson, T. W.
2762 Jones, D. Kielczewska, W. R. Kropp, J. G. Learned, J. M. LoSecco, C. Mc-
2763 Grew, S. Matsuno, J. Matthews, M. S. Mudah, L. Price, F. Reines, J. Schultz,
2764 D. Sinclair, H. W. Sobel, J. L. Stone, L. R. Sulak, R. Svoboda, G. Thornton,
2765 and J. C. van der Velde. Search for proton decay into $e^+ + \pi^0$ in the imb-3
2766 detector. *Phys. Rev. D*, 42:2974–2976, Nov 1990.
- 2767 [29] J B Birks. Scintillations from organic crystals: Specific fluorescence and relative
2768 response to different radiations. *Proceedings of the Physical Society. Section A*,
2769 64(10):874, 1951.
- 2770 [30] A. Bodek and J. L. Ritchie. Further studies of fermi-motion effects in lepton
2771 scattering from nuclear targets. *Phys. Rev. D*, 24:1400–1402, Sep 1981.
- 2772 [31] Mark G. Boulay and A. Hime. Direct WIMP detection using scintillation time
2773 discrimination in liquid argon. 2004.
- 2774 [32] D. V. Bugg, R. S. Gilmore, K. M. Knight, D. C. Salter, G. H. Stafford, E. J. N.
2775 Wilson, J. D. Davies, J. D. Dowell, P. M. Hattersley, R. J. Homer, A. W. O'dell,

- 2776 A. A. Carter, R. J. Tapper, and K. F. Riley. Kaon-nucleon total cross sections
2777 from 0.6 to 2.65 gev/ *c. Phys. Rev.*, 168:1466–1475, Apr 1968.
- 2778 [33] W. M. Burton and B. A. Powell. Fluorescence of tetraphenyl-butadiene in the
2779 vacuum ultraviolet. *Applied Optics*, 12(1):87, jan 1973.
- 2780 [34] CAEN. Caen v1495 data sheet. Technical report, jan 2018.
- 2781 [35] CAEN. Caen v1740 data sheet. Technical report, jan 2018.
- 2782 [36] A. S. Carroll, I. H. Chiang, C. B. Dover, T. F. Kycia, K. K. Li, P. O. Mazur,
2783 D. N. Michael, P. M. Mockett, D. C. Rahm, and R. Rubinstein. Pion-nucleus
2784 total cross sections in the (3,3) resonance region. *Phys. Rev. C*, 14:635–638,
2785 Aug 1976.
- 2786 [37] D. Casper. The nuance neutrino physics simulation, and the future. *Nuclear
2787 Physics B - Proceedings Supplements*, 112(1-3):161–170, nov 2002.
- 2788 [38] A. Cervera, A. Donini, M.B. Gavela, J.J. Gomez Cádenas, P. Hernández,
2789 O. Mena, and S. Rigolin. Golden measurements at a neutrino factory. *Nu-
2790 clear Physics B*, 579(1-2):17–55, jul 2000.
- 2791 [39] E. Church. LArSoft: A Software Package for Liquid Argon Time Projection
2792 Drift Chambers. 2013.
- 2793 [40] ATLAS Collaboration. Observation of a new particle in the search for the
2794 standard model higgs boson with the ATLAS detector at the LHC. *Physics
2795 Letters B*, 716(1):1–29, sep 2012.
- 2796 [41] CMS Collaboration. Observation of a new boson at a mass of 125 gev with the
2797 cms experiment at the lhc. *Physics Letters B*, 716(1):30 – 61, 2012.
- 2798 [42] The LArIAT Collaboration. The liquid argon in a testbeam (lariat) experiment.
2799 Technical report, In Preparation 2018.

- 2800 [43] Stefano Dell’Oro, Simone Marcocci, Matteo Viel, and Francesco Vissani. Neu-
2801 trinoless double beta decay: 2015 review. *Advances in High Energy Physics*,
2802 2016:1–37, 2016.
- 2803 [44] S.E. Derenzo, A.R. Kirschbaum, P.H. Eberhard, R.R. Ross, and F.T. Solmitz.
2804 Test of a liquid argon chamber with 20 m rms resolution. *Nuclear Instruments
2805 and Methods*, 122:319 – 327, 1974.
- 2806 [45] Savas Dimopoulos, Stuart Raby, and Frank Wilczek. Proton Decay in Super-
2807 symmetric Models. *Phys. Lett.*, B112:133, 1982.
- 2808 [46] D. Drakoulakos et al. Proposal to perform a high-statistics neutrino scattering
2809 experiment using a fine-grained detector in the NuMI beam. 2004.
- 2810 [47] A Ereditato, C C Hsu, S Janos, I Kreslo, M Messina, C Rudolf von Rohr,
2811 B Rossi, T Strauss, M S Weber, and M Zeller. Design and operation of
2812 argontube: a 5 m long drift liquid argon tpc. *Journal of Instrumentation*,
2813 8(07):P07002, 2013.
- 2814 [48] Torleif Ericson and Wolfram Weise. *Pions and Nuclei (The International Series
2815 of Monographs on Physics)*. Oxford University Press, 1988.
- 2816 [49] A.A. Aguilar-Arevalo et al. The miniboone detector. *Nuclear Instruments and
2817 Methods in Physics Research Section A: Accelerators, Spectrometers, Detectors
2818 and Associated Equipment*, 599(1):28 – 46, 2009.
- 2819 [50] Antonio Bueno et al. Nucleon decay searches with large liquid argon TPC de-
2820 tectors at shallow depths: atmospheric neutrinos and cosmogenic backgrounds.
2821 *Journal of High Energy Physics*, 2007(04):041–041, apr 2007.
- 2822 [51] A.S. Clough et al. Pion-nucleus total cross sections from 88 to 860 MeV. *Nuclear
2823 Physics B*, 76(1):15–28, jul 1974.

- 2824 [52] B.W. Allardyce et al. Pion reaction cross sections and nuclear sizes. *Nuclear*
2825 *Physics A*, 209(1):1 – 51, 1973.
- 2826 [53] C Athanassopoulos et al. The liquid scintillator neutrino detector and LAMPF
2827 neutrino source. *Nuclear Instruments and Methods in Physics Research Section*
2828 *A: Accelerators, Spectrometers, Detectors and Associated Equipment*, 388(1-
2829 2):149–172, mar 1997.
- 2830 [54] F. Binon et al. Scattering of negative pions on carbon. *Nuclear Physics B*,
2831 17(1):168 – 188, 1970.
- 2832 [55] L. Aliaga et al. Minerva neutrino detector response measured with test beam
2833 data. *Nuclear Instruments and Methods in Physics Research Section A: Ac-*
2834 *celerators, Spectrometers, Detectors and Associated Equipment*, 789:28 – 42,
2835 2015.
- 2836 [56] M Adamowski et al. The liquid argon purity demonstrator. *Journal of Instru-*
2837 *mentation*, 9(07):P07005, 2014.
- 2838 [57] P. Vilain et al. Coherent single charged pion production by neutrinos. *Physics*
2839 *Letters B*, 313(1-2):267–275, aug 1993.
- 2840 [58] R. Acciarri et al. Convolutional neural networks applied to neutrino events
2841 in a liquid argon time projection chamber. *Journal of Instrumentation*,
2842 12(03):P03011, 2017.
- 2843 [59] R. Acciarri et al. Design and construction of the MicroBooNE detector. *Journal*
2844 *of Instrumentation*, 12(02):P02017–P02017, feb 2017.
- 2845 [60] C. E. Aalseth et al.l. DarkSide-20k: A 20 tonne two-phase LAr TPC for direct
2846 dark matter detection at LNGS. *The European Physical Journal Plus*, 133(3),
2847 mar 2018.

- 2848 [61] H Fenker. Standard beam pwc for fermilab. Technical report, Fermi National
2849 Accelerator Lab., Batavia, IL (USA), 1983.
- 2850 [62] H Fesbach. Theoretical nuclear physics: Nuclear reactions. 1992.
- 2851 [63] J. A. Formaggio and G. P. Zeller. From ev to eev: Neutrino cross sections across
2852 energy scales. *Rev. Mod. Phys.*, 84:1307–1341, Sep 2012.
- 2853 [64] E. Friedman et al. K+ nucleus reaction and total cross-sections: New analysis
2854 of transmission experiments. *Phys. Rev.*, C55:1304–1311, 1997.
- 2855 [65] V.M. Gehman, S.R. Seibert, K. Rielage, A. Hime, Y. Sun, D.-M. Mei,
2856 J. Maassen, and D. Moore. Fluorescence efficiency and visible re-emission
2857 spectrum of tetraphenyl butadiene films at extreme ultraviolet wavelengths.
2858 *Nuclear Instruments and Methods in Physics Research Section A: Accelerators,*
2859 *Spectrometers, Detectors and Associated Equipment*, 654(1):116 – 121, 2011.
- 2860 [66] H. Geiger and E. Marsden. On a diffuse reflection of the formula-particles.
2861 *Proceedings of the Royal Society A: Mathematical, Physical and Engineering*
2862 *Sciences*, 82(557):495–500, jul 1909.
- 2863 [67] Howard Georgi and S. L. Glashow. Unity of all elementary-particle forces. *Phys.*
2864 *Rev. Lett.*, 32:438–441, Feb 1974.
- 2865 [68] D.Y. Wong (editor) G.L. Shaw (Editor). *Pion-nucleon Scattering*. John Wiley
2866 & Sons Inc, 1969.
- 2867 [69] Glassman High Voltage, Inc., Precision Regulated High Voltage DC Power Sup-
2868 ply.
- 2869 [70] D S Gorbunov. Sterile neutrinos and their role in particle physics and cosmology.
2870 *Physics-Uspekhi*, 57(5):503, 2014.

- 2871 [71] C. Green, J. Kowalkowski, M. Paterno, M. Fischler, L. Garren, and Q. Lu. The
2872 Art Framework. *J. Phys. Conf. Ser.*, 396:022020, 2012.
- 2873 [72] S. Hansen, D. Jensen, G. Savage, E. Skup, and A. Soha. Fermilab test beam
2874 multi-wire proportional chamber tracking system upgrade. June 2014. International
2875 Conference on Technology and Instrumentation in Particle Physics (TIPP
2876 2014).
- 2877 [73] J. Harada. Non-maximal θ_{23} , large θ_{13} and tri-bimaximal θ_{12} via quark-
2878 lepton complementarity at next-to-leading order. *EPL (Europhysics Letters)*,
2879 103(2):21001, 2013.
- 2880 [74] Peter W. Higgs. Broken symmetries and the masses of gauge bosons. *Physical*
2881 *Review Letters*, 13(16):508–509, oct 1964.
- 2882 [75] P.W. Higgs. Broken symmetries, massless particles and gauge fields. *Physics*
2883 *Letters*, 12(2):132–133, sep 1964.
- 2884 [76] H J Hilke. Time projection chambers. *Reports on Progress in Physics*,
2885 73(11):116201, 2010.
- 2886 [77] N. Ishida, M. Chen, T. Doke, K. Hasuike, A. Hitachi, M. Gaudreau, M. Kase,
2887 Y. Kawada, J. Kikuchi, T. Komiyama, K. Kuwahara, K. Masuda, H. Okada,
2888 Y.H. Qu, M. Suzuki, and T. Takahashi. Attenuation length measurements of
2889 scintillation light in liquid rare gases and their mixtures using an improved
2890 reflection suppresser. *Nuclear Instruments and Methods in Physics Research*
2891 *Section A: Accelerators, Spectrometers, Detectors and Associated Equipment*,
2892 384(2-3):380–386, jan 1997.
- 2893 [78] G. Pulliam J. Asaadi, E. Gramellini. Determination of the electron lifetime in
2894 lariat. Technical report, August 2017.

- 2895 [79] George Jaffé. Zur theorie der ionisation in kolonnen. *Annalen der Physik*,
2896 347(12):303–344, 1913.
- 2897 [80] C. Jarlskog. A basis independent formulation of the connection between quark
2898 mass matrices, CP violation and experiment. *Zeitschrift für Physik C Particles
2899 and Fields*, 29(3):491–497, sep 1985.
- 2900 [81] B J P Jones, C S Chiu, J M Conrad, C M Ignarra, T Katori, and M Toups. A
2901 measurement of the absorption of liquid argon scintillation light by dissolved ni-
2902 tragen at the part-per-million level. *Journal of Instrumentation*, 8(07):P07011,
2903 2013.
- 2904 [82] Benjamin J. P. Jones. *Sterile Neutrinos in Cold Climates*. PhD thesis, MIT,
2905 2015.
- 2906 [83] Cezary Juszczak, Jarosław A. Nowak, and Jan T. Sobczyk. Simulations from
2907 a new neutrino event generator. *Nuclear Physics B - Proceedings Supplements*,
2908 159:211–216, sep 2006.
- 2909 [84] D. I. Kazakov. Beyond the standard model: In search of supersymmetry. In
2910 *2000 European School of high-energy physics, Caramulo, Portugal, 20 Aug-2 Sep 2000: Proceedings*, pages 125–199, 2000.
- 2912 [85] Dae-Gyu Lee, R. N. Mohapatra, M. K. Parida, and Merostar Rani. Predic-
2913 tions for the proton lifetime in minimal nonsupersymmetric $so(10)$ models: An
2914 update. *Phys. Rev. D*, 51:229–235, Jan 1995.
- 2915 [86] M A Leogui de Oliveira. Expression of Interest for a Full-Scale Detector Engi-
2916 neering Test and Test Beam Calibration of a Single-Phase LAr TPC. Technical
2917 Report CERN-SPSC-2014-027. SPSC-EOL-011, CERN, Geneva, Oct 2014.

- 2918 [87] W. H. Lippincott, K. J. Coakley, D. Gastler, A. Hime, E. Kearns, D. N. McK-
2919 insey, J. A. Nikkel, and L. C. Stonehill. Scintillation time dependence and pulse
2920 shape discrimination in liquid argon. *Phys. Rev. C*, 78:035801, Sep 2008.
- 2921 [88] Jorge L. Lopez and Dimitri V. Nanopoulos. Flipped SU(5): Origins and re-
2922 cent developments. In *15th Johns Hopkins Workshop on Current Problems*
2923 *in Particle Theory: Particle Physics from Underground to Heaven Baltimore,*
2924 *Maryland, August 26-28, 1991*, pages 277–297, 1991.
- 2925 [89] Vincent Lucas and Stuart Raby. Nucleon decay in a realistic so(10) susy gut.
2926 *Phys. Rev. D*, 55:6986–7009, Jun 1997.
- 2927 [90] Ettore Majorana. Teoria simmetrica dell'elettrone e del positrone. *Il Nuovo*
2928 *Cimento*, 14(4):171–184, apr 1937.
- 2929 [91] Hisakazu Minakata and Alexei Yu. Smirnov. Neutrino mixing and quark-lepton
2930 complementarity. *Phys. Rev. D*, 70:073009, Oct 2004.
- 2931 [92] M. Mooney. The microboone experiment and the impact of space charge effects.
2932 2015.
- 2933 [93] E. Morikawa, R. Reininger, P. Gürtler, V. Saile, and P. Laporte. Argon, kryp-
2934 ton, and xenon excimer luminescence: From the dilute gas to the condensed
2935 phase. *The Journal of Chemical Physics*, 91(3):1469–1477, aug 1989.
- 2936 [94] FM Newcomer, S Tedja, R Van Berg, J Van der Spiegel, and HH Williams.
2937 A fast, low power, amplifier-shaper-discriminator for high rate straw tracking
2938 systems. *IEEE Transactions on Nuclear Science*, 40(4):630–636, 1993.
- 2939 [95] Emmy Noether. Invariant variation problems. *Transport Theory and Statistical*
2940 *Physics*, 1(3):186–207, jan 1971.

- 2941 [96] I. Nutini. Study of charged particles interaction processes on ar in the 0.2 - 2.0
2942 GeV energy range through combined information from ionization free charge
2943 and scintillation light. Technical report, jan 2015.
- 2944 [97] D. R. Nygren. The time projection chamber: A new 4π detector for charged
2945 particles. Technical report, 1974.
- 2946 [98] L. Onsager. Initial recombination of ions. *Phys. Rev.*, 54:554–557, Oct 1938.
- 2947 [99] S. Pascoli, S.T. Petcov, and A. Riotto. Leptogenesis and low energy cp-violation
2948 in neutrino physics. *Nuclear Physics B*, 774(1):1 – 52, 2007.
- 2949 [100] C. Patrignani et al. Review of Particle Physics. *Chin. Phys.*, C40(10):100001,
2950 2016.
- 2951 [101] B. Pontecorvo. Neutrino Experiments and the Problem of Conservation of
2952 Leptonic Charge. *Sov. Phys. JETP*, 26:984–988, 1968. [Zh. Eksp. Teor.
2953 Fiz.53,1717(1967)].
- 2954 [102] T. Yang R. Acciarri. Investigation of the non-uniformity observed in the wire
2955 response to charge in lariat run 1. Technical report, February 2017.
- 2956 [103] T. Yang R. Acciarri, M. Stancari. Determination of the electron lifetime in
2957 lariat. Technical report, March 2016.
- 2958 [104] Martti Raidal. Relation between the neutrino and quark mixing angles and
2959 grand unification. *Phys. Rev. Lett.*, 93:161801, Oct 2004.
- 2960 [105] Steve Ritz et al. Building for Discovery: Strategic Plan for U.S. Particle Physics
2961 in the Global Context. 2014.
- 2962 [106] C. Rubbia. The Liquid Argon Time Projection Chamber: A New Concept for
2963 Neutrino Detectors. 1977.

- 2964 [107] L.M. Saunders. Electromagnetic production of pions from nuclei. *Nucl. Phys.*,
2965 *B7*: 293-310(1968).
- 2966 [108] Qaisar Shafi and Zurab Tavartkiladze. Neutrino democracy, fermion mass hier-
2967 archies, and proton decay from 5d su(5). *Phys. Rev. D*, 67:075007, Apr 2003.
- 2968 [109] Sigma-Aldrich, P.O. Box 14508, St. Louis, MO 63178 USA.
- 2969 [110] R. K. Teague and C. J. Pings. Refractive index and the lorentz–lorenz function
2970 for gaseous and liquid argon, including a study of the coexistence curve near the
2971 critical state. *The Journal of Chemical Physics*, 48(11):4973–4984, jun 1968.
- 2972 [111] J. Thomas and D. A. Imel. Recombination of electron-ion pairs in liquid argon
2973 and liquid xenon. *Phys. Rev. A*, 36:614–616, Jul 1987.
- 2974 [112] D.R.O. Morrison N. Rivoire V. Flaminio, W.G. Moorhead. Compilation of
2975 Cross Sections I: π^+ and π^- Induced Reactions. *CERN-HERA*, pages 83–01,
2976 1983.
- 2977 [113] D.R.O. Morrison N. Rivoire V. Flaminio, W.G. Moorhead. Compilation of
2978 Cross Sections II: K^+ and K^- Induced Reactions. *CERN-HERA*, pages 83–02,
2979 1983.
- 2980 [114] Hermann Weyl. Gravitation and the electron. *Proceedings of the National
2981 Academy of Sciences of the United States of America*, 15(4):323–334, 1929.
- 2982 [115] Colin et al Wilkin. A comparison of pi+ and pi- total cross-sections of light
2983 nuclei near the 3-3 resonance. *Nucl. Phys.*, B62:61–85, 1973.
- 2984 [116] D. H. Wright and M. H. Kelsey. The Geant4 Bertini Cascade. *Nucl. Instrum.
2985 Meth.*, A804:175–188, 2015.

- 2986 [117] C. S. Wu, E. Ambler, R. W. Hayward, D. D. Hoppes, and R. P. Hudson.
- 2987 Experimental test of parity conservation in beta decay. *Phys. Rev.*, 105:1413–
- 2988 1415, Feb 1957.
- 2989 [118] N Yahlali, L M P Fernandes, K Gonzlez, A N C Garcia, and A Soriano. Imaging
- 2990 with sipms in noble-gas detectors. *Journal of Instrumentation*, 8(01):C01003,
- 2991 2013.
- 2992 [119] T. Yanagida. Horizontal symmetry and masses of neutrinos. *Progress of Theo-*
- 2993 *retical Physics*, 64(3):1103–1105, sep 1980.